EXPERIMENTAL INVESTIGATION OF THE REAR-BODY AERODYNAMICS OF A HELICOPTER FUSELAGE

by

Drew Gingras

A thesis submitted to the Faculty of Graduate Studies and Research in partial fulfillment
of the requirements for the degree of

Master of Science

Department of Mechanical Engineering
University of Alberta

Abstract

Helicopters have proven to be a versatile air vehicle in today's society and are used in a variety of applications. Many complexities arise in the aerodynamics of helicopters due to the presence of the main rotor downwash and the diverse range of flight conditions. The various uses of helicopters result in large variations in the aerodynamic loading, which can be problematic to safe flight operation.

An experimental setup was developed in the University of Alberta wind tunnel to analyze and improve the aerodynamic performance of a helicopter fuselage under a wide array of flight conditions. The experimental model was comprised of a 3D printed fuselage equipped with a motorized main rotor used to emulate the downwash. A six-axis load cell was used to measure the aerodynamic forces and moments acting on the fuselage. Stereoscopic and multiple-camera planar particle image velocimetry (PIV) techniques were used to analyze the development of the separation bubble in the rear-fuselage wake.

The forward flight condition was analyzed over an angle-of-attack range of $-15° \leq \alpha \leq 15°$ at zero side-slip. The drag force coefficients had the largest magnitude and decreased as the angle-of-attack was swept from positive to negative, while the lift force coefficients showed a linear increase over the same range. A down-force was present over for $-15° \leq \alpha \leq 5°$ while positive lift was noticed for $5° \leq \alpha \leq 15°$. The pitch moment was the only moment that showed any dependency on angle-of-attack for the forward flight condition. Nose-down moments were present for $-15° \leq \alpha \leq 7°$ while nose up moments existed for $7° \leq \alpha \leq 15°$.

The level flight condition was analyzed over the side-slip angles of $0° \leq \beta \leq 180°$ at zero angle-of-attack. The aerodynamic forces were found to have much larger magnitudes at high side-slip relative to the forces measured in the forward flight condition. Drag and side force coefficients were shown to have significant variation with changing side-slip. The drag increased to a maximum value occurring at $\beta = 80°$. The side force coefficients were positive for $0° \leq \beta \leq 100°$ and before transitioning to negative magnitudes for $100° \leq \beta \leq 180°$. The lift force coefficients showed small fluctuations around a magnitude of zero. The dominant moment acting on the fuselage was in the yawing direction, which is countered by the tail rotor. The roll moments showed a near linear increase for $0° \leq \beta \leq 90°$ before decreasing back to zero over $90° \leq \beta \leq 180°$. The pitch moment coefficients showed large changes in magnitude, particularly from $\beta = 20°$ to $30°$ and from $\beta = 60°$ to $70°$. These large magnitude variations draw concern for safe flight operation.

Stereo and multiple-camera planar PIV was used to analyze the effect of the main rotor downwash in the rear-fuselage wake. The presence of the downwash consistently resulted in a more rapid expansion of the wake, resulting in a larger separation region. The larger separation region would add to the pressure drag of the fuselage. The downwash also introduced an additional downwards component of velocity across the measurement region that resulted in a 10% increase of the mean velocity magnitude in the vertical plane of the wake.

Four rear-fuselage designs including a removable motor geometry, streamlined casing, and round casing were developed and analyzed at side-slip angles between $\beta = 0°$ and $40°$. The load measurements revealed that the streamlined case achieved up to 20% drag reduction over $0° \leq \beta \leq 30°$, while the round case increased the drag by up to 18% for $0° \leq \beta \leq 40°$. The magnitude of the pitch moment variation between $\beta = 20°$ and $30°$ was reduced by 36% and 67% using the streamlined and round cases respectively.

A four-camera planar PIV campaign was performed to investigate the effect of the four rear-fuselage geometries on the wake for side-slip angles of $0° \leq \beta \leq 40°$. The streamlined case was found to consistently reduce the size of the separation bubble, thus explaining the reduced drag. Sharp flow separation points were noticed to cause large regions of high velocity fluctuations. The constant aft-body curvature of the rounded case reduced the effects of the sharp separation point, resulting in less abrupt changes in the aerodynamic forces and moments for changing side-slip angle.

Preface

Some of this research was conducted in collaboration with an undisclosed company. The experimental setup was developed at the University of Alberta in collaboration with the company. Values of the aerodynamic load measurements have been removed and images of the helicopter model have been cropped to protect proprietary information, as requested by the company.

The experimental measurements and analysis were preformed by Drew Gingras under the supervision of Professor Sina Ghaemi from the Department of Mechanical Engineering at the University of Alberta.

Acknowledgements

I would like to thank my supervisor Dr. Sina Ghaemi for the continuous guidance and support that he provided throughout my studies. I would also like to thank Bryan Godbolt for the assistance and knowledge provided in the early stages of my work. Thanks to all the machine shop personal for playing a critical role in the design and fabrication of the experimental setup, and to the research group of Dr. Nobes for the access to the 3D printers and PIV equipment. Finally, thanks to all my friends and family for making my time here an enjoyable experience.

Contents

1 Introduction **1**

1.1 Motivation 1

1.2 Thesis Outline 2

2 Literature Review **4**

2.1 Helicopter Aerodynamics 4

2.1.1 Rotor Aerodynamics 4

2.1.2 Fuselage Aerodynamics 6

2.1.3 Experimental Investigations 7

2.1.4 Numerical Investigations 9

2.2 Flow Separation 10

2.2.1 Fundamentals 10

2.2.2 Suppression Techniques 12

2.2.3 Effect of Curvature 12

2.3 Particle Image Velocimetry 13

2.3.1 Main Principles 13

2.3.2 Particles 14

2.3.3 Imaging 15

2.3.4 Image Evaluation 16

2.3.5 Stereoscopic PIV 16

3 Experimental Setup **18**

3.1 Wind Tunnel Testing Facility 18

3.2 Helicopter Model 19

3.2.1 Fuselage 19

3.2.2 Rotor System 21

3.2.3 Mounting System 22

3.3 Instrumentation 23

3.3.1 Load Cell 23

3.3.2 Main Rotor and Cooling System Control 24

3.4 Particle Image Velocimetry 26

3.4.1 Stereo-PIV 26
3.4.2 Four-Camera Planar PIV 28

4 Characterization of Fuselage Aerodynamics 30
4.1 Load Measurements 30
4.1.1 Forward Flight Condition at Zero Side-Slip 30
4.1.2 Level Flight Condition at Zero Angle-of-Attack 33
4.2 Wake Analysis for Varying Angle-of-attack 39
4.3 Conclusions 42

5 Analysis of Side-Slip Angle and Rear-Fuselage Geometry on Wake Flow 46
5.1 Load Measurements 46
5.2 Four-Camera Planar PIV Investigation 49
5.2.1 Forward Flight Condition 49
5.2.2 Effect of Main Rotor Downwash 51
5.2.3 Effect of Side-Slip Angle 52
5.3 Conclusions 55

6 Conclusions 62
6.1 Summary of Results 62
6.2 Future Considerations 64

Bibliography 65

A Load Measurement Uncertainty 69

B Time Stability of Load Cell Data 71

List of Figures

2.1 Velocity distribution over rotor blade at various azimuth angles during (a) hovering flight, and (b) forward flight (Leishman, 2006). 5

2.2 Change in rear fuselage flow topology for (a) pitch-down and (b) pitch-up orientations. 7

2.3 The Ahmed body showing the rounded leading edge and the angled back ramp. 12

2.4 Generic experimental setup for PIV in a wind tunnel showing illuminated particles captured at two instances (Raffel *et al.*, 2007). 13

2.5 Polar spectrum of light scattering from a 532 nm incoming light by a 1 μm oil particle in air using Mie scattering theory (Raffel *et al.*, 2007). 15

2.6 Cross-correlation analysis flow chart for double frame, single exposure PIV measurement (Raffel *et al.*, 2007). 16

2.7 Stereo PIV imaging configuration showing the breakdown of the velocity components detected by each camera. 17

2.8 Common camera configuration used in stereo PIV measurements. 17

3.1 Helicopter model mounted in the University of Alberta Wind Tunnel showing the rotating rotor and a laser sheet used for PIV measurements. 19

3.2 Sectioned view of the helicopter model showing the internal components. . . 20

3.3 Rear fuselage appendages studied in the investigation. 21

3.4 Comparison of the rotor equipped model to the isolated fuselage configuration showing the load cell decoupling mount system. 23

3.5 Location of the load cell (LC) axes relative to the body fixed axes with origin at the center-of-mass (COM). Components p_1 and p_2 of the position vector ($\boldsymbol{p}$) are shown to relate the two coordinate systems. 24

3.6 Body fixed axes showing definition of the roll, pitch, and yaw moments with respect to the approximate location of the center-of-mass. 25

3.7 Wind axis definition showing the the angle-of-attack and side-slip angle with respect to the body fixed axis. Drag, side, and lift forces are defined with respect to wind axis. 26

3.8 Combined stereo- and planar-PIV setups showing approximate camera positions and field of view locations with respect to the helicopter fuselage. . . . 27

3.9 (a) Four camera planar PIV setup showing horizontally mounted cameras, (b) field of view size and location with respect to the helicopter fuselage. . . 28

4.1 (a) Force coefficients and (b) moment coefficients for the baseline configuration with varying angle-of-attack at zero side-slip. 31
4.2 Slope of the pitch moment with respect to angle-of-attack (dC_m/dα). . . . 32
4.3 Resultant vector of the pitch and roll moment coefficients showing the changes in magnitude and direction of the moment acting in the $x'y'$ plane. The forward flight conditions are shown for -15° $\leq \alpha \leq$ 15° in 2.5° increments at zero side-slip. 34
4.4 (a) Force coefficients and (b) moment coefficients for the baseline configuration with varying side-slip angle at zero angle-of-attack. 35
4.5 Slope of the roll moment coefficients with respect to side-slip angle (dC_l/dβ). 36
4.6 Slope of the pitch moment coefficients with respect to side-slip angle (dC_m/dβ). 37
4.7 Combined pitch and roll moment coefficients showing the changes in magnitude and angle of the moments acting in the $x'y'$ plane. The level flight conditions are shown for (a) 0° $\leq \beta \leq$ 90° and (b) 90° $\leq \beta \leq$ 180° with 10° increments at zero angle-of-attack. 38
4.8 Flight envelope for the level flight condition showing the magnitude of the resultant roll and pitch moment vector ($|C_{lm}|$) for side-slip angles varying between $\beta = 0°$ and 180° in 100° increments. 39
4.9 Normalized velocity magnitudes in the intersecting xy and xz planes comparing (a) the isolated fuselage and (b) the rotor equipped model at α = -5°. 40
4.10 Normalized velocity magnitudes in the intersecting xy and xz planes comparing (a) the isolated fuselage and (b) the rotor equipped model at $\alpha = 0°$. 44
4.11 Normalized velocity magnitudes in the intersecting xy and xz planes comparing (a) the isolated fuselage and (b) the rotor equipped model at $\alpha = 5°$. 45

5.1 (a)Drag and (b) lift coefficients with varying side-slip angle for the four tested configurations at zero angle-of-attack compared to data presented in Stepanov *et al.* (2016). 47
5.2 Dimensionless (a) roll and (b) pitch moment coefficients for varying side-slip angle comparing the four fuselage configurations at zero angle-of-attack. . . 49
5.3 Instantaneous vorticity field at zero angle of incidence comparing the (a) baseline, (b) empty, (c) cusped, and (d) round case configurations. 50
5.4 Normalized velocity magnitudes comparing the (a-d) isolated fuselage and (e-h) the rotor equipped model for the four rear-fuselage configurations at zero angle of incidence. 56

5.5 Normalized RMS velocity fields comparing the (a-d) isolated fuselage and (e-h) the rotor equipped model for the four rear-fuselage configurations at zero angle of incidence. 57
5.6 (a-d) Normalized velocity magnitudes and (e-h) RMS fluctuation fields comparing the four fuselage geometries at a side-slip angle of $\beta = 10°$. 58
5.7 (a-d) Normalized velocity magnitudes and (e-h) RMS fluctuation fields comparing the four fuselage geometries at a side-slip angle of $\beta = 20°$. 59
5.8 (a-d) Normalized velocity magnitudes and (e-h) RMS fluctuation fields comparing the four fuselage geometries at a side-slip angle of $\beta = 30°$. 60
5.9 (a-d) Normalized velocity magnitudes and (e-h) RMS fluctuation fields comparing the four fuselage geometries at a side-slip angle of $\beta = 40°$. 61

A.1 (a) Force coefficients and (b) moment coefficients for the baseline configuration with varying angle-of-attack at zero side-slip using black and red markers to distinguish the repeated measurements. 69
A.2 (a) Force coefficients and (b) moment coefficients for the baseline configuration with varying angle-of-attack at zero side-slip with error bars. 70

B.1 Variation of the drag force coefficients with time at $\alpha = 15°$ and zero side-slip. 71
B.2 Variation of the side force coefficients with time at $\alpha = 15°$ and zero side-slip. 72
B.3 Variation of the lift force coefficients with time at $\alpha = 15°$ and zero side-slip. 72
B.4 Variation of the roll moment coefficients with time at $\alpha = 15°$ and zero side-slip. 72
B.5 Variation of the pitch moment coefficients with time at $\alpha = 15°$ and zero side-slip. 73
B.6 Variation of the yaw moment coefficients with time at $\alpha = 15°$ and zero side-slip. 73

List of Tables

3.1 Measurable range, resolution, and uncertainty for the Mini45 six-axis load cell. 23

Chapter 1

Introduction

1.1 Motivation

Helicopters play an integral role in today's society. Helicopters are designed to perform vertical takeoff and landing (VTOL), sustained hover, as well as forward, reverse, and lateral flight maneuvers, providing a versatile method of transportation. The ability to precisely maneuver within both rural and urban environments makes helicopters a desirable vehicle for many applications. Some of the current uses of helicopters include military combat and transport, emergency response, fire fighting, law enforcement, new reporting, aerial tours, and many others. Helicopters also have the ability to support sling loads to provide aerial transport of oversized structures that may not be transportable by land.

The design of a helicopter proves to be a technical challenge due to the many complexities involved with the aerodynamics of bluff bodies. Thrust is produced by the lift force acting on the main rotor blades which pass air downwards through the rotor plane, known as the main rotor downwash. The downwash produced by the main rotor consists of highly turbulent and swirling flow that acts over the helicopter fuselage (Seddon and Newman, 2011). Tip vortices that shed from the main rotor can interact with the trailing blades, known as blade-vortex interaction (Poling *et al.*, 1989), or with downstream sections of the fuselage causing an oscillating vortex-structure interaction, as studied by De Gregorio *et al.* (2012). The versatility of helicopters inherently results in a large amount of flight conditions that can be experienced. The changing wind directions can result in high positive and negative angles-of-attack and side-slip angles. Light-weight helicopters are particularly vulnerable to variations from strong wind gusts since they incorporate lighter and weaker engines.

As climate change has seen increasing awareness in the past few decades, the emphasis on reducing emissions and improving fuel economy has also become more present in research. The aerodynamic drag of a helicopter plays an important role in the fuel consumption and emissions that are produced as drag works against the forward flight motion. The drag associated with a helicopter primarily derives from the main rotor components and the fuselage (Prouty, 1986). As the largest component of typical helicopters, the fuselage typically accounts for 20-40% of the parasitic drag (Wagner, 1973; Grawunder *et al.*, 2012; Leishman, 2006). A helicopter fuselage is considered a bluff body which is associated with a low velocity separation bubble that develops in its wake (Anderson, 2016). Reducing the size of the separation bubble can reduce the pressure drag, and thus improve the fuel efficiency of the helicopter.

Another critical component of helicopter performance is the ride safety and stability. The complex aerodynamics and the wide array of flight conditions experienced by helicopters can cause large changes in the aerodynamic loading. Helicopters are susceptible to pilot or control induced oscillations (McRuer, 1995) that can be caused by applying a higher control input than required to correct a disturbance. Rotor-driven aircraft experience a delay between the control input and the reaction of the aircraft that can cause the pilot to provide an over-correcting response. A mean of mitigating such scenarios is to minimize the frequency and magnitudes of the disturbances from wind gusts or large changes in flight attitude that require large corrections of the rotor trim. The magnitude of the disturbances can be related to the changes in aerodynamic loading of the helicopter. Therefore, ensuring that the helicopter fuselage has smooth transitions in the loading is essential.

The objective of this investigation was to characterize the aerodynamics of a helicopter fuselage by performing wind tunnel test over various flight conditions. Problems involving the critical parameters, including the drag and stability of the fuselage, were addressed by developing new geometries to improve the aerodynamic performance. Stereo and multiple camera planar PIV techniques were used to analyze the development of the rear-fuselage wake, and to determine the effect of the main rotor downwash.

1.2 Thesis Outline

The contents of this thesis are organized as follows:

- Chapter 2: An overview of the background material relevant to the investigation is provided. Various complexities involved with helicopter aerodynamics are described. A review of relevant investigations on helicopter fuselage aerodynamics is given. Separation of flow behind a bluff body is explained. An introduction to PIV measurement techniques is also provided.

- Chapter 3: A description of the experimental setup is given. Details of the the wind tunnel facility, and specifications of the helicopter model, mechanical supports, sensors, and PIV measurement equipment are described.

- Chapter 4: Results of the experimental investigation performed to characterize the fuselage aerodynamics are presented. Aerodynamic force and moment measurements are provided for various angle-of-attack and side-slip conditions. Results of four-camera planar and stereo-PIV investigation focused on the fuselage wake are analyzed.

- Chapter 5: The effect of side-slip angle is investigated further, and various rear-fuselage geometries are implemented with intent to improve the aerodynamic performance. Results from load measurements and a four-camera planar PIV campaign are analyzed.
- Chapter 6: A summary of the results from this investigation is given. Suggestions for future work in the field of helicopter aerodynamics are outlined.

Chapter 2

Literature Review

This chapter provides an overview of the complex flow field related to helicopter aerodynamics and flow separation. A review of relevant experimental and numerical studies is presented to provide reference for the results discussed in later chapters. An overview of the working principle of planar PIV is also provided. In this thesis, planar PIV measurement techniques are utilized to analyze the flow separation region in the wake of the helicopter fuselage.

2.1 Helicopter Aerodynamics

2.1.1 Rotor Aerodynamics

Helicopters experience various technical challenges for aerodynamic design. The complications that arise from the presence of the main and tail rotors have large effects on the stability and control of a helicopter. The velocity distribution over the main rotor is more complex compared to the distribution over fixed-wing aircraft, as shown in Figure 2.1. The rotation of the main rotor causes a linear velocity distribution with the highest acting flow speed over the tip of the of the blades. In hover or vertical flight the velocity distribution over the blades remains constant as a function of the azimuth angle ψ. In forward flight however, the flight speed adds a component to the velocity acting over the blade in a single direction. The additional component of velocity results in stronger flow acting over the advancing blades and a weaker flow acting over the retreating blades. At a large enough flight speed the advancing blades can experience transonic flow and may even develop shock waves. The compressible flow features not only add to the power requirements of the motor, but also increase the noise that can be disruptive in an urban setting. The retreating blades experience a net negative flow direction acting over the blades as a result of the freestream velocity. This results in a reversed flow region that will cause a reduction in lift on the retreating side of the rotor disk shown Figure 2.1b. The reduced lift on the retreating blades forces the operator to increase the angle-of-attack of the retreating blades via cyclic pitch controls to compensate for the loss of lift in the reversed flow region. If the blade angle-of-attack becomes too large, the blades can stall, causing a sudden loss in lift and a separated flow region in the rotor wake. The combination of the higher velocity on the advancing side and the lower velocities on the retreating side produces a nonuniform distribution of lift across the rotor disk. The rotor limitations at high advanced ratios (ratio of the freestream to the rotor tip velocity) restrict the rotor performance which can lead to unstable flight conditions, as discussed in Drees and Harvey (1970); Wang *et al.* (2017).

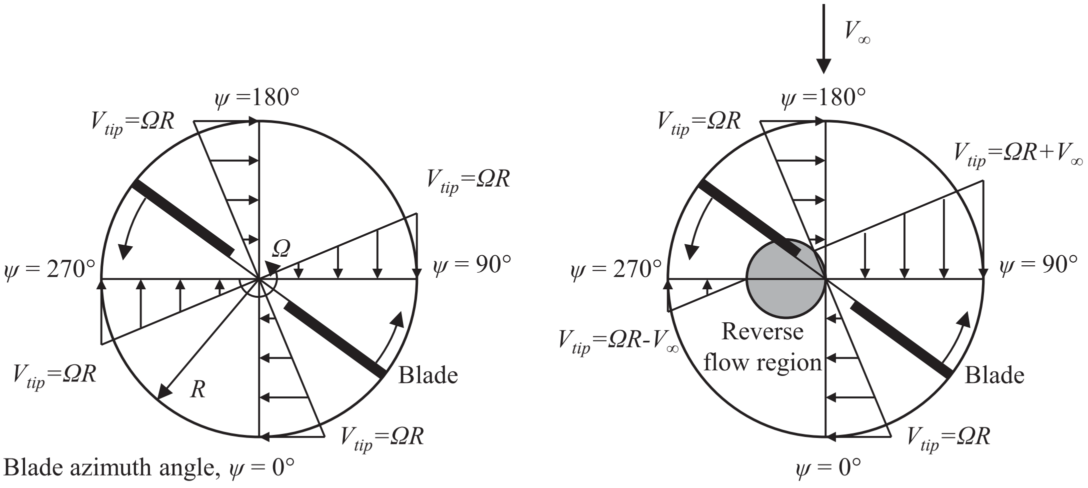

(a) Hover flight

(b) Forward flight

Figure 2.1: Velocity distribution over rotor blade at various azimuth angles during (a) hovering flight, and (b) forward flight (Leishman, 2006).

Another issue that derives from the rotor is the interactions involving the blade tip vortices. Fixed-wing aircraft have tip vortices follow downstream of the wing and typically do not interact with the aircraft. The blades of the helicopter rotor however, rotates around in a circular path causing the following blades to interact with the tip vortices of the leading blades. The interaction of the blades with the tip vortices causes fluctuating airloads on the blades and is known as blade-vortex interaction (Poling *et al.*, 1989). The path of the tip vortices also varies dependant on the flight speed. As the flight speed is increased, the trajectory of the tip vortices begins to travel downstream towards the fuselage and tail boom of the helicopter. At higher flight speeds the tip vortices travel farther downstream and interact with the tail rotor or tail empennages. The interaction of the low pressure cores from the tip vortices with the tail boom and empennages have been known to cause vibrations and is often referred to as a tail shake condition, which was investigated in De Gregorio *et al.* (2012). The tail shake condition can result in undesired loading on the tail boom and it's connection to the fuselage, while also causing vibrations in the cabin that can disturb the passengers or sensitive instruments in the payload. The vibrations can also effect the flow separation in the rear fuselage area which could implement drag penalties.

2.1.2 Fuselage Aerodynamics

The parasitic drag of a helicopter serves an important role in evaluating the aerodynamic performance. The parasitic drag is the combined drag from the components of the helicopter that do not provide any direct contribution to the lift produced by the main rotor (Seddon and Newman, 2011). As in ground vehicles, the fuel efficiency depends greatly on parasitic drag, especially at high flight speeds since drag is proportional to the square of velocity (Anderson, 2016). The largest contributors to parasitic drag for a helicopter are the fuselage and the rotor system including the hub, shaft, and blades. A typical drag breakdown by Prouty (1986) estimated that the fuselage contributes to approximately 30% of the parasitic drag while the rotor head contributes to 35%. These values provide only an estimation and depend on the individual helicopter. Other studies have shown fuselage drag accounting for 25-40% of the parasitic drag with rotor system contributions of 20-50% (Wagner, 1973; Grawunder *et al.*, 2012; Leishman, 2006). High amounts of turbulence is generated behind the rotor system due to the sharp edges and rotating components. The fuselage is the largest component of the helicopter and its size is typically governed by passenger and cargo requirements. Most helicopter fuselages are considered to be bluff bodies in aerodynamic investigations as the drag is dominated by pressure rather than viscous forces. Many fuselage designs promote large areas of flow separation that have considerable drag consequences. The aft-body design is critical to bluff bodies because the aft-body governs the properties of the wake region that contributes to the pressure drag. Each fuselage model has a different rear design to accommodate the uses of the helicopter. The various designs will exhibit different flow separation regions that will play a role in the aerodynamic performance of the helicopter.

Helicopters often encounter flight conditions that result in large angle-of-attack and side-slip angles due to their lower flight speeds. Helicopters are also capable of vertical and lateral maneuvers that can complicate the flow fields (Leishman, 2006). The vertical ascent of a helicopter involves an influx of air through the rotor disk. An additional component of velocity from the ascent rate is added to the flow traveling through the rotor disk. The fuselage lies within the downwash and contributes to a vertical drag that opposes the thrust produced by the main rotor. The descent of a helicopter is particularly a difficult feat from an aerodynamic perspective. Descent involves the helicopter passing through the vortices, turbulence, and separated flow produced by the rotor downwash (Seddon and Newman, 2011). The high turbulence makes the descent of a helicopter a complex maneuver.

Forward flight typically consists of a nose down configuration which maintains the influx of air through the rotor plane. The flight speed also contributes to an additional velocity that acts over the body. The combination of these flow patterns introduces a complex interaction of the high-swirl flow of the downwash with the boundary layer and the fuselage wake. The pitch-up configuration is known to form an eddy flow with span-wise vortex rolls (classical bluff body) while the pitch-down configuration forms stream-wise vortices (Seddon and Newman, 2011), as shown in Figure 2.2. While in hover and at low flight speeds, a helicopter can be subjected to winds gusts from all directions. The sporadic nature of wind gusts cause rapid variations of relative wind direction which results in large shifts in the aerodynamic loading.

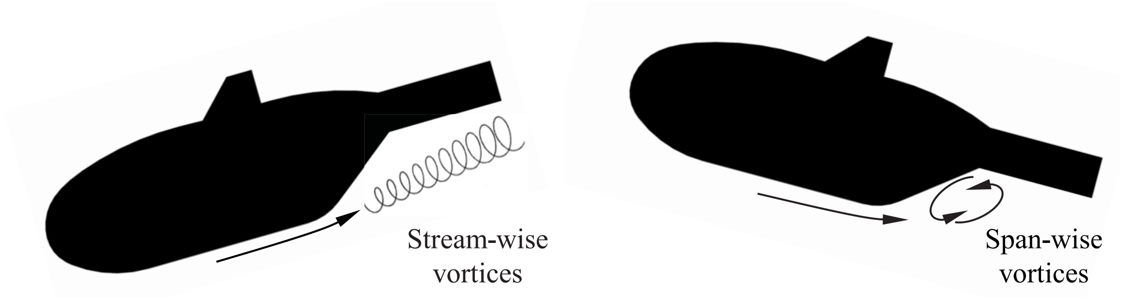

(a) Vortex flow (b) Eddy flow

Figure 2.2: Change in rear fuselage flow topology for (a) pitch-down and (b) pitch-up orientations.

When at close proximity to the ground a helicopter experiences a flight condition referred to as ground effect. The presence of the ground alters the wake and can effect the performance of the main rotor. The ground causes an expansion of the wake near the surface which alters the velocity travelling through the rotor disk, and in turn affects the thrust. The effect is more pronounced in hovering flight than in forward flight (Leishman, 2006). The effects of the ground provide an increase in thrust at a given motor power (Knight and Hefner, 1941). To be free from ground effects, it has been found that a minimum distance from the ground of two times the rotor radius must be present (Fradenburgh, 1972; Hayden, 1976). The wide array of flight conditions makes the aft-body design critical and characterization of the aerodynamic loads an important tool for optimizing the aerodynamic performance.

2.1.3 Experimental Investigations

Wind tunnels enable partial-scale models to be used to measure the forces acing on the body in similar conditions as a full scale model. Wind tunnels can be used to investigate the aerodynamic response of helicopters under various flight conditions. The majority of wind tunnel investigations are focused on drag reduction techniques in forward flight on scaled fuselage models.

Breitsamter *et al.* (2014) investigated passive techniques for parasitic drag reduction on a 1:5 scale model of a light class utility helicopter including a rotating rotor. Measurements were performed in a 2.4×4.8 m^2 wind tunnel test section to supplement CFD simulations. Load measurements evaluated drag reduction due to the implementation of the VGs, rotor hub and landing gear geometries. PIV was used to determine the mean axial velocity and RMS velocity distributions in the aft-body region and was used to visualize the effect of the

VGs. CFD was performed to visualize surface streamlines and pressure distribution on the body of the fuselage with particular interest in the aft-body region. A reduction in the size of the wake and drag was noted for the faired skid landing gear configurations. An overall drag reduction of 2.3% was noted relative to the original model. The VGs and strakes on the up-swept portion of the fuselage provided a 1.4% drag reduction for over the tested angles-of-attack.

Zanotti *et al.* (2016) experimentally evaluated the effectiveness of CFD design components that were optimized for drag reduction. Tests were performed on a 1:4 scale model of a NH90 medium sized military helicopter with a rotating rotor in a 4.00×3.84 m^2 wind tunnel test section. Load measurements were used to compare different VG configurations, fairing sponsors, and rotor hub caps while the stereo-PIV was used to analyze the velocity in the aft-body region. Pressure taps were used to determine pressure fluctuations in the aft-body region. The load measurements confirmed drag reduction of up to 6% for the configuration containing counter-rotating VGs and . The PIV results showed a reduction in the size of the wake region, similar to Breitsamter *et al.* (2014). The implementation of the VGs showed a drop in the root mean square (RMS) pressure fluctuations in the up-swept section of the aft-body.

Le Pape *et al.* (2015) reported the effectiveness of active flow control on an isolated and simplified blunt fuselage model. A 2.4 m diameter circular test section wind tunnel and a fuselage model corresponding to a blockage ratio of 1.5% were used to carry out the measurements. Pressure tap and load measurements were used to evaluate the effectiveness of actively controlled synthetic jets on the drag reduction of the fuselage. An overall drag reduction of 20% was achieved. The synthetic jets showed highest drag reductions for nose down angles-of-attack using slots on the side of the body. The nose up configurations experienced the highest drag reduction using slots on the bottom of the body. The flow topology for the pitch up and pitch down configurations agrees with those presented by Seddon and Newman (2011).

De Gregorio *et al.* (2012) investigated on a fully equipped scaled helicopter model with a motorized main and tail rotor to characterize the flow field and to analyze aerodynamic interactions of the main rotor and several components of the helicopter. A 1:3.88 scale of a NH90 medium sized transport helicopter was tested in an 8×6 m^2 wind tunnel test section to acquire data for the increasing demand of CFD validation. Multiple domains were analyzed using PIV including above and below the tail boom, as well as above the horizontal stabilizer near the tail rotor. Pressure tap measurements were also used to supplement the PIV data. The motorized model experienced increased cross flow and decreased vertical velocities when compared to the isolated fuselage. The vortices detached from the main rotor hub were reported to decrease in strength and have an altered path downstream of the hub. The motorized model was also reported to have a drag increase relative to the isolated fuselage associated with a loss of momentum in the region below the fuselage.

There are a limited number of experimental studies that consider side-slip angles that would be experienced in strong crosswinds and gusts. Reß *et al.* (2015) investigated the effect of side-slip angle on the drag, lift, and yawing moment coefficients for a range of side-slip angles between -10° to 10°. The same 1:5 scaled model equipped with a rotating rotor as Breitsamter *et al.* (2014) was used in the 2.4×4.8 m^2 wind tunnel test section. The model was tested with a number of landing gear configurations and also compared the effect of the rotor downwash. The study noted that the configurations including the rotating rotor resulted in a consistently increased drag at each angle-of-attack and side-slip angle. The lift for the rotor equipped model showed an increased slope with respect to angle-of-attack. The optimal landing gear achieved a drag reduction of 45% relative to the original landing gear.

Stepanov *et al.* (2016) investigated the drag on a 1:7 scaled model based on the fuselage of a twin engine light ANSAT helicopter. An open jet wind tunnel at the Kazan National Research Technical University was used to collect force and moment measurements to analyze drag of various configurations. Different fuselage designs, landing gear skids, and fuel tank geometries were tested at angles-of-attack between -10° and 10°, and side-slip angles between -18° and 18°. The investigation found that the addition of landing gear skids and fuel tanks added 80% and 48% to the base fuselage drag, respectively. Up to 16% drag reduction for the tested angles-of-attack was achieved by streamlining the rear fuselage design.

Hilbert (1984) developed revisions to a mathematical model used to describe the aerodynamics forces and moments acting on an UH-60A Black Hawk helicopter. Wind tunnel data from Howlett (1981) was used as a verification method for the force and moment coefficients presented for an angle-of-attack range of -90° to 90° and for a side-slip range of -90° to 90°.

The physical limits and complexity of some wind tunnel experiments can limit the regions of interest that may be necessary to provide a fundamental understanding of the problems that need to be addressed.

2.1.4 Numerical Investigations

The advancement in computational abilities has been valuable for aerodynamic design as it has enabled the use of Computational Fluid Dynamics (CFD). Numerical simulations are beneficial for aerodynamic optimization since modifications to the geometry in question can be easily made. Thus, several iterations may be performed while making minute changes to the body using 3D modelling software. The results that can be obtained from numerical simulations are quite desirable since 3D flow patterns and pressure distributions can be obtained. Several investigations on the aerodynamics of helicopters have used CFD.

Brunello *et al.* (2012) measured force and moment coefficients up to side-slip angles of ±180° to develop a database for flight dynamics modelling. A 1:10 scaled model of an

Australian Defense Force helicopter was tested in an octagonal wind tunnel section with 9×7 ft^2 dimensions. The purpose of the work was to develop a database for slung load modeling and to provide load measurements that can validate CFD simulations. Smoke streams were also used in the wind tunnel to visualize the flow at higher side-slip angles. A component of the CFD investigation was used to simulate the vortex structure that was found in the experimental flow visualization at a side-slip angle of -22.5°. Moment coefficients were computed for side-slip angles ranging between 45° to compare with wind tunnel measurements. Significant discrepancies were noted between the CFD and wind tunnel results at high side-slip angles.

Boniface (2016) utilized CFD to visualize and quantify the effectiveness of vortex generators on drag reduction in pitch-up and pitch-down configurations in forward flight. The drag reduction of vortex generators was also analyzed for a 5° side-slip angle. Though no experiments were performed in this investigation, validation of results was referenced to other investigations of the GOAHEAD project (Pahlke, 2007; Raffel *et al.*, 2011; Steijl and Barakos, 2009; Renaud *et al.*, 2012) since the fuselage model was geometrically similar with the exception of different sponsors.

The work by Filippone (2007) paired CFD and wind tunnel results to determine the drag and lift at small side-slip angles, and provided streamline traces of the flow acting at a side-slip angle of 30°. Deviation from the experimental measurements was noted as a result of the flow separation causing the solver to diverge. It was also noted that large amounts of computing power would be required to adequately resolve the large flow separation regions present in high yaw conditions.

Vogel *et al.* (2010) used numerical simulations for flow topology in the aft-body region of a helicopter fuselage for a single configuration and flight condition. The CFD data showed large discrepancies from the reference wind tunnel data. It was noted that a well resolved wake area and hybrid turbulence models are required for accurate simulations of separated wake flows.

A recurring issue with many of the CFD investigations is the divergence from the experimental data at high side-slip angles. Many of the studies have attributed the issue to the significant regions of separated flow that occur in these conditions. These large separation regions require a more refined grid to resolve the flow, thus requiring much higher computational requirements. CFD studies often limit the configurations that are investigated due to the mesh requirements at higher angles of incidence.

2.2 Flow Separation

2.2.1 Fundamentals

When a fluid passes over a solid surface, the viscous forces produce an imposing force on the body resulting in an adverse pressure gradient. An adverse pressure gradient is an increasing pressure distribution in the flow direction (Anderson, 2016). As the fluid travels downstream, it must work against an increasing pressure which causes a reduction in velocity. The local region of decreased flow speed causes the near wall velocity profile to have a gradient in the wall normal direction, known as the boundary layer (Prandtl, 1904). The velocity gradient eventually reaches point where it transitions from positive to negative, resulting in flow separation. For internal flows an adverse pressure gradient can be caused by an expansion of the cross sectional area, such as a diverging channel. For flow around a body an adverse pressure gradient can be caused by a reduction in the cross sectional area normal to the flow, such as the rear section of submersed cylinder or the rear section of an airfoil. The flow farther downstream may have a negative velocity gradient leading the streamlines to detach from the wall and for a recirculating region to develop.

Another mechanism that can cause flow separation is and abrupt change in geometry. Flow separation at a sharp edge occurs at a fixed point located at the geometric singularity, such as the classical example of a backwards facing step. As the fixed separation point implies that little can be done to delay the flow separation.

A consequence of separated flow is that the pressure distribution in the separated region is vastly altered. This change in the pressure distribution contributes primarily to a large increase in drag known as pressure drag (Anderson, 2016). The pressure in the separated region of the flow is lower than that of attached flow, causing a force on the rear section of the body opposing the flow direction to reduce. The reduction of this force opposing the flow direction results in an increase in the net drag force acting on the body. In the case of an airfoil at a high angle-of-attack, flow separation also results in a large reduction in lift.

Another consequence of flow separation, particularly behind bluff bodies, is the phenomenon of vortex shedding. Vortex shedding is an oscillating flow that occurs in the separated flow region behind bluff bodies. Vortex shedding causes alternating low pressure vortices that can cause the body to oscillate (Williamson and Govardhan, 2004). The oscillating pressures can also produce noise that is undesirable.

The Ahmed body (Ahmed *et al.*, 1984) is a bluff body geometry that has been used in generalized investigations of ground vehicles. The Ahmed body consists of a flat base with a rounded leading edge and an angled ramp on the upper back surface, as shown in Figure 2.3. Three main flow features were found in the wake of the Ahmed body. Firstly, a recirculating region is formed at the back ramp. Another recirculating region forms from the separation from the flat bottom surface. Stream-wise vortices that roll up from the side up to the top surface of the ramp also form and produce three-dimensional flow in the wake. The flow was found to have a great dependency on the slant angle of the back ramp. The flow remains relatively attached for slant angles up to 12°, while between 12° and 30°, the stream-wise vortices begin to form. At slant angles greater than 30° the flow fully separates from the back ramp resulting in a sudden drop in drag. Investigations have shown that the drag increases significantly with increasing side-slip angle (Bello-Millán *et al.*, 2016).

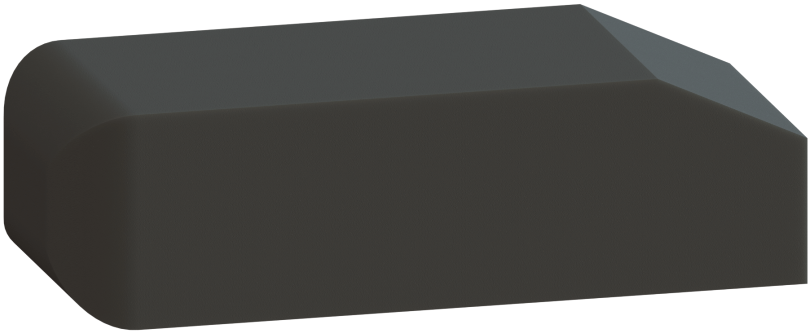

Figure 2.3: The Ahmed body showing the rounded leading edge and the angled back ramp.

2.2.2 Suppression Techniques

In general, laminar flow is more susceptible to separation than turbulent flow since the energy in the fluid elements near the wall is higher in turbulent flow (Anderson, 2016). Not only are turbulent flows less likely to separate, the recirculating regions that result are also smaller. This concept has been exploited in flow control investigations using vortex generators, synthetic jets, and actuators. Correct size and placement of vortex generators have shown that transporting low momentum fluid of the near wall region to outer regions of the boundary layer can effectively avoid or delay the separation for backwards facing ramps (Lin *et al.*, 1990, 1991; Lin, 1999). Synthetic jets have been shown to reduce drag of a submersed cylinder (Wang *et al.*, 2007), and to reduce the separation region on the top surface of an airfoil (Liu *et al.*, 2015). Plasma actuators have been shown to minimize the separated region of the flow in a backwards facing step (Gholamhosein Pouryoussefi *et al.* (2015)), to minimize the fluctuations in the wake of a blunt trailing edge (Nati *et al.*, 2013), and to control separation on high angle-of-attack airfoils (Post and Corke, 2004).

2.2.3 Effect of Curvature

The curvature of the wall has a significant effect on the flow separation. Stronger curvatures typically result in a higher adverse pressure gradient and will then induce separation sooner than gradual curvatures. Convex and concave curvatures have vastly different effects on the boundary layer (Muck *et al.*, 1985; Hoffmann *et al.*, 1985; Tulapurkara *et al.*, 2001). Convex curvatures tend to have a stabilizing effect on boundary layers by attenuating pre-existing turbulence (Muck *et al.*, 1985). Concave curvatures tend to have a destabilizing effect on boundary layers and notably changes the turbulence structures within (Hoffmann *et al.*, 1985). Convex curvatures are found to suppress turbulence intensities while concave curvatures increase boundary layer thickness (Tulapurkara *et al.*, 2001). Boundary layers show a faster response to convex curvature while the response is slow for concave curvatures (Tulapurkara *et al.*, 2001). A direct numerical simulation was performed by Lamballais *et* *al.* (2010) to investigate effect of the curvature of a leading edge on separation region on a half-flat plate showing the effect of the separations angle on the wake.

2.3 Particle Image Velocimetry

2.3.1 Main Principles

Particle image velocimetry is a non-intrusive flow measurement technique used to capture velocities of flow fields (Raffel *et al.*, 2007). The technique involves imaging local displacements of fluid elements over a known time interval. Small tracer particles are seeded into the flow to follow the fluid's motion. The particles must be sized small enough to ensure that the flow is not disrupted, and large enough to be captured by the imaging system. Two successive images of a measurement region illuminated by a thin light sheet are captured at a short time interval. The light sheet illuminates the particles for two short pulses to freeze the motion of the seeded particles. The time between the two pulses is determined by the mean flow velocity to ensure the local displacement is within the imaged region. The light scattered by the particles is recorded on separate frames and the results are then processed using an image cross correlation. The shift in location of local intensity peaks provides a reference displacement and, with the know time interval between the two images, can provide spatially resolved velocity fields. Figure 2.4 shows a generic schematic of a planar PIV setup in a wind tunnel.

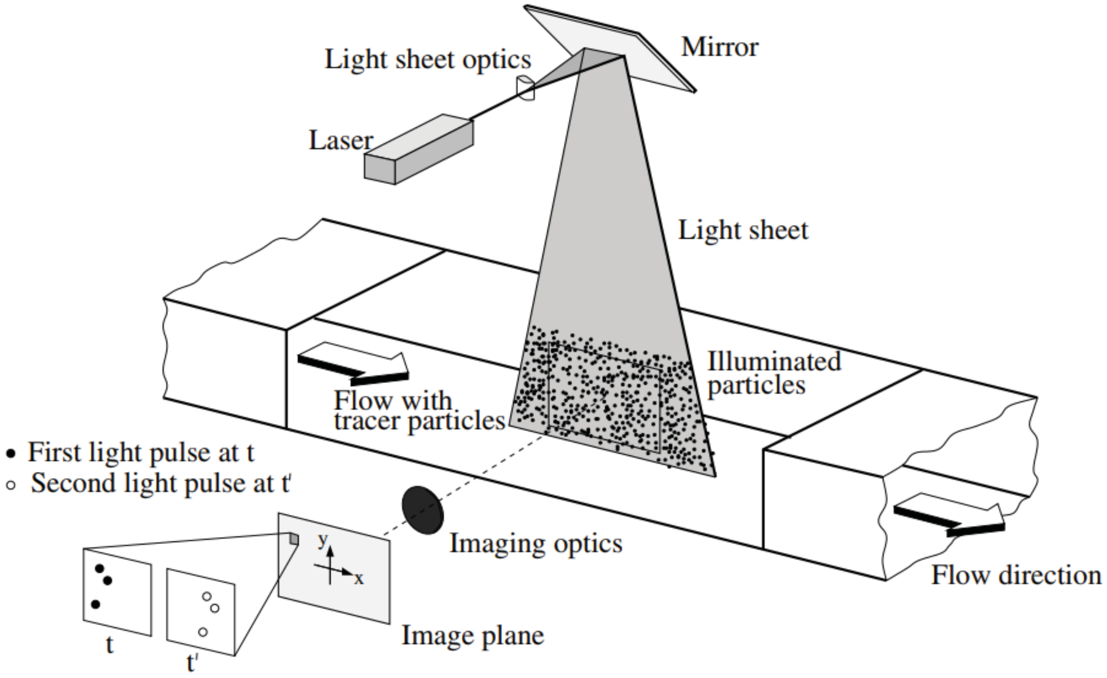

Figure 2.4: Generic experimental setup for PIV in a wind tunnel showing illuminated particles captured at two instances (Raffel *et al.*, 2007).

2.3.2 Particles

Particle selection is particularly important for ensuring accuracy of PIV measurements. The desired output of PIV campaigns is a velocity field of the fluid, thus an integral characteristic of the particle is that it must accurately represent the motion of the fluid. To achieve this, the particles must be small and have a similar density to the fluid. The Reynolds number used to describe the motion of the particles is defined as

$$Re = \frac{\rho \Delta U d_p}{\mu} \tag{2.1}$$

where ρ is the density of the fluid, ΔU is the difference in velocity between the particle and the fluid, d_p is the diameter of the particle, and μ is the dynamic viscosity of the fluid. Since the Reynolds number of the particles is typically small ($Re < 1$) the forces follow Stoke's law and are dominated by friction forces. The equation of motion of the particles can then be described as

$$\frac{\pi}{4} d_p(\rho_p - \rho)\frac{dU_p}{dt} = \text{-}3\pi\mu d_p \Delta U \tag{2.2}$$

where ρ_p is the density of the particle and ρ is the density of the fluid. Equation 2.2 shows that it is ideal to select particles with the same density as the fluid. For wind tunnel tests where the working fluid is air, finding a particle with a similar density is much more difficult. Gaseous flows require small particles to overcome the large difference in density and ensure that the flow is accurately traced.

Another important characteristic of the selected particle is the ability to scatter light efficiently. The correlation performed on the image requires a strong contrast between the captured intensities and the background of the image. The light scattered by the particle is proportionate to the captured intensity in the image. The Mie scattering theory states that the light scattered by the particle depends on the diameter of the particle, the wavelength of the particle illumination, and the ratio of refractive index of the particle relative to the surrounding fluid (Van der Hulst, 1981). A polar distribution of the Mie theory light scattering for a 1 μm oil particle in air is shown in Figure 2.5. It can be observed that the scattered light intensity greatly depends on the viewing angle. The viewing angle is typically restricted to 90° for planar PIV investigations due to limits of the depth of focus of the imaging system which fails to utilize the high intensity forward scattering.

When selecting a tracer particle, a balance must be made between minimizing the diameter to achieve proper aerodynamic characteristics and maximizing the diameter for higher Mie scattering. Many different particles have been utilized in a wide array of PIV investigations (Hinds, 1982). Most aerodynamic applications use oil based or Di-Ethyl-Hexyl-Sebacat particles to seed the flow (Raffel *et al.*, 2007). The mean particle diameter of oil based particles are 1 μm (Kähler *et al.*, 2002; Melling, 1997). Another common seeding method for wind tunnel applications is to use smoke generators (Raffel *et al.*, 2007). Smoke

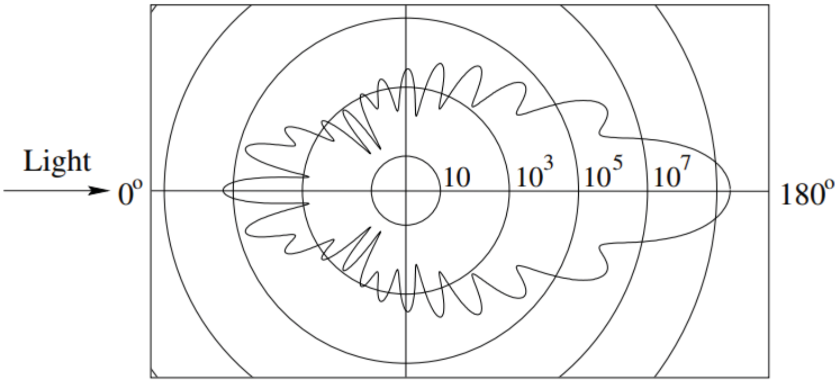

Figure 2.5: Polar spectrum of light scattering from a 532 nm incoming light by a 1 μm oil particle in air using Mie scattering theory (Raffel *et al.*, 2007).

generators are commercially available and easily implemented for wind tunnel seeding.

2.3.3 Imaging

Imaging particles that are on the order of micrometers requires a high intensity light source that enable the imaging system to detect the light scattering. Typical PIV measurements are performed using a laser as the particle illumination source. Lasers have the ability to emit monochromatic light at high energy in short pulses, which well suits the application in PIV. The beam emitted from a laser can be easily manipulated using a combination of light optics to form a thin sheet that covers the measurement region. A number of types of lasers have qualities that can be applied to different PIV applications (Raffel *et al.*, 2007).

The particles that are imaged have a diameter that is a combination of the optical imaging (Md_p), and the diffracting imaging estimated as

$$d_{diff} = 2.44 f_{\#}(M+1)\lambda \tag{2.3}$$

where $f_{\#}$ is the f-number of the imaging system, M is the magnification, and λ is the wavelength of incoming light. For small particles, the diffraction effect contribution is much greater than the optical imaging and thus the imaged particle diameter is governed by d_{diff} (Raffel *et al.*, 2007). The imaged particle diameter is recommended to be at least the size of one pixel to avoid peak-locking effects. The optimum particle image diameter for cross-correlation of two images is slightly larger than 2 pixel (Raffel *et al.*, 2007). A defocusing technique can be implemented to blur particles that are too small to an optimal image size by shifting the focus plane. The focus plane has a depth of field defined by

$$\delta_z = 2 f_{\#} d_{diff}(M+1)/M^2 \tag{2.4}$$

The depth of field is recommended to be at least the thickness of the measurement to ensure that all of the particles in the measurement region are in focus.

2.3.4 Image Evaluation

The images captured in PIV measurements contain intensity peaks associated with the particle locations for a measurement region. To obtain a spatially resolved field, the measurement region is typically divided into smaller sub-regions called interrogation windows. The interrogation windows govern the resolution of the vector fields computed. The recommended number of particles within an interrogation window was determined by Keane and Adrain (1992) to be 10 particles for planar PIV. In double frame recording systems a normalized cross-correlation is performed on the interrogation windows of successive images. The correlation coefficients are computed using a fast Fourier transform in the frequency domain. A resulting correlation peak is used to determine the image particle shift between the two time instances. Using a calibration mapping the sensor dimensions to the measurement field and the known time step between the two images, a velocity can be computed. Figure 2.6 illustrates the cross-correlation process for double frame, single exposure PIV measurements.

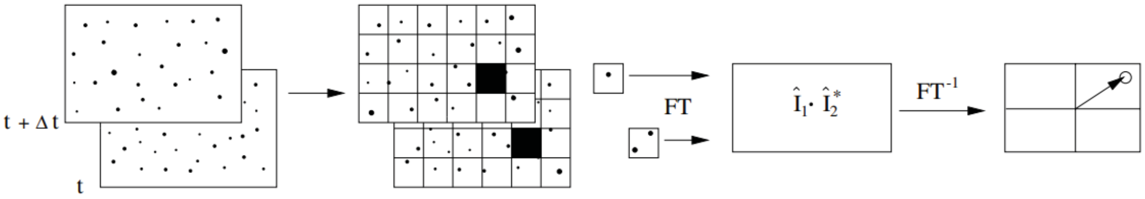

Figure 2.6: Cross-correlation analysis flow chart for double frame, single exposure PIV measurement (Raffel *et al.*, 2007).

2.3.5 Stereoscopic PIV

Stereoscopic (Stereo) PIV utilizes two cameras at off-axis viewing angles to allow an out-of-plane velocity component to be resolved across a region of interest (Prasad, 2000). The two cameras record simultaneous, but different perspectives of the region of interest which are then reconstructed to a three-dimensional field of view. The distinct camera perspectives cause the displacements detected by the camera sensor to be different, as shown in Figure 2.7. The velocity components of the particle can be reconstructed following Raffel *et al.* (2007) as,

$$U_{particle} = \frac{U_1 \tan\alpha_2 + U_2 \tan\alpha_1}{\tan\alpha_1 + \tan\alpha_2}, \tag{2.5a}$$

$$W_{particle} = \frac{U_1 - U_2}{\tan\alpha_1 + \tan\alpha_2}. \tag{2.5b}$$

The cameras can be positioned in several arrangements, as shown in Figure 2.8. Figure 2.8a shows the cameras positioned on the same side of the laser sheet. The disadvantage of this configuration is that the two cameras will experience different particle intensities due

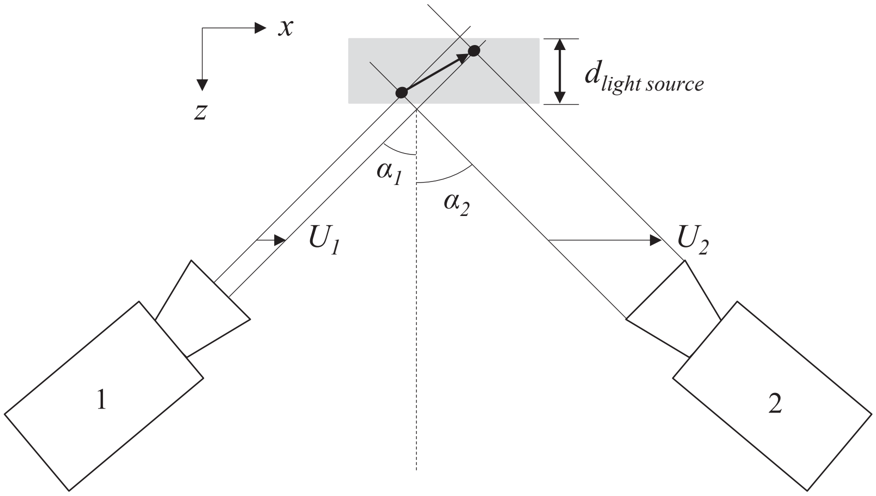

Figure 2.7: Stereo PIV imaging configuration showing the breakdown of the velocity components detected by each camera.

to the Mie scattering of the light source. Figures 2.8a and 2.8b show the cameras positioned on each side of the laser sheet. The particle reflection in these configurations will yield similar intensities, however, a transparent or two-sided calibration target is required to correctly map the geometry of the measurement region to the camera sensors.

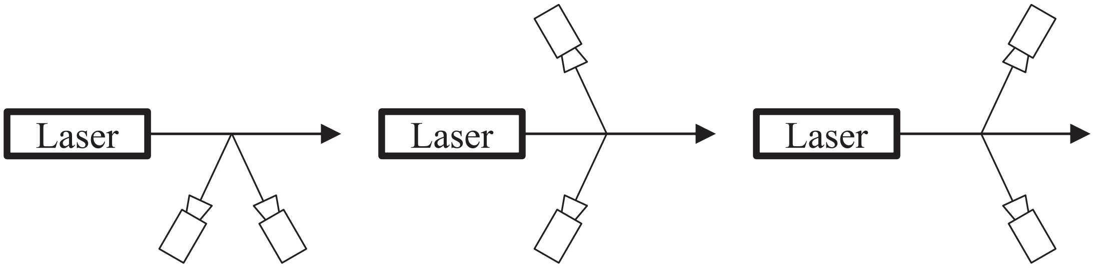

(a) (b) (c)

Figure 2.8: Common camera configuration used in stereo PIV measurements.

Chapter 3

Experimental Setup

This chapter outlines the facility, equipment, and measurement techniques used to perform the investigations. The described facilities and equipment have been used to generate and measure the flow fields for the experiments. The first investigation was to characterize the aerodynamics of the helicopter model by measuring the three components of forces and moments over a variety of flight conditions. The next investigation was to analyze the effect of the rear-fuselage design and side-slip angle of the development of the fuselage wake. The wake region of the flow field was analyzed using stereo and multiple-camera planar PIV techniques.

3.1 Wind Tunnel Testing Facility

The experiments were performed in the two story closed-loop wind tunnel facility in the Mechanical Engineering Building at the University of Alberta. The wind tunnel has a 1.2×2.4 m^2 rectangular test section which can achieve wind speeds up to 35 m/s. The wind speeds were produced by a 3 m diameter fan that was powered by a 150 kW DC electric motor. The lower test section has a contraction ratio of 6.3:1 while utilizing three fine meshes and turning vanes at the four bends to condition the flow. At wind speeds greater than 2 m/s, the turbulence intensity was documented to be less than 0.4% in the central region of the test section (Kostiuk *et al.*, 2004). The test section has an approximate length of 11.8 m and the experimental model was located 2.3 m downstream of the converging section of the wind. The helicopter model was situated in the wind tunnel such that at the most extreme test conditions, the model had 15 cm clearance from any wall. Two Pitot tubes and two thermocouples located 0.6 m from the side wall at distances 1.4 m and 5.0 m downstream of the converging section were used to provide live readings of the dynamic pressure and temperature which were presented on a digital display. The Pitot tubes and thermocouples were also used calculate flow velocity and humidity.

The lower test section underwent modifications to incorporate glass and acrylic section to provide access for illumination and imaging of PIV measurements. The side walls of the lower test section were made up entirely of 19 mm (0.75 inch) acrylic. Two wooden roof panels and two floor panels were replaced with acrylic. One of the acrylic floor panels had a 230×90 mm^2 rectangular slot removed to allow for the helicopter support structure to pass through at different locations and angles.

3.2 Helicopter Model

The experiments were carried out to determine the aerodynamic characteristics of a helicopter fuselage, shown in Figure 3.1, in various flight conditions. It was desired to isolate the aerodynamic forces acting on the fuselage from those resulting from the spinning rotor. To achieve this, designs were implemented into the support system in order to decouple the forces and torques of the rotor system.

Figure 3.1: Helicopter model mounted in the University of Alberta Wind Tunnel showing the rotating rotor and a laser sheet used for PIV measurements.

The helicopter model consisted of a modified remote control (R/C) helicopter, used emulate the downwash, and a 3D printed fuselage, a shown in Figure 3.2. A combination of various mechanical supports were used to position and finely adjust the helicopter to the desired orientation. An array of instrumentation were used to operate the rotor system, as well as to display and collect data.

3.2.1 Fuselage

The size of the fuselage corresponds to a 3% blockage ratio at zero angle of incidence and a maximum of 9% at $\alpha = 0°$ and $\beta = 90°$. The fuselage was modeled in Solidworks 3D computer aided design (CAD) using measurements generated from a 3D scanner. The fuselage was separated into three main components due to 3D print volume limitations and

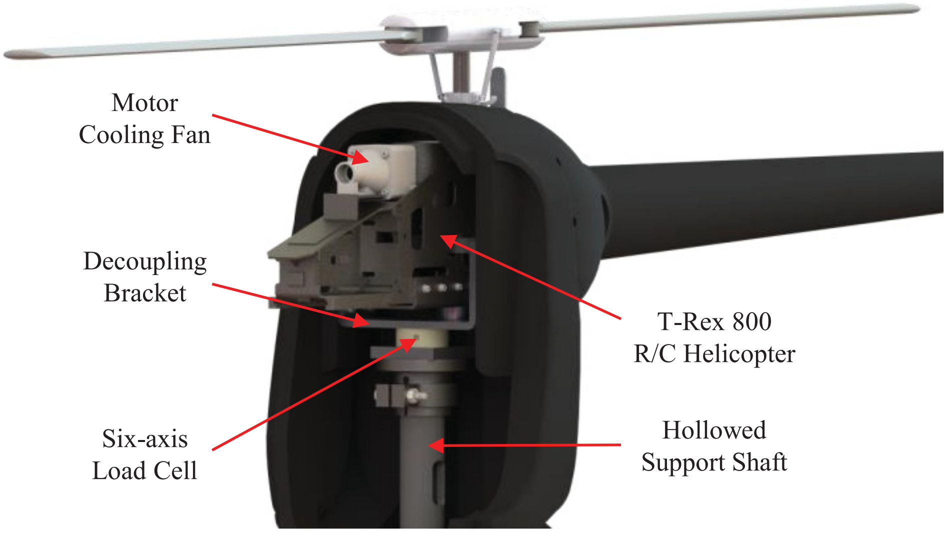

Figure 3.2: Sectioned view of the helicopter model showing the internal components.

also to ease the assembly process. The three main sections of the fuselage were printed from black ABS plastic. The smaller components components including the rear fuselage appendages and the drive shaft plug were also printed. The "Nose" section of the fuselage was primarily hollow and housed the counter weight assembly. The counter weight assembly consisted of a flat plate with a threaded rod that was epoxied to lower surface on the interior of the nose. Several weights were machined to assist in minimizing the initial torque acting on the load cell. The "Back" section of the fuselage was used as the main connection point to the fuselage. A circular hole was specified in order to pass the support shaft through to the load cell brackets without contacting the fuselage. The back section also served as the connection to the load cell. The "Tail Boom" was printed in three sections due to its length not fitting in the 3D printer volume. A removable 249 mm tail boom section was designed to allow for the model to properly fit in the wind tunnel at a side-slip angle of $\beta = 90°$. All of the components were fitted together using protruding lips around the edges of mating components. The protruding lips contained threaded inserts that allowed the parts to be bolted together. The outer surfaces of the fuselage underwent a surface smoothing process to minimize the skin friction. All of the outer surfaces were sanded and then covered with a drywall filler to fill the gaps between the print layers. Once covered with the drywall filler, the surface was once again sanded with a finer grid. The final surface was then painted with a matte black spray paint to minimize the reflection of the laser sheet off of the fuselage surface.

Four rear fuselage designs were compared throughout the investigation, as outlined in Figure 3.3. The baseline configuration was modelled based on a helicopter with an externally mounted motor, with simplified geometry. To investigate the significance of this geometry the fuselage was also tested with the simplified motor geometry removed (C1).

Two additional cases were designed with the goal of providing an aerodynamic casing for the simplified motor geometry, namely the cusped case and the round case.

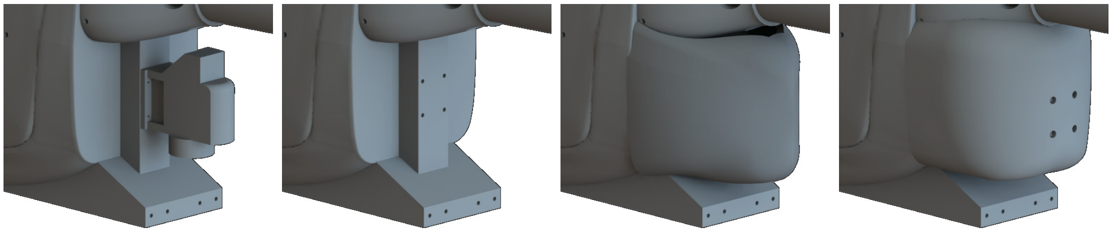
(a) Baseline (b) Empty (c) Cusped case (d) Round case

Figure 3.3: Rear fuselage appendages studied in the investigation.

The cusped case was designed to delay the flow separation and to reduce the size of the wake in the aft-body region of the fuselage. The design was shaped based on a tangential spline from the back edge of the fuselage and connecting with a cusp at the trailing edge. Two passageways with removable plugs were designed to allow for flow to pass from one side of the body to the other in high side-slip orientations. A 10 mm gap through a horizontal section of the case was designed with the intent to allow for a laser sheet to pass through. The outer surface of the gap was fitted with a transparent acrylic sheet that formed to the shape of the case. It was later found that the transparent slice was not adequate at allowing the laser sheet to pass through without being disrupted.

The round case was also designed to delay the flow separation, however, with more emphasis on the higher side-slip angles. The round case maintains a constant curvature as it encloses the original simplified geometry. The overall length of the round case was 10 mm shorter than the cusped case. The round case had a more blunt trailing edge that may consequently reduce the drag performance at low side-slip angles.

3.2.2 Rotor System

A T-Rex 800E R/C helicopter was used to reproduce the downwash in the flow field. In order to accommodate the T-Rex helicopter into the 3D printed fuselage, modifications had to be made to the frame. The tail rotor was not required for the investigations and thus the tail rotor servo was removed to free up space in the rear section of the frame. The batteries were stored externally which enabled the housing to be removed to shorten the height of the frame. A minimum distance of 6 mm existed between the fuselage and T-Rex frame at any point in the model.

The original blades had a span of 800 mm and were replaced with 600 mm span blades from a T-Rex 600 R/C helicopter. Align 600 mm 3G Carbon Fiber Blades were used to produce downwash on a smaller section of the fuselage and to ensure that the blades did not interfere with the boundary layer of the wind tunnel. The main rotor diameter of 1.2 m corresponds to a rotor diameter to wind tunnel width ratio of 0.5. This ratio was selected base on the investigation by Langer *et al.* (1996) as the ratio of 0.5 coincided with the smallest boundary correction factors for rectangular test sections by lowering the effective blockage of the downwash produced by the rotor. The blades have a 55 mm chord length and a 7.15 mm maximum thickness. The blades were 2 mm thinner at the grip location which required the use of two 1 mm shims on each side of the blade grips. The bolt bore diameter was 1 mm smaller which required a 1 mm bushing in the grips in order to allow for a smaller bolt.

The motor that spun the blades was a Quantum 4530-45kV brushless motor. The ten magnetic pole motor has a maximum continuous power and current of 5000 Watts and 125 Amps respectively. The motor can spin the blades from a threshold speed of 1050 RPM to a maximum speed of approximately 2500 RPM. The speed was governed by the Electronic Speed Control (ESC). A Phoenix Edge HV 160 Amp electronic speed controller (ESC) from Castle Creations was used to control the speed of the rotor. The ESC was powered by two 5000 mAh 6S1P 45C Li-Po batteries wired in series. The auxiliary wire was used to measure the speed of the motor by counting the number of rising edges of the output signal. The signal was then converted to the RPM by dividing the number of magnetic poles and then converting from frequency to angular speed.

3.2.3 Mounting System

In order to adjust the pitch and yaw angles, a configuration was designed to allow the model to rotate in the wind tunnel. The mounting system consisted of an adjustable rolling table, titling-rotary table, support shaft, decoupling mount, and mounting brackets. The adjustable rolling table was used as a base for the system. The rolling table allowed for the system to be moved around the laboratory on its casters and to be lifted from its casters to provide a more stable base. The height of the table could be adjusted up to 330 mm from its base height. In order to finely adjust the angle-of-attack and side-slip angle, a Weiss 300 mm tilting rotary table was mounted on the rolling table. The rotary table has 1/60° graduations for adjusting both the side-slip angles, and the tilting angle which corresponds to the angle-of-attack. Since the rotary table could only tilt in one direction, a specialized mount for the support shaft was designed with a 20° offset angle which enabled the helicopter to be mounted with a negative angle-of-attack.

A 38.1 mm (1.5 inch) connection plate secured the support assembly to the rotary table. The support shaft had an outer diameter of 38.1 mm (1.5 inch) and had a hollowed out center to allow for the cables of the instrumentation to pass through without extruding into the flow field. The support shaft was secured to the connection plate and the decoupling mount using bolted on flanges that were compressed to the support shaft with a clamping ring. The load cell and rotor system were attached to the support shaft using a decoupling mount, as shown in Figure 3.4. The decoupling mount was designed to isolate the forces acting on the fuselage from the thrust and torque produced by the rotor. Figure 3.4a shows that the rotor system can be mounted within the fuselage with no points of contact. The fuselage was mounted directly to the load cell through a U-shaped bracket, as shown in Figure 3.4b. The rotor system was connected on a separate portion of the decoupling mount and had a minimum of 6 mm clearance from the fuselage at any point in the model.

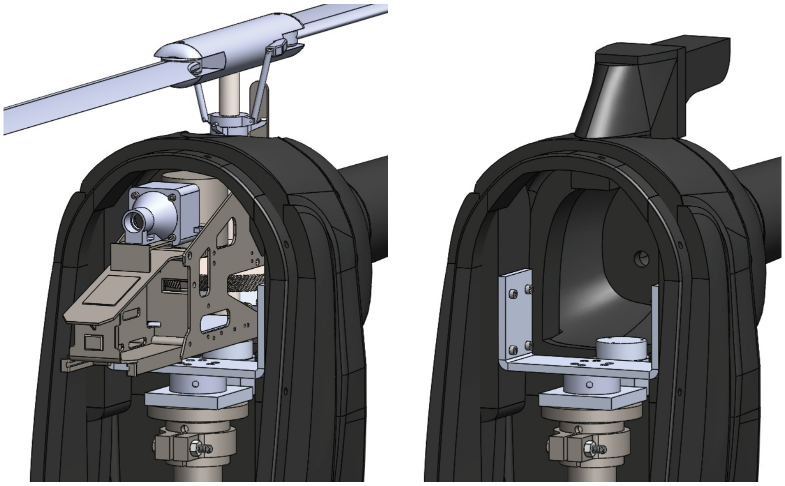
(a) Rotor Equipped Model (b) Isolated Fuselage

Figure 3.4: Comparison of the rotor equipped model to the isolated fuselage configuration showing the load cell decoupling mount system.

3.3 Instrumentation

Instrumentation was implemented to control the operational parameter and to record the load measurements and rotor data. A six-axis load cell was used to measure the aerodynamic forces acting on the fuselage. The main rotor and cooling system were controlled through a LabVIEW based interface. The load cell and rotor data were exported as a comma separated values and processed using MATLAB scripts.

3.3.1 Load Cell

The six-axis load cell that was used for the experiments was the Mini45 with the SI-580-20 calibration from ATI Industrial Automation. The sensing range and uncertainty of each component is outlined in Table 3.1.

	f_x	f_y	f_z	τ_x	τ_y	τ_z
Range	±580 N	±580 N	±1160 N	±20 N-m	±20 N-m	±20 N-m
Resolution	1/4 N	1/4 N	1/4 N	1/188 N-m	1/188 N-m	1/376 N-m
Uncertainty	1.25%	1.75%	1.00%	1.75%	1.25%	1.00%

Table 3.1: Measurable range, resolution, and uncertainty for the Mini45 six-axis load cell.

Since the load cell axis did not coincide with the estimated center of mass of the helicopter, as shown in Figure 3.5, an axis transformation was required. Equation 3.1 shows the rigid body transformation used to resolve the load measurements about the center-of-mass, following Murray *et al.* (1994) as

$$\begin{bmatrix} f_{COM} \\ \tau_{COM} \end{bmatrix} = \begin{bmatrix} R^T_{LC-COM} & 0_{3\times 3} \\ -R^T_{LC-COM}\hat{p}_{LC-COM} & R^T_{LC-COM} \end{bmatrix} \begin{bmatrix} f_{LC} \\ \tau_{LC} \end{bmatrix} \tag{3.1}$$

where R is the rotation matrix, and p is the position vector describing the relative rotation and position between the axes of the load cell and center-of-mass, denoted by subscripts LC and COM, respectively.

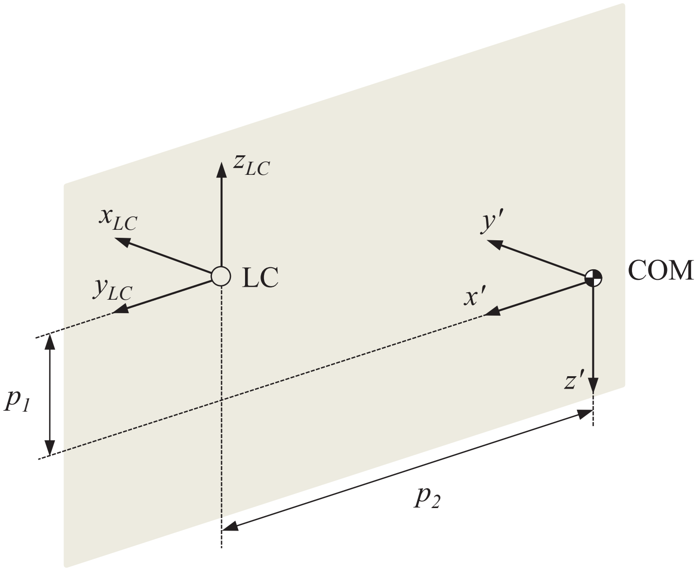

Figure 3.5: Location of the load cell (LC) axes relative to the body fixed axes with origin at the center-of-mass (COM). Components p_1 and p_2 of the position vector ($\boldsymbol{p}$) are shown to relate the two coordinate systems.

The resulting forces and moments could then be described about a body fixed axis with an origin at the center-of-mass, as shown in Figure 3.6. The roll moment was defined about a longitudinal axis spanning from the nose to the tail, the pitch moment was defined about a lateral axis spanning from the port to starboard side, and the yaw moment as defined about the vertical axis. The positive rotation directions of the moments are shown in Figure 3.6.

The orientation of the helicopter in the wind tunnel was defined with respect to the wind axis by the angle-of-attack and side-slip angle, as shown in Figure 3.7. The aerodynamic drag, side, and lift force coefficients were defined about the wind axis.

3.3.2 Main Rotor and Cooling System Control

The motor, cooling fans, and servos were controlled using an Arduino board. The control interface was ran through a LabVIEW Virtual Instrument. The motor speed and servo

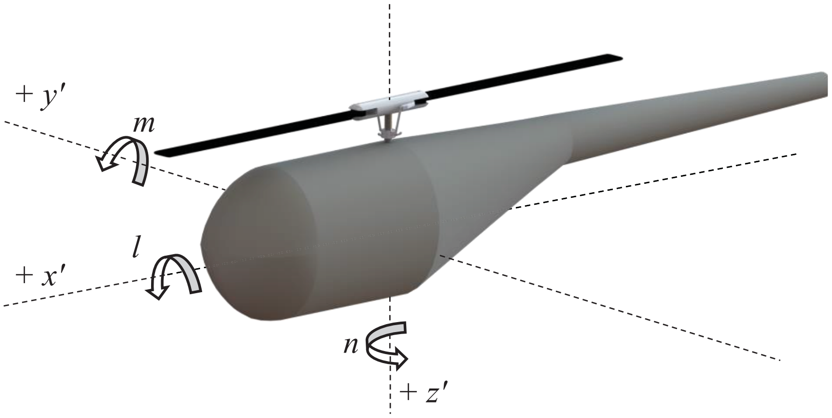

Figure 3.6: Body fixed axes showing definition of the roll, pitch, and yaw moments with respect to the approximate location of the center-of-mass.

positions were controlled using a pulse width modulation (PWM) signal with a 50 Hz frequency. The cooling fans were toggled on and off with power from a 12 V source. The control signals sent to the servos update once every second.

The servo positions were adjusted to control the collective and cyclic pitch of the helicopter. The collective control was achieved by mapping the PWM signal of the servo position to the pitch angle of the blades. The lateral and longitudinal cyclic controls were determined based on the tilting of the swashplate. Using the geometry of the swashplate, the mapping to the servo location were described by Equation 3.2.

Servo position mixing:

$$s_{prt} = \theta_{col} + \theta_{cyc,lat} + 0.5\ \theta_{cyc,lon}, \tag{3.2a}$$

$$s_{stb} = \theta_{col} - \theta_{cyc,lat} + 0.5\ \theta_{cyc,lon}, \tag{3.2b}$$

$$s_{aft} = \theta_{col} - \theta_{cyc,lon}. \tag{3.2c}$$

A cooling system was implemented to assist in regulating the motor and electronic speed controller (ESC) temperatures between testing periods. The motor temperature was monitored using an Omega HH506 Thermometer to determine if breaks were required between measurements to allow for the motor to cool. Two 30 mm diameter tube-axial fans capable of 14.8 L/s (31.3 CFM) were used to move the warm air surrounding the motor and ESC. Rubber tubing with a 12.7 mm (0.5 inch) inner diameter was used to exhaust the air out the tail boom of the helicopter. After testing the system, it was determined that the diameter of the tubing was too small and was restricting the flow from the fans. The resulting solution was to remove the tubes and to instead take off the nose component of the fuselage to allow the cooling fan to move the air into the test section of the wind tunnel. The combined effect of the cooling fans and the wind tunnel operating at a low speed helped accelerate the cool down period.

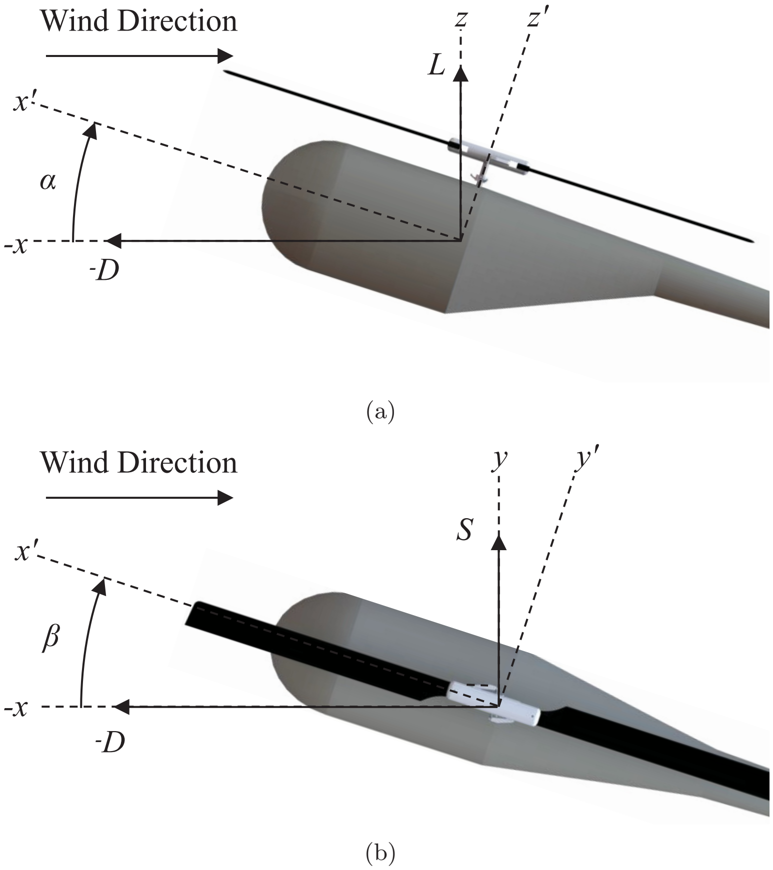

(a)

(b)

Figure 3.7: Wind axis definition showing the the angle-of-attack and side-slip angle with respect to the body fixed axis. Drag, side, and lift forces are defined with respect to wind axis.

3.4 Particle Image Velocimetry

3.4.1 Stereo-PIV

The stereoscopic PIV investigation was performed to characterize the effect of the main rotor downwash on the wake of the rear fuselage for various angles-of-attack. Particle illumination was provided by a dual-cavity Nd:YAG laser (Spectra-Physics, PIV-400-10) that outputs a 532 nm light beam at 400 mJ per pulse and with a pulse width of 5-8 ns. The light was directed to the region of interest using three adjustable mirrors and formed into a laser sheet with a 2 mm thickness using a series of cylindrical and spherical lenses. The particles were provided remotely using two smoke generators (Antari W-515D, American DJ Fogstorm 1700HD) located in the upper test section of the wind tunnel. The smoke machines produced glycol-based water particles that have an average diameter of approximately 1 μm. Two Imager ProX CCD cameras (LaVision GmbH) with a 2048×2048 pix sensor with a 7.4×7.4 μm^2 pixel size and a 14-bit resolution were used to capture the field of view. Two Scheimpflug adapters were used to to assist in maintaining the full field of view within the focus plane. Two Nikon lenses with focal lengths of 60 mm were used with an aperture settings of $f/4$. The schematic in Figure 3.8 show the relative position and the corresponding field of view (FOV1). The two cameras were positioned at a working distance of 1170 mm and 1160 mm with viewing angles of 90° and 55° respectively. The field of view for the stereo-PIV measurements was located 180 mm above the bottom surface of the fuselage in the xy plane and had dimensions of 275×275 mm^2 ($x\times y$) depicted by FOV1 in Figure 3.8. A 3D calibration of the FOVs, using a Type 22 calibration plate (LaVision GmbH) with 3 mm dot diameters and 15 mm dot spacing was performed prior to a self-calibration on particle images as described in Wieneke (2005). The stereo-PIV data were processed using DaVis 8.3 (LaVision GmbH) with an interrogation window size of 64×64 pix (8.4×8.4 mm^2).

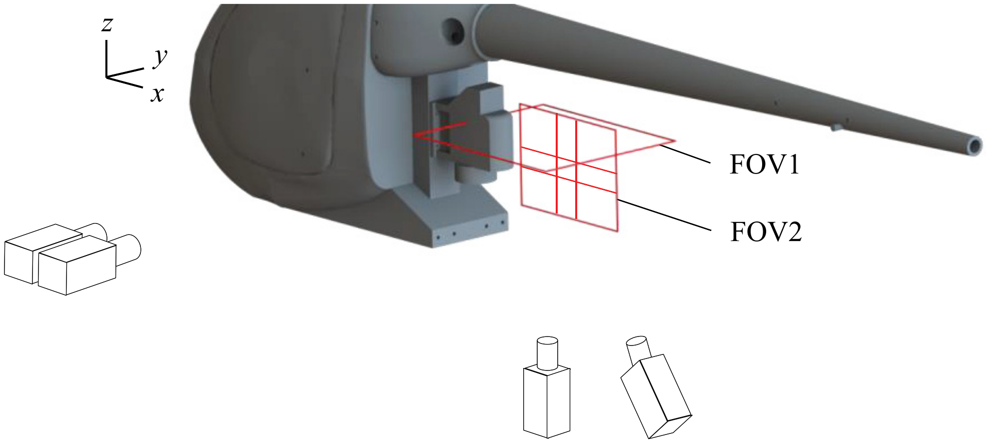

Figure 3.8: Combined stereo- and planar-PIV setups showing approximate camera positions and field of view locations with respect to the helicopter fuselage.

A supplementary planar PIV investigation was performed to capture an intersecting field of view in the xz plane. Illumination was provided using the same Nd:YAG laser as the stereo-PIV measurements. Two Imager Intense CCD cameras (LaVision GmbH) with 1376×1040 pix sensors with a 6.45×6.45 μm^2 pixel size and a 12-bit resolution were used to image the field of view. Each camera was located at a working distance of 1350 mm and had a field of view of 120×90 mm^2. Two separate measurements were performed with the field of views offset vertically within the xz plane. The results were stitched together in MATLAB using the known overlap regions to produce a combined field of view of 210×150 mm^2 (FOV2). The field of view was located 200 mm downstream of the rear surface of the fuselage and 70 mm above the bottom surface. The cameras were calibrated the same Type 22 calibration plate (LaVision GmbH) as in the stereo-PIV measurements. The planar data were also processed in DaVis 8.3 (LaVision GmbH) using an interrogation window size of 32×32 pix (2.8×2.8 mm^2).

3.4.2 Four-Camera Planar PIV

Planar PIV measurements with a high dynamic range were performed to analyze the wake of the rear fuselage for varying side-slip angles both with and without the rotor downwash. The same Nd:YAG laser and particle supply system was used as in the stereo-PIV investigation. The light was directed to the region of interest using three adjustable mirrors and formed into a laser sheet with 2 mm thickness and approximately 370 mm width using a series of cylindrical and spherical lenses. Four Imager ProX CCD cameras (LaVision GmbH) were used to capture the field of view. Each camera was equipped with a Nikon 50 mm lens with an aperture setting of $f/2$. The camera setup shown in Figure 3.9a consists of two horizontally mounted cameras (number 1 and 2) viewing into 45° angled front-surface mirrors, and two vertically oriented cameras (number 3 and 4). The horizontally mounted cameras were oriented as such due to space restrictions between the bottom panel of the wind tunnel and the supporting structures of the helicopter setup. A rail was supported horizontally where the two cameras and angles viewing mirrors were mounted. The setup enabled the position of the cameras to be adjusted in three directions to capture the field of view. The imaged region was comprised of four slightly overlapping field of view of 188×188 mm^2 in the xy plane of the aft-body Figure 3.9b. Approximately 10% overlap of each adjacent region allowed for a combined FOV of 355×355 mm^2. The field of view was located 150 mm from the bottom surface of the fuselage. The cameras were calibrated using a customized 370×260 mm^2 calibration plate consisting of 2 mm dot diameters and 5 mm dot spacing. The working distances of the cameras were 735 mm and images were captured with a digital resolution of 0.092 mm/pix.

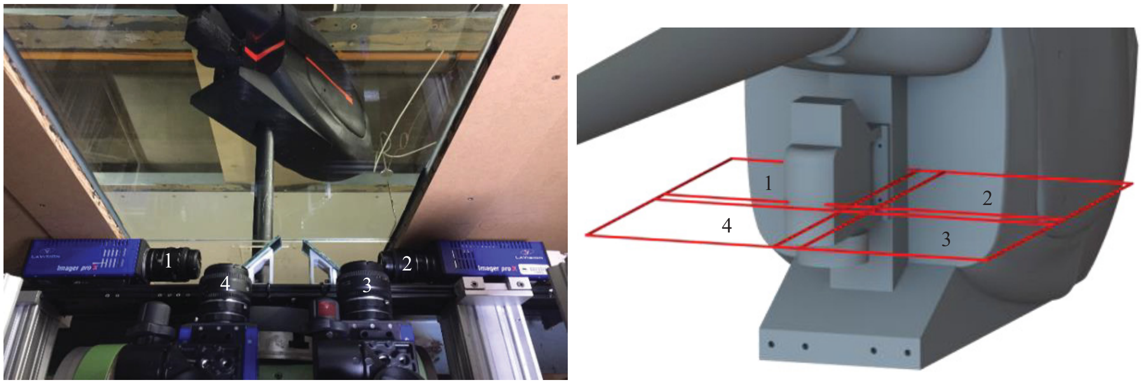

(a) (b)

Figure 3.9: (a) Four camera planar PIV setup showing horizontally mounted cameras, (b) field of view size and location with respect to the helicopter fuselage.

The background noise of the raw images was reduced by subtracting the minimum value of the ensemble images. A geometric mask was applied to avoid vector calculations in the regions where the aft-section of the fuselage protruded into the FOV. The data from rotor equipped measurements required additional image enhancement steps to be performed prior to cross-correlation as a result of the high reflectively of the main rotor blades passing through the background of the FOV. An algorithmic mask was defined by setting a maximum intensity threshold corresponding to the blade reflection intensity to mask out the rotor as it passed through the background of the FOV. The data were processed in DaVis 8.3 (LaVision GmbH) using interrogation windows of 96×96 pix (8.81×8.81 mm^2) and 75% window overlap. The FOV of each camera was merged in DaVis 8.3 (LaVision GmbH) through the use of a common coordinate system defined on the custom calibration plate.

Chapter 4

Characterization of Fuselage Aerodynamics

This chapter outlines the investigation performed to characterize the aerodynamics of the baseline configuration over a wide array of flight conditions. The intent of the investigation was to discover anomalies in the aerodynamic loading that may be problematic to the safe operation of the helicopter. Six-axis load cell measurements were performed for -15° $\leq \alpha \leq$ 15° at $\beta = 0°$ and for $0° \leq \beta \leq 180°$ at $\alpha = 0°$. A stereo- and planar-PIV campaign were carried out in the wake of the fuselage to analyze the development of the separation bubble and to characterize the effect of the main rotor downwash for -5° $\leq \alpha \leq$ 5° at $\beta = 0°$.

4.1 Load Measurements

The aerodynamic loads measured by the six-axis load cell are presented as dimensionless force and moment coefficients, defined as

$$C_f = \frac{f}{\frac{1}{2}\rho_\infty U_\infty^2 A_{ref}} \tag{4.1a}$$

$$C_\tau = \frac{\tau}{\frac{1}{2}\rho_\infty U_\infty^2 A_{ref} c} \tag{4.1b}$$

where f and τ are the force and moment vectors defined about the center of mass, respectively. The reference length (c) was defined as the fuselage width, and the reference area (A_{ref}) was defined as the frontal area at zero angle of incidence.

4.1.1 Forward Flight Condition at Zero Side-Slip

The first test condition that was tested was forward flight. Figure 4.1 shows the dimensionless force and moment coefficients for -15° $\leq \alpha \leq$ 15° at zero side-slip. The measurements were swept from α = -15° to 15° in 2.5° increments. Each angle-of-attack was recorded for 120 s at 100 Hz and the resulting measurements were averaged over the 120 s testing period to determine the forces and moments acting about the load cell axis. Uncertainty in the load cell measurements is analyzed in Appendix A. A representation of the load cell measurements over the 120 s testing period is presented in Appendix B to show the stability of the measurements over the collection period.

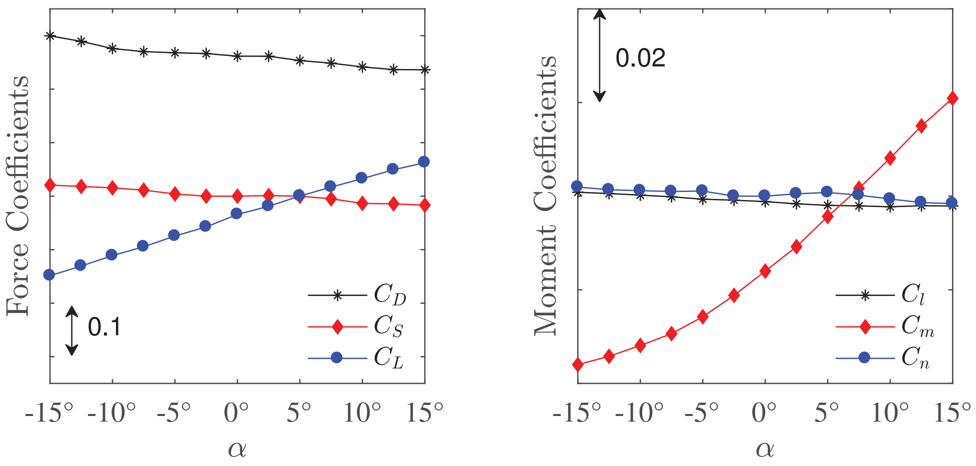

(a) (b)

Figure 4.1: (a) Force coefficients and (b) moment coefficients for the baseline configuration with varying angle-of-attack at zero side-slip.

Figure 4.1a shows the drag, side, and lift force coefficients over the swept range of angle-of-attack. It can be observed that the drag coefficients (C_D) have the highest magnitude throughout the entire range of α. The high drag coefficients are expected since the fuselage is a bluff body and the formation of a separation region in the wake contributes to a large pressure drag. A small and steady decrease in drag is noticed with increasing angle-of-attack. Seddon and Newman (2011) suggests that the transition from negative to positive angle-of-attack results in a change in flow topology of the wake that depends on the upsweep angle of the rear fuselage. For negative α, the wake produces streamwise vortices while for positive α, the flow transitions to form spanwise vortices as shown previously in Figure 2.2. The change in flow topology was predicted to result in a sudden decrease in drag, though no such pattern is experienced for the drag coefficients shown in Figure 4.1a. The upsweep of the fuselage tested in this investigation is sharp (90°) and mitigates the change in flow topology, thus resulting a steady decrease with no sudden drop in drag. Several experimental investigations (Reß *et al.*, 2015; Stepanov *et al.*, 2016; Zanotti *et al.*, 2016; Jenkins Jr. *et al.*, 1962) noticed that as the angle-of-attack is increased, the drag plateaued near $\alpha = 0°$, and in some cases began to rise as the angle-of-attack was increased into positive values. In Figure 4.1a, the drag coefficients do not exhibit this pattern and instead decrease as the angle-of-attack becomes more positive.

The lift coefficients (C_L) in Figure 4.1a follow a consistent linear rise with increasing angle-of-attack. This agrees with many experimental studies performed over a similar angle-of-attack range (Reß *et al.*, 2015; Jenkins Jr. *et al.*, 1962; Filippone, 2007). The zero-lift angle-of-attack occurs at approximately $\alpha = 5°$, and the lift coefficients for $\alpha < 0°$ are negative. The negative lift coefficients indicate a downforce that opposes the effort of the main rotor to maintain altitude. The most common helicopter flight conditions occur when $\alpha \leq 0°$, thus the additional downforce from the fuselage serves to decrease the fuel economy of the helicopter for the majority of its operation.

The side force coefficients (C_S) in Figure 4.1a are approximately zero across the tested angle-of-attack range. This is expected due to symmetry of the fuselage about the central $x'z'$ plane. A small negative slope is noticed approximately centered at $\alpha = 0°$, which may be indicative of a small misalignment of the tilting axis of the rotary table in the experimental setup, or manufacturing asymmetry of the 3D printed model. The misalignment would introduce small side-slip angles as the angle-of-attack is varied, which only introduces the small errors when the angle-of-attack is varied. Since the resulting side-force is small relative to the other forces, no corrections were made to the load cell data for this misalignment.

Figure 4.1b shows the dimensionless roll, pitch, and yaw coefficients over the tested angle-of-attack range. The roll (C_l) and yaw (C_n) moment coefficients are approximately zero throughout the range of angle-of-attack, conforming to the expectations based on the symmetry of the fuselage about the $x'z'$ plane. Similarly to the side force coefficients in Figure 4.1a, the roll and yaw moments have a small decreasing slope as a result of the misalignment. The pitch moment coefficients (C_m) in Figure 4.1b show a positive growth with increasing angle-of-attack. The slope of the pitch moment ($\mathrm{d}C_m/\mathrm{d}\alpha$) remains approximately constant for $2.5° \leq \alpha \leq 15°$ and decreases as α is reduced from $\alpha = 2.5°$ to -15°, as shown in Figure 4.2. The pitching moment at $\alpha = 0°$ is negative, which induces a nose-down motion. These trends have been noticed in investigations over similar ranges of angle-of-attack (Sweet and Jenkins Jr., 1962; Howlett, 1981). The pitch moments transition from negative to positive values at approximately $\alpha = 7°$.

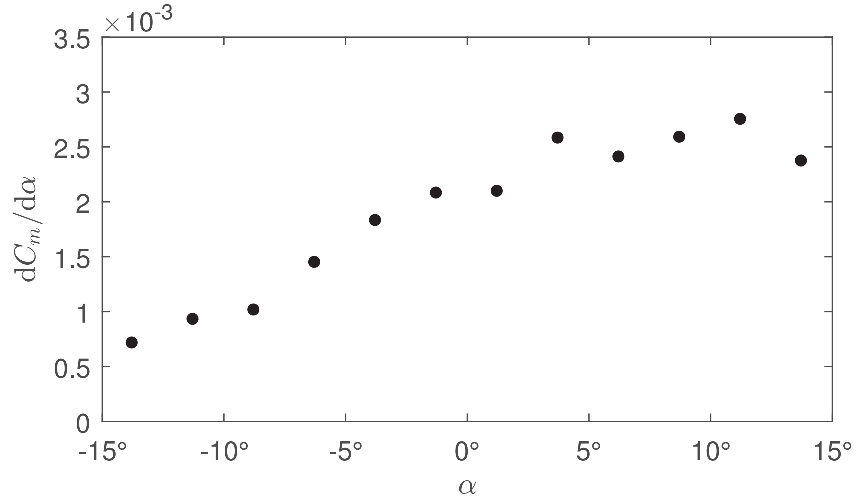

Figure 4.2: Slope of the pitch moment with respect to angle-of-attack ($\mathrm{d}C_m/\mathrm{d}\alpha$).

The static stability of an aircraft describes the response to angular disturbances, and its ability to return to the original flight condition (Seddon and Newman, 2011). If the aerodynamic reaction to an angular disturbance causes a moment that corrects to the original position, the fuselage is considered statically stable. If the aerodynamic reaction causes a moment that further displaces the helicopter from its original position, it is considered statically unstable. The static stability of an aircraft can also relate to the dynamic stability, since statically unstable motions are also dynamically unstable, while statically stable motions can be either dynamically stable or unstable (Seddon and Newman, 2011). The constraints of the static stability of the fuselage aerodynamics depends on the original trim of the helicopter. Figure 4.2 shows that the slope of the pitching moments with respect to the angle-pf-attack ($\mathrm{d}C_m/\mathrm{d}\alpha$) is positive over the tested range of α. The positive slope is indicative of statically unstable behaviour (Cook, 2013). When a disturbance causes a shift in the angle of attack (i.e. a downwards or upwards wind gust), the moments produced have a destabilizing effect on the fuselage with respect to the original trim.

Figure 4.3 displays both the pitch and roll moment coefficients on same polar plot to show the magnitude and direction of moments relevant to the cyclic controls of the main rotor. The combined loading of the pitch and roll moments determine direction and magnitude of the cyclic pitch applied to the main rotor for adjusting lateral and longitudinal attitude. The magnitude of the combined loading can be quantified as the distance from the origin to the data point. The angle of the moment vector can be measured as the angle between the vector drawn from the origin to the data point and the -C_l axis, in a similar fashion as the azimuth angle discussed in Figure 2.1. Both large changes in magnitude, and large angular changes can be problematic to flight operation since such changes require large corrections to keep the helicopter in the desired flight pattern. Figure 4.3 shows the resultant moments plotted from -15° to 15° in 2.5° increments. It can be seen in Figure 4.3 that the moments acting on the main rotor are primarily pitch moments and that there are no dramatic angular shifts in loading. The strongest magnitudes occur for $-15^\circ \leq \alpha \leq -5^\circ$, though the changes in magnitude are small within this range. The change in magnitude remains consistent for $0^\circ \leq \alpha \leq 15^\circ$ as noticed in Figure 4.1b.

4.1.2 Level Flight Condition at Zero Angle-of-Attack

The level flight condition was tested by performing load measurements over a wide range of side-slip angles. Figure 4.4 shows the dimensionless force and moment coefficients for $0^\circ \leq \beta \leq 180^\circ$ in 10° increments. The measurements were swept from $\beta = 0^\circ$ to 180° in 10° increments. The loads were measured at each angle and were averaged over 120 s recording period at a 100 Hz sampling rate.

Figure 4.4a shows the drag, side, and lift coefficients for tested side-slip angles. The force coefficients are defined about the wind axis in Figure 3.7, thus the drag and side force are in the streamwise and spanwise directions, respectively. It is evident that the magnitude of the force coefficients are much larger for varying side-slip in comparison to

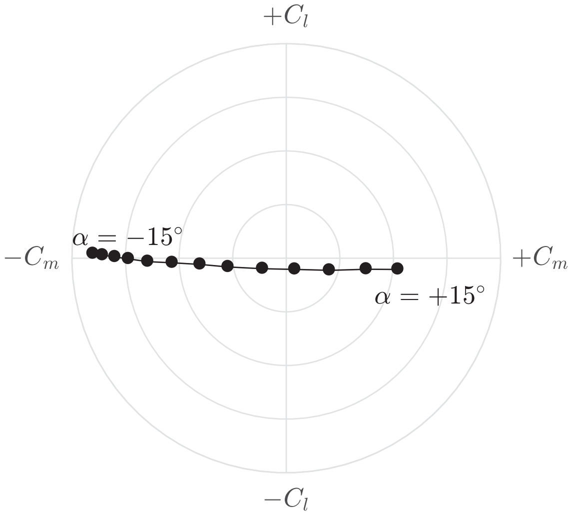

Figure 4.3: Resultant vector of the pitch and roll moment coefficients showing the changes in magnitude and direction of the moment acting in the $x'y'$ plane. The forward flight conditions are shown for -15° $\leq \alpha \leq$ 15° in 2.5° increments at zero side-slip.

the forward flight forces in Figure 4.1a. The drag force coefficients are nearly an order of magnitude larger at high side-slip angles. The high drag forces are primarily due to the large projected frontal area that is experienced as the fuselage is turned at high side-slip angles. The drag increases rapidly up to an angle of $\beta = 80°$ where it peaks. The drag decreases as β is increased from 80° to 180°. The drag at $\beta = 180°$ is greater than at $\beta = 0°$ as a result of the flatter and less streamlined geometry of the aft-body. There are few investigations of helicopters at side-slip angles that exceed $\beta = \pm 20°$ (Howlett, 1981; Brunello *et al.*, 2012). Howlett (1981) used wind tunnel data to evaluate a mathematical model for performance and handling quality evaluation. The drag was found to peak at $\beta \approx 80°$ in the wind tunnel and mathematical model results presented by Howlett (1981), showing similar results with respect to the peak location in Figure 4.4a.

The side force coefficients also have a large contribution to the aerodynamic forces acting on the body, as shown in Figure 4.4a. The side force increase up to a side-slip angle of 60° where the maximum value was recorded. The side force then decreases as the side-slip is raised to $\beta = 150°$, where the minimum value is reached. The values of C_S are positive for $0° \leq \beta \leq 100°$ and negative for $110° \leq \beta \leq 180°$. The trend in the side force is not symmetric about $\beta = 90°$ due to the asymmetry of the fuselage about the $y'z'$ plane. The side force presented for the range $0° \leq \beta \leq 80°$ by Howlett (1981) exhibited a similar trend as in Figure 4.4a, showing a peak C_S at $\beta \approx 55°$.

The lift forces coefficients in Figure 4.4a are much smaller in magnitude relative to the drag and side force coefficients. The variation of the lift force over the 10° intervals also is much smaller than those of the drag and side force coefficients. The region of the largest incremental lift occurs for $100° \leq \beta \leq 130°$, at which the helicopter would be experiencing tail and side wind components.

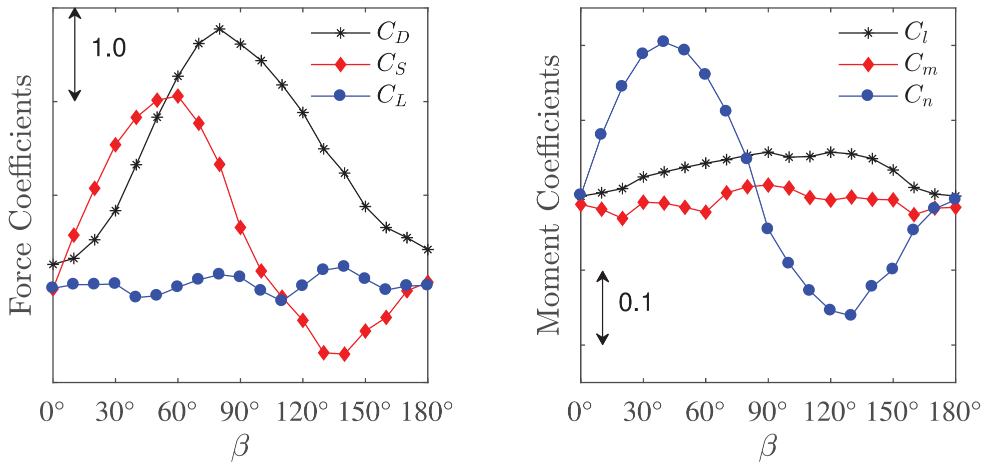

(a)

(b)

Figure 4.4: (a) Force coefficients and (b) moment coefficients for the baseline configuration with varying side-slip angle at zero angle-of-attack.

Figure 4.4b shows the roll (C_l), pitch (C_m), and yaw (C_n) moment coefficients for the tested side-slip angles. It is evident that the yaw moment has the highest magnitudes and variation with side-slip angle. This is a result of the large projected frontal area of the fuselage that is experienced at high side-slip. The center of pressure shifts greatly in the lateral direction, causing a long moment arm about the vertical axis. The tail rotor enables the helicopter to correct for large yaw moments by adjusting the tail rotor blade pitch in the positive and negative direction. The yaw moment coefficients increase up to $\beta = 40°$, where the maximum positive value is reached. The yaw moment has positive magnitude prior to transitioning to negative values at $\beta \approx 85°$. The largest negative magnitude is achieved at $\beta = 130°$, at which the magnitudes return to zero. The overall trend resembles a sinusoidal-like response over the 180° period.

Yaw moments presented by Howlett (1981) over -90° $\leq \beta \leq$ 90° exhibit a similar pattern as in Figure 4.4b with some distinct differences. The first difference is that the yaw moment has its positive peak around $\beta = 20°$, in contrast to the peak at $\beta = 40°$ in Figure 4.4b. The helicopter model in Howlett (1981) has a vertical tail stabilizer on the aft-most section of the tail boom. The vertical stabilizer serves to provide an additional side force with a long moment arm when at side-slip angles to provide a stabilizing moment while in forward flight. The stabilizing moment would result in a lower maximum yaw moment and shift the occurrence of the peak to a side-slip angle closer to zero. The second observation from Figure 4.4b which differs from that of Howlett (1981) is that the maximum positive moment at $\beta = 40°$ has a larger magnitude than the maximum negative moment at $\beta = 130°$. The magnitude of the peak in the yaw moments presented by Howlett (1981) in the side-slip range $40° \leq \beta \leq 90°$ are evidently high than the peak magnitudes in the range $40° \leq \beta \leq 90°$. This again can be attributed to the vertical tail stabilizer and the larger tail boom. The tail stabilizer and tail boom are designed to operate optimally under low side-slip conditions, and provide the dominant moment for the helicopter. A consequence of the vertical tail stabilizer is that during tail wind conditions ($90° < \beta \leq 180°$) the moment provided by the vertical stabilizer is destabilizing, causing large negative moments in that range of side-slip angles. Since the tail boom of the helicopter in this investigation is narrower than in Howlett (1981), the yaw moments are balanced more between the nose of the fuselage and the tail boom, resulting in the more sinusoidal response observed in Figure 4.4b.

The roll moment coefficients in Figure 4.4b are positive in magnitude for $0° \leq \beta \leq 180°$. The magnitudes rise with increasing side-slip up to a side-slip of $\beta = 90°$. The positive magnitudes are indicative of the greater concentration of a high pressure region above the center of mass on the upturned side of the fuselage. The roll moments approximately follow a linear increase for $0° \leq \beta \leq 90°$, with a jump discontinuity between $\beta = 20°$ and 30°, as shown in Figure 4.5. The discontinuity can be indicative of a change in wake flow that occurs between $\beta = 20°$ and 30°. Figure 4.4b shows that after $\beta = 90°$, the roll moment plateaus and begins to decrease back to zero magnitude at $\beta = 120°$. The moment coefficients for $0° \leq \beta \leq 90°$ and $90° \leq \beta \leq 180°$ are not symmetric about $\beta = 90°$ due to the different shapes of the front and aft sections of the fuselage. The sharper edge on the aft-side geometry that is experienced when the fuselage is oriented in reverse flow ($90° \leq \beta \leq 180°$) likely causes higher pressure regions that result in increased roll moments for $120° \leq \beta \leq 150°$.

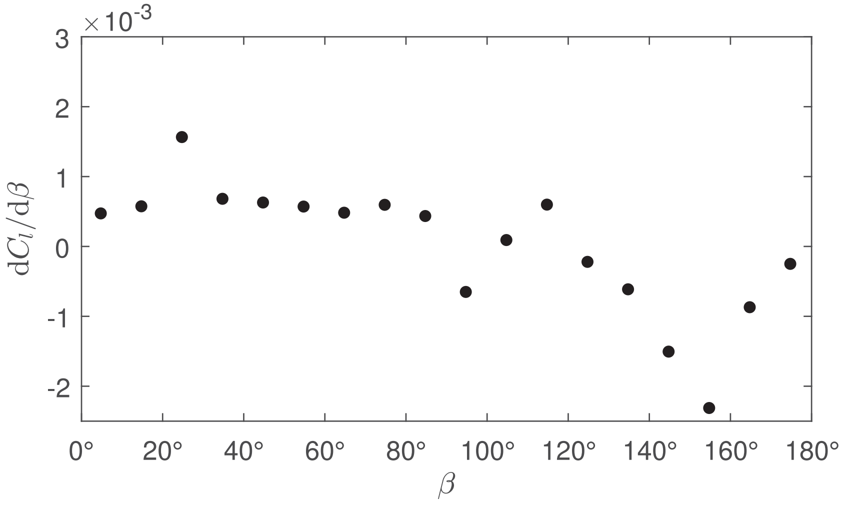

Figure 4.5: Slope of the roll moment coefficients with respect to side-slip angle ($\mathrm{d}C_l/\mathrm{d}\beta$).

The pitch moment coefficients in Figure 4.4b have a slightly lowered magnitude relative to the roll moments, however, larger fluctuations are observed. The pitching moments decrease to the strongest nose-down moment at $\beta = 20°$, before enduring a sudden drop in magnitude between $\beta = 20°$ and 30°. Between $\beta = 30°$ and 60° the pitch moments grow in magnitude, in a similar fashion as the transition from $\beta = 0°$ to 20°, prior to experiencing a rapid shift from a negative value at $\beta = 60°$ to a positive value at $\beta = 70°$. The pitch moments remain at a relatively constant positive magnitude for $70° \leq \beta \leq 100°$ before reducing to near-zero magnitudes for $110° \leq \beta \leq 150°$. The pitch moment experiences a negative jump between 150° and 160° and stays relatively constant for $170° \leq \beta \leq 180°$. Much of the fluctuations can be attributed to the changes in the fuselage wake size and shape as the side-slip angle is varied. The low pressure wake applies forces to the rear surface of the fuselage as well as the bottom of the tail boom, which contributes to the pitching moments. The slope of the pitching moment experiences several large changes, as shown in Figure 4.6. Large positive slopes are experienced, particularly between $\beta = 20°$ and 30°, as well as between $\beta = 60°$ and 70°. The slope does not remain constant at any range for $0° \leq \beta \leq 180°$, which shows the high variablility of the pitch moment with side-slip.

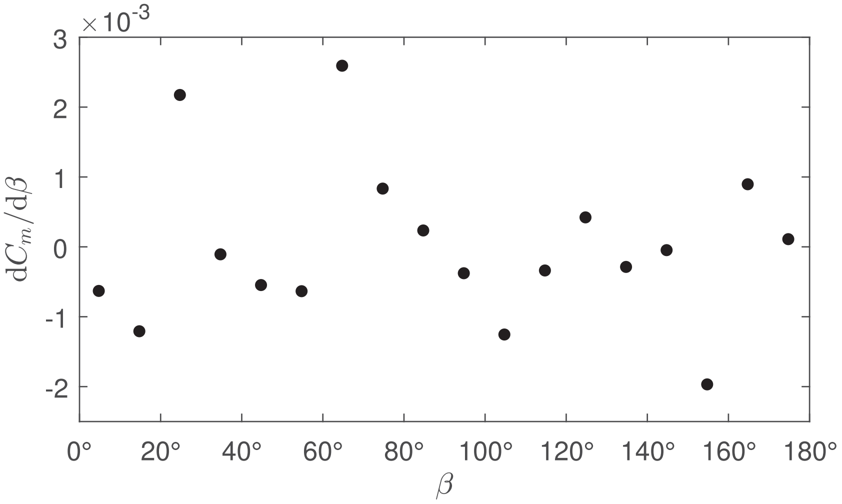

Figure 4.6: Slope of the pitch moment coefficients with respect to side-slip angle ($\mathrm{d}C_m/\mathrm{d}\beta$).

Figure 4.7 shows the pitch and roll moment coefficients on the same axes to display the magnitude and direction of the combined moments acting in the $x'y'$ plane which are relevant to the cyclic pitch control of the main rotor. The combined loading are presented for $0° \leq \beta \leq 90°$ with 10° intervals in Figure 4.7a, and for $90° \leq \beta \leq 180°$ with 10° intervals in Figure 4.7b. It can be seen that both the pitch and roll moments have significant contributions, in contrast to the forward flight condition, shown in Figure 4.3, where the pitching moment was the only main contributor. In Figure 4.7a, the magnitude of the combined moment increases from $\beta = 0°$ to 20°, primarily due to the large increase in the magnitude of the pitching moment. The loading undergoes a large directional shift during the transition from $\beta = 20°$ to 30° resulting from the reduction of the pitch moment and increase of the roll moment magnitude. After the sudden directional change, the loading continues to increase in magnitude from $\beta = 30°$ to 60° as magnitudes of both the pitch and roll moments undergo a similar increase. The pitch moment once again experiences a large shift from $\beta = 60°$ to $70°$, causing another large change in the direction of the combined moment. Both the pitch and roll moments increase positively from $\beta = 60°$ to $90°$, where the maximum combined moment is achieved. These large shifts in the magnitude and direction of the resultant pitch and roll moment vector ($\mathrm{d}C_m/\mathrm{d}\beta$) provide insight to the required action that must be taken to correct for sudden changes in side-slip angle.

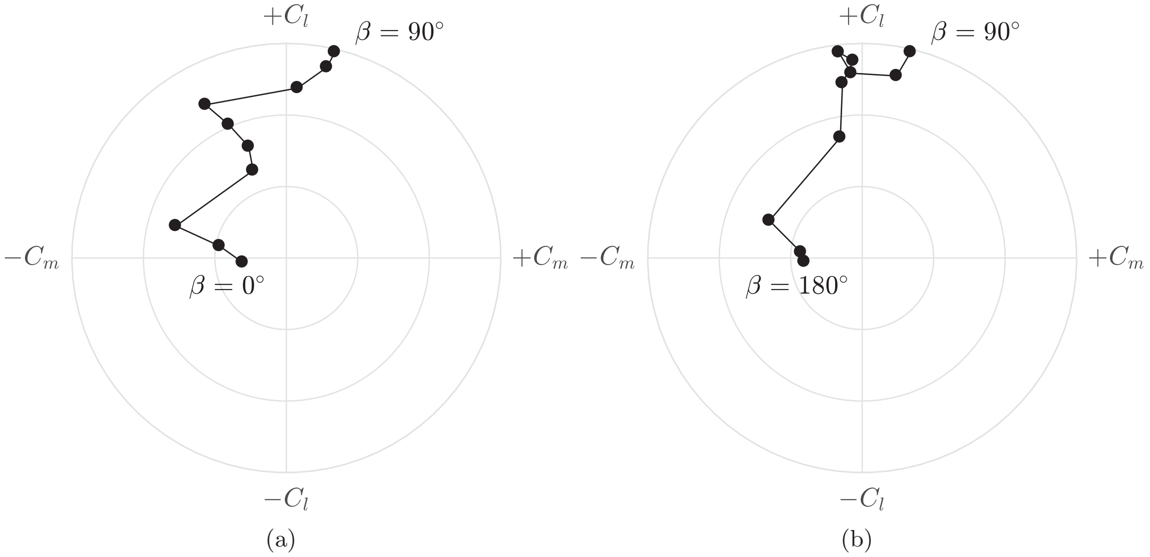

Figure 4.7: Combined pitch and roll moment coefficients showing the changes in magnitude and angle of the moments acting in the $x'y'$ plane. The level flight conditions are shown for (a) $0° \leq \beta \leq 90°$ and (b) $90° \leq \beta \leq 180°$ with 10° increments at zero angle-of-attack.

The combined moments for $90° \leq \beta \leq 180°$ were plotted separately in Figure 4.7b to more easily distinguish the data points, as the values follow a similar path as in $0° \leq \beta \leq 90°$. The main distinction between Figures 4.7a and 4.7b is that the loading remains relatively constant for $90° \leq \beta \leq 140°$ and does not experience any drastic changes in direction or magnitude. Significant changes in direction and magnitude occur between $\beta = 140°$ and $170°$. A large reduction in the roll moment occurs from $\beta = 140°$ to $150°$, followed by large reduction in both the pitch and roll moments from $\beta = 150°$ and $160°$. The reduction in both the pitch and roll moments cause the largest change in direction of the moments over the entire range of side-slip angles. The magnitude again reduces between $\beta = 160°$ and $170°$ before settling at a constant loading for $\beta = 170°$ to $180°$.

Figure 4.8 shows a flight envelope for the level flight condition showing the magnitude of the resultant roll and pitch moment vector ($|C_{lm}|$) for varying side-slip angle. It can be seen that the introduction of small side-slip angles introduces large C_{lm} values. The magnitude of the coefficients are at their largest for $50° \leq \beta \leq 140°$, showing that there is a high aerodynamic loading on the fuselage in this range of side-slip.

Variation of side-slip angle proved to introduce larger forces and moments on the helicopter fuselage, and thus has a more significant impact on the aerodynamic performance.

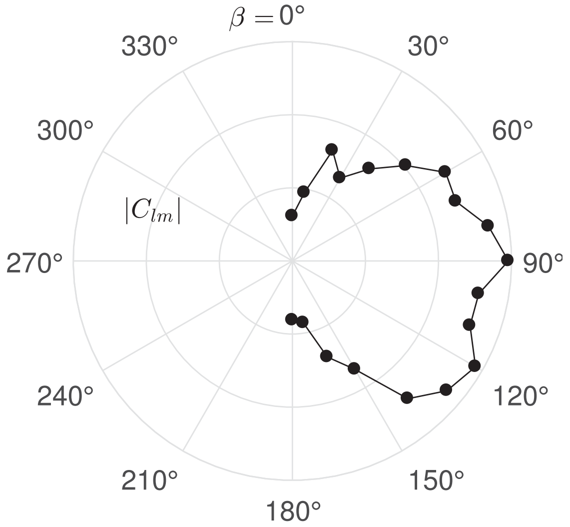

Figure 4.8: Flight envelope for the level flight condition showing the magnitude of the resultant roll and pitch moment vector ($|C_{lm}|$) for side-slip angles varying between $\beta = 0°$ and 180° in 100° increments.

Overall, the moments acting in the $x'y'$ plane have a larger change in magnitude and direction for varying side-slip angle compared to varying angle-of-attack, even over small ranges of angles. The flight conditions in the range of $0° \leq \beta \leq 70°$ show both large changes in the direction and magnitude of the moments relevant to the cyclic pitch control of hte main rotor, which can be problematic for safe flight operation. A particular interest was taken for $0° \leq \beta \leq 40°$ since these side-slip angles are common to forward flight conditions with strong crosswinds.

4.2 Wake Analysis for Varying Angle-of-attack

The planar and stereo-PIV investigation was performed to analyze the development of the rear fuselage wake as described in Chapter 3.4.1. A horizontally oriented FOV in the xy plane in the was analyzed using stereo-PIV techniques. An intersecting FOV in the xz plane was analyzed using two sets of 2-camera planar PIV measurements. The resulting field of view locations can be seen in Figure 3.8. The measurements were performed for $\alpha = \pm 5°$ and $\alpha = 0°$ at zero side-slip, for both the rotor equipped model and the isolated fuselage with no rotor downwash. The rotor equipped model produced a downwash of approximately 18% of the freestream velocity.

Figure 4.9-4.11 shows normalized velocity magnitudes for the the planar and stereo PIV measurement campaign. The isolated fuselage model and the rotor equipped model are compared at $\alpha =$ -5° in Figure 4.9, at $\alpha = 0°$ in Figure 4.10, and at $\alpha = 5°$ in Figure 4.11. It can be seen, particularly in Figures 4.10 and 4.11, that large portions of the xy plane were cut off due to laser sheet blockage from the motor geometry protruding into the FOV. In Figure 4.11, it be seen that the yz plane also experiences laser sheet blockage. A consequence of having a fixed PIV measurement region was that the adjustments of the helicopter angle-of-attack resulted in varying degrees of laser sheet blockage from the aft-body of the fuselage. The pivot location for the helicopter when adjusting the angle-of-attack was located on the rotary table, which was located under the wind tunnel. The extension of the support shaft caused large $x-$direction displacements when the angle-of-attack was adjusted.

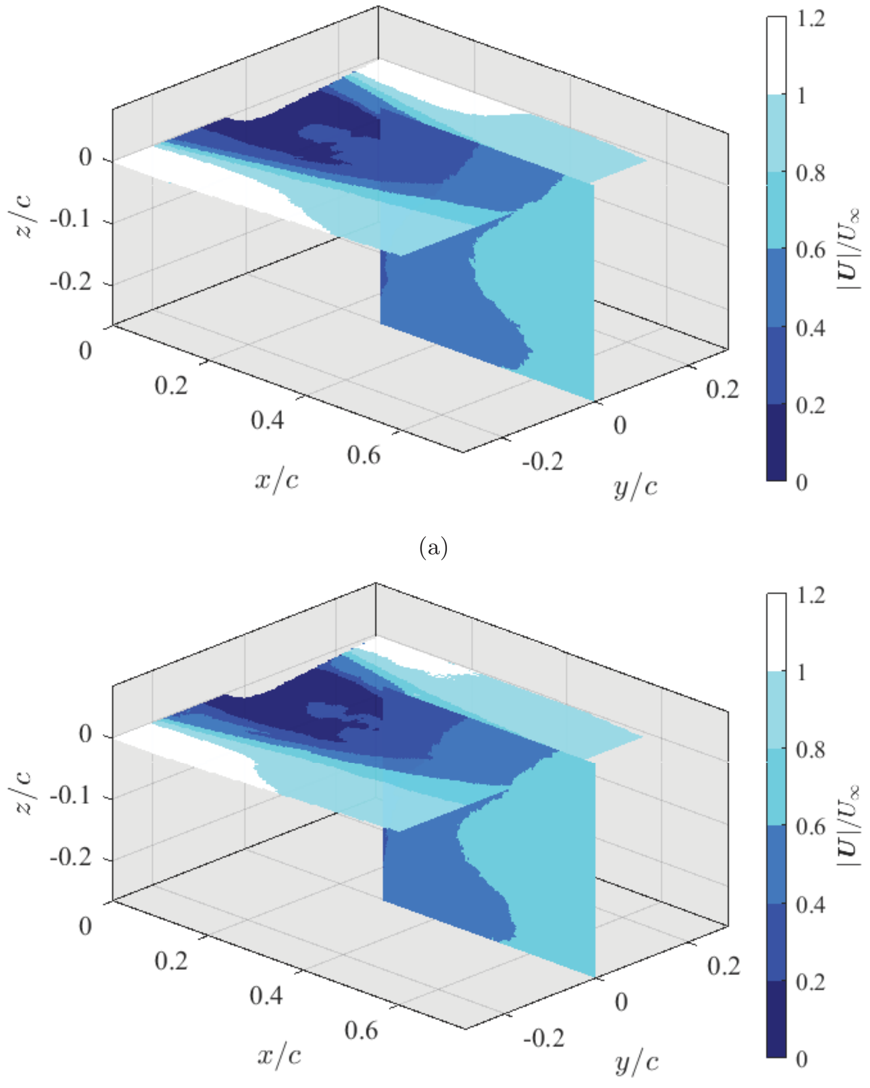

(a)

(b)

Figure 4.9: Normalized velocity magnitudes in the intersecting xy and xz planes comparing (a) the isolated fuselage and (b) the rotor equipped model at α = -5°.

It can be observed in Figure 4.9a that a large low velocity region develops in the near wake of the fuselage. The low velocity regions reduce in width as the flow travels farther downstream, as noticed in the $|\boldsymbol{U}|/U_\infty = 0$ to 0.8 contours of the xy plane. A region of decelerated velocity ($|\boldsymbol{U}|/U_\infty = 0.8$ to 1.0) expands at $x/c \approx 0.2$. The low velocities extends down in the negative $z-$direction. The $|\boldsymbol{U}|/U_\infty = 0.4$ to 0.6 contour of the yz plane exhibits a curvature which causes a peak in the contour at $(x, z)/c \approx$ (0.6,-0.2). The rotor equipped model in Figure 4.9b shows a similar overall pattern to the flow in the presented domain. The presence of the rotor downwash slightly widens the wake in the xy plane relative to Figure 4.9a. A widening of the wake would result in an increased pressure drag. The load measurements by Reß *et al.* (2015) noted a nearly 100% increase in drag for -10° $\leq \beta \leq$ 10° due to the rotor downwash. Since widening of the wake in this investigation is very small, the anticipated effect on the aerodynamic forces is minute. The average velocity of the xz plane in Figure 4.9b is 4% higher than that of the isolated fuselage in Figure 4.9a. This would be expected since the downwash introduces an additional $z-$component of velocity into the near body wake.

Figure 4.10a shows the velocity fields for the isolated fuselage model at $\alpha = 0°$. The geometry of the simplified motor protrudes into the field of view of the horizontally oriented (xy) stereo-PIV measurement plane. The laser sheet blockage resulted in an obstructed domain for $0 \leq x/c \leq 0.2$ and -0.05 $\leq y/c \leq$ 0.30. It can be seen that the magnitudes of velocity in the PIV measurement regions are much lower than the magnitudes at $\alpha =$ -5°. The measurement region has a closer proximity to the fuselage at $\alpha = 0°$, and thus the magnitude of the velocity fields are expected to be reduced. The bulk of the velocity magnitudes in the measurement region are less than 40% of the freestream velocity U_∞. The addition of the rotor downwash in Figure 4.10b slightly widens the wake in the xy plane when compared to the isolated fuselage model in Figure 4.10a, similar to the feature observed in Figure 4.9. A more notable increase in the velocity magnitude of 11% is noticed in the xz plane of rotor equipped model at $\alpha = 0°$.

The velocity fields in the wake of the isolated fuselage at $\alpha = 5°$ are shown in Figure 4.11a. A large portion of the stereo-PIV (xy) and a small portion of the planar PIV region (xz) were lost due to laser sheet blockage. Particle illumination was lost for up to $x/c = 0.35$ in the xy plane. The majority of the flow in the xz plane has a magnitude of $|\boldsymbol{U}|/U_\infty = 0.4$ or less. The entirety of the xz plane has velocity magnitudes less than 40% of the freestream velocity U_∞. A region of locally increased velocity, as indicated by the $|\boldsymbol{U}|/U_\infty =$ 0.2-0.4 contour, develops in the top section of the xz plane ($z/c \approx$ 0-0.1 and $x/c \approx$ 0.4-0.5). This increased velocity region corresponds to circulating flow that detaches from the side of the fuselage. The rotor equipped model at $\alpha = 5°$ shows similar performance when compared to the isolated fuselage model. The velocity field for the rotor equipped model shown in Figure 4.11b show some minor distinctions from the isolated fuselage wake. The circulating flow region that was observed in Figure 4.11a was found to reduce in size for the rotor equipped model. The average velocity magnitude in the xz plane is 10% greater for the rotor equipped model when compared to the isolated fuselage with no downwash.

Overall, the presence of the main rotor downwash was found to consistently cause a small increase in the width of the wake as the flow travels downstream. The additional downwards component of velocity that is characteristic of a helicopter's main rotor was found to increase the velocity in the wake region by approximately 10%. Ultimately the effect of the main rotor was found to be minimal and did not vary significantly with changing angle-of-attack. This can be partially attributed to the blockage of the downwash by the tail boom geometry of the helicopter, as well as the ratio low ratio of the downwash to the freestream velocity.

4.3 Conclusions

An investigation into the aerodynamic characteristics of a helicopter fuselage was performed both for a rotor equipped model, and an isolated fuselage with no spinning rotor. Six-axis load cell measurements were performed over a wide array of flight conditions were performed to analyze the effect and significance of the angle-of-attack and side-slip angle. A planar and stereo-PIV campaign was performed in the wake of the fuselage to investigate the development of the separation bubble under conditions including and not including the main rotor downwash.

The forward flight condition was analyzed at $\beta = 0°$ while varying the angle-of-attack over the range -15° $\leq \alpha \leq$ 15° in 2.5° increments. It was found that the angle-of-attack had notable effects on the drag, lift, and pitch moment coefficients. The drag was found to decrease with increasing angle-of-attack, while the lift was found to increase linearly. The pitch moments were found to increase as the angle-of-attack was swept from negative to positive, and a negative (nose down) pitch moment was present at $\alpha = 0°$. The roll and yaw moment did not show any significant variance for changing angle-of-attack. The trends noticed in the presented data were found to be similar to those discussed in literature.

The level flight condition was examined at $\alpha = 0°$ while varying the side-slip angle from $\beta = 0°$ to 180° in 10° increments. The side-slip angle was found to have a more significant effect on the aerodynamic loads in comparison to the angle-of-attack. The drag and side force coefficients noticed large variations with changing side-slip, having values that were nearly an order of magnitude larger that those for varying angle-of-attack. The lift force coefficients had little variation relative the the other aerodynamics forces, and only had small fluctuations around zero magnitude. The yaw moment coefficients experienced the largest changes in magnitude out of the aerodynamic moments acting on the fuselage. The pitch and roll moment exhibited a similar magnitude range, though the pitch moments underwent larger variations over the 10° increments. The combined loading of the pitch and roll moments that are relevant to the main rotor cyclic controls showed large variations in both magnitude and direction. The large variations seen as a feature of the aerodynamic performance that may be problematic to the safe operation of the helicopter in forward flight and hover conditions.

A planar and stereo-PIV investigation as performed in the wake of the fuselage for a side-slip of $\beta = 0°$ and angles-of-attack of α = -5°, 0°, and 5°. A large separation bubble with low velocity magnitudes was found to develop in the rear fuselage wake. The wake extended and widened downstream of the fuselage. The main rotor downwash was found to consistently cause a slight widening of the wake. The downwash of the main rotor was also found to increase the magnitude of the velocity in the separation bubble by approximately 10%. Overall, the effect of the main rotor downwash was found to be minute.

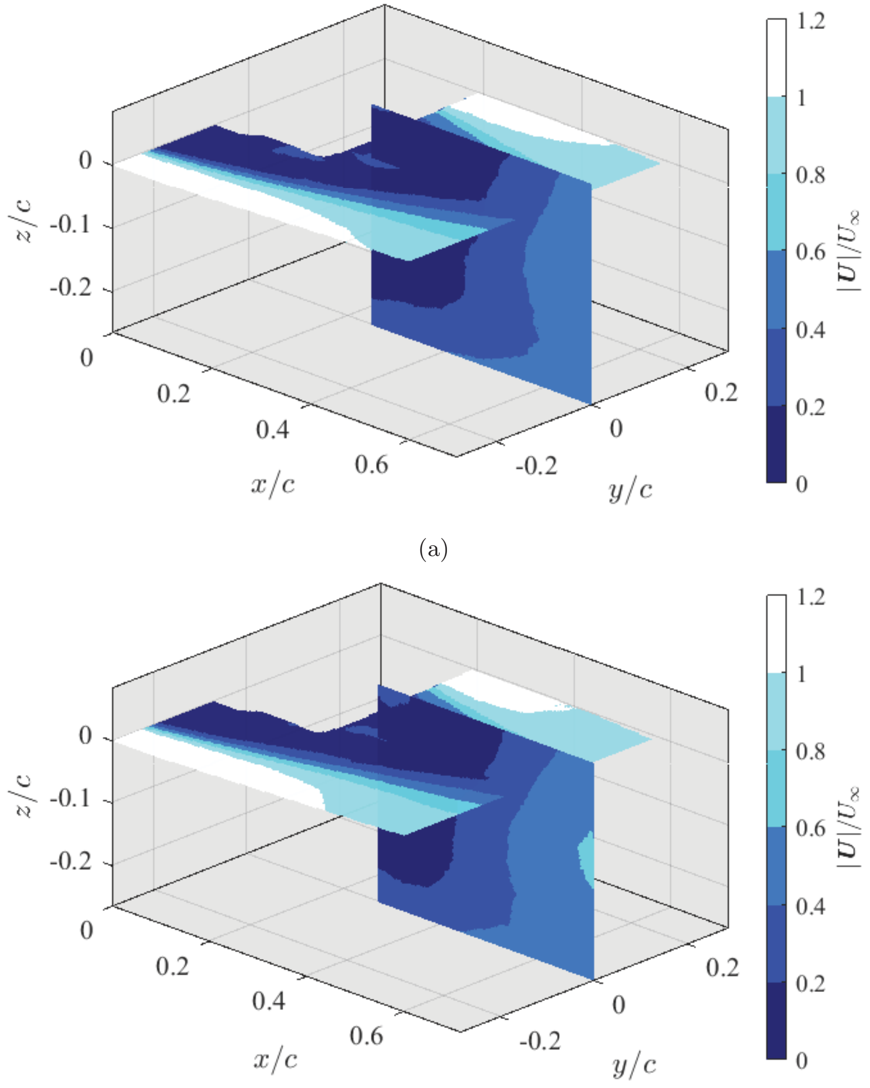

(a)

(b)

Figure 4.10: Normalized velocity magnitudes in the intersecting xy and xz planes comparing (a) the isolated fuselage and (b) the rotor equipped model at $\alpha = 0°$.

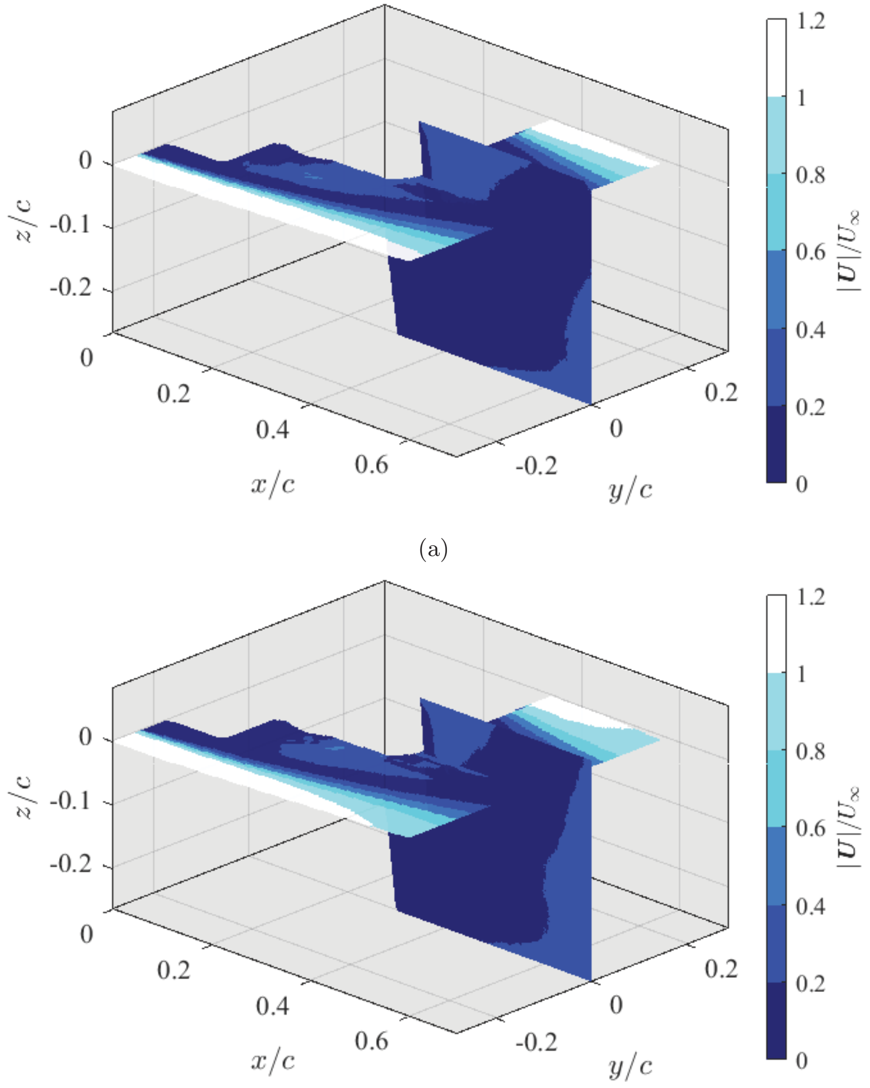

(a)

(b)

Figure 4.11: Normalized velocity magnitudes in the intersecting xy and xz planes comparing (a) the isolated fuselage and (b) the rotor equipped model at $\alpha = 5°$.

Chapter 5

Analysis of Side-Slip Angle and Rear-Fuselage Geometry on Wake Flow

This chapter covers the investigation performed to analyze the effect of side-slip angle on the aerodynamic performance of the fuselage using four different rear-fuselage configurations. A removable motor geometry, as well as a streamlined and round enclosure for the motor were developed to investigate the effect of the rear-fuselage geometry at various side-slip angles. Six-axis load measurements were performed over a narrower range of side-slip to provide a more detailed comparison of the parameters. A four camera planar PIV campaign was carried out to analyze the fuselage wake formation over a range of side-slip angles. Instantaneous vorticity and mean velocity fields were analyzed to evaluate the effectiveness of the rear-fuselage configurations.

5.1 Load Measurements

The dimensionless aerodynamic drag coefficients for the four tested configurations are shown for side-slip angles $0^\circ \leq \beta \leq 40^\circ$ in Figure 5.1a. The drag data for a twin engine light ANSAT helicopter model at $Re = 3.85 \times 10^6$ by Stepanov *et al.* (2016) was digitized and plotted alogn with the drag coefficients in Figure 5.1a. Since the coefficients presented in Stepanov *et al.* (2016) were multiplied by an undisclosed constant, the values in Figure 5.1a were scaled to procide a relative comparison of the trend with respect to the baseline data. The overall trend of the drag coefficients for all configurations follows a parabolic increase with increasing side-slip. The trend for baseline configuration can be described by the second-order polynomial $C_D = 0.0007\beta^2 + 0.0003\beta + 0.2575$, where β is in degrees. The drag coefficients for the empty configuration show minimal difference from the baseline configuration (<5%) for the range of tested side-slip angles. The cusped and round cases display more significant variations from the baseline model. The cusped case notices a drag reduction up to 20% at low side-slip while showing small variation (<5%) for $20^\circ \leq \beta \leq 35^\circ$.

The round case shows a consistent increase in drag (up to 20%) for the full range of side-slip, however a gradual regression to the baseline is observed after $\beta = 30°$. The cusped case has the highest reduction in drag due to its streamlined profile that is expected to delay the flow separation further downstream of the body at low side-slip angles. This notion is supported by the load measurements for side-slip angles up to 30°. At higher side-slip angles the increase of effective cross-section of the body dominates and drag increases. The round TE case was designed to avoid flow separation from the sharp geometries of the trailing-edge at high side-slip angles and, as a consequence, increases drag at lower side-slip angles.

The lift coefficients shown in Figure 5.1b compare the four configurations for side-slip angles $0° \leq \beta \leq 40°$. It is clearly shown that the magnitudes of the lift coefficients are much lower than the drag coefficients as the maximum values have an order of magnitude of difference. The lift coefficients remain relatively constant and have minute differences between the configurations prior to $\beta = 25°$. After $\beta = 25°$ the four configurations begin to show larger differences. All configurations experience a loss of lift at $\beta = 25°$ with the exception of the cusped case, which experiences a drop in lift after $\beta = 30°$. The loss in lift at high side-slip angles is associated with the displacement of the high-pressure wake region from the area under the tail boom to the side of the aft-body, as will be seen in the PIV results. The flow is expected to remain attached to the cusped case at higher angle and thus the loss of lift is delayed to $\beta = 30°$.

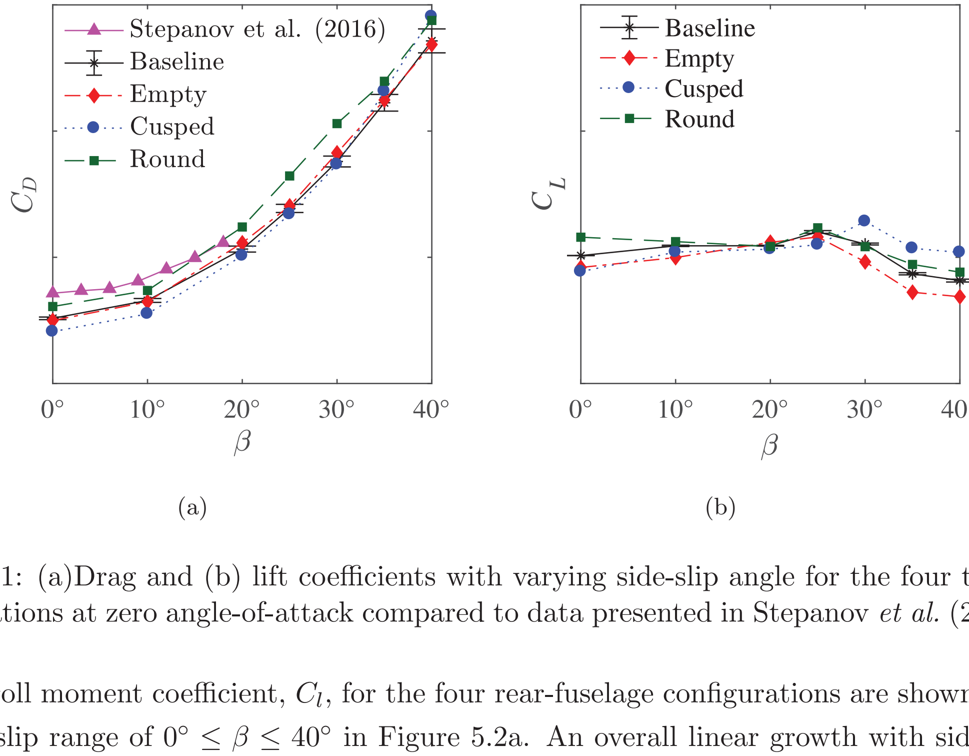

(a)

(b)

Figure 5.1: (a)Drag and (b) lift coefficients with varying side-slip angle for the four tested configurations at zero angle-of-attack compared to data presented in Stepanov *et al.* (2016).

The roll moment coefficient, C_l, for the four rear-fuselage configurations are shown over the side-slip range of $0° \leq \beta \leq 40°$ in Figure 5.2a. An overall linear growth with side-slip angle is evident for all configurations. Sweet and Jenkins Jr. (1962) presented roll moment coefficients for various helicopter fuselage models which showed a linear trend with β for

-8° $\leq \beta \leq$ 8° which supports the trend in Figure 5.2a over a portion of the range. It is observed that the baseline, cusped, and round geometries have a smaller roll moments compared to the empty configuration for side-slip angles up to 25°. At side-slip angles greater than 30°, the roll moment coefficients for the cusped case are notably greater than the other three configurations. This is associated with the effect of the larger lateral cross-section of the cusped configuration at high side-slip angles.

The pitch moment coefficients are shown for the four configurations in Figure 5.2b as a function of the side-slip angle. The magnitude of the pitch moment is negative throughout the presented range of side-slip angle corresponding to a nose down moment. The pitch moment at $\beta = 0°$ varies notably between the configurations. The magnitude of C_m at $\beta = 0°$ for the configurations follows a reverse pattern of the drag force coefficients, mainly that the cusped case has the largest magnitude while the round case has the smallest. The values of C_m decrease to larger negative values up to an angle of $\beta = 20°$ (i.e., $\mathrm{d}C_m/\mathrm{d}\beta < 0$) where each configuration experiences its maximum nose down pitching moment. The comparison of the baseline and the empty configuration shows that the presence of the motor geometry in the baseline configuration results in a large negative C_m within $10° \leq \beta \leq 35°$ compared to the empty configuration. The cusped case however, has a near-zero slope ($\mathrm{d}C_m/\mathrm{d}\beta$) within $0° \leq \beta \leq 20°$, and the round case also has a reduced slope relative to the baseline and empty configurations over this range of side-slip. The experimentally and numerically determined pitch moments presented in Brunello *et al.* (2012) have small negative slope up to an angle of $\beta = 15°$ before transitioning to a larger positive slope for $\beta > 15°$, as shown in Figure 5.2b. The pitching moments in Figure 5.2b follow a similar trend with the transition from negative slope to positive slope occurring at $\beta = 20°$. The baseline and empty configurations exhibit a sharp $\mathrm{d}C_m/\mathrm{d}\beta$ transition at $\beta = 20°$ which can be problematic in flight conditions where cross-winds cause rapid changes in side-slip angle. The cusped and round cases, however, there is a less extreme $\mathrm{d}C_m/\mathrm{d}\beta$ transition at $\beta = 20°$. In the range of $20° \leq \beta \leq 30°$, the baseline and empty configurations experience a rapid drop in magnitude associated with the high positive slope during that range of side-slip. The cusped case has a similar slope to the baseline and empty configurations from $\beta = 20°$ to 25°, but has a significantly reduced from $\beta = 25°$ to 30°. The change in magnitude from $\beta = 20°$ to 30° that is experienced by the cusped case was reduced by 36% relative to the baseline configuration. The round case maintains a relatively constant C_m with comparatively lower magnitudes for side-slip $\beta > 20°$. The reduction in magnitude between $\beta = 20°$ and 30° was reduced by 67% compared to the baseline configuration in the same range.

The drag and lateral-longitudinal stability of the fuselage were investigated to characterize the aerodynamics of the helicopter at side-slip angles. When analyzing the drag performance, the cusped case has the most desirable performance since it consistently had the lowest drag coefficients at lower side-slip angles. The round case provided a much larger

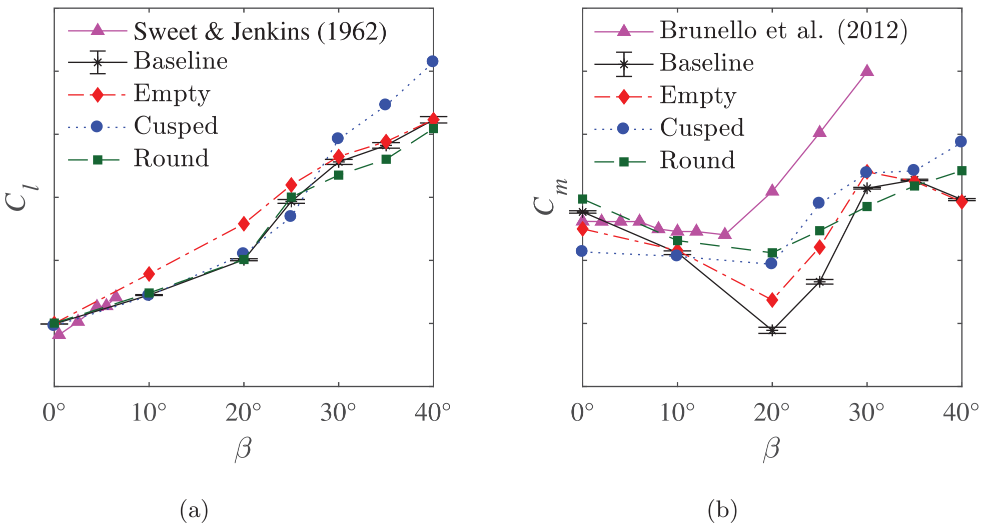

(a) (b)

Figure 5.2: Dimensionless (a) roll and (b) pitch moment coefficients for varying side-slip angle comparing the four fuselage configurations at zero angle-of-attack.

drag than the other configurations for the entire range of presented side-slip angles due to its blunt trailing-edge profile and larger lateral cross-section. When analyzing the stability of the roll and pitch moments, the baseline and empty configurations experienced sharp transitions in moments at $\beta = 20°$. The cusped case provided the superior performance with regards to stability, especially considering smooth variations of the pitch moment across the full range of side-slip angles. Further analysis of the load cell measurements would require a better understanding of the flow around the fuselage. Since the fuselage is a bluff body, the aft-body flow is of particular interest with regards to its aerodynamic performance. The planar PIV measurements are used in the next section to characterize the wake formation in the aft-body.

5.2 Four-Camera Planar PIV Investigation

The four-camera planar PIV investigation was performed to analyze the wake for a side-slip angle range of $0° \leq \beta \leq 40°$. The four fuselage rear-fuselage designs were tested at zero angle of incidence for both the isolated fuselage and the rotor equipped model to analyze the effect of the main rotor downwash. The experiment was configured as described in section 3.4.2.

5.2.1 Forward Flight Condition

The forward flight condition with no side-slip angle is used to analyze the wake development behind different geometries and to determine the effect of the main rotor downwash. Figure 5.3 compares the instantaneous vorticity component about the z-axis at zero side-slip angle for the four fuselage configurations. The black area of the PIV results represents the cross-section of the fuselage and appendages at the measurement plane. The gray area represents locations where no vectors were computed due to laser sheet blockage or obstruction of the FOV from the lower appendages as seen in Figure 3.9. The wake flow of all configurations is mainly comprised of small-scale vortical structures fed into the wake by the two shear layers. The small-scale structures are indicative of a highly turbulent flow at $Re_w = 4.5 \times 10^5$, base on the trailing-edge width of the model. The vortices on each side of the fuselage are counter-rotating while they tangle around the wake centerline. Figure 5.3 shows that the baseline and empty configurations have a stronger separated shear layer and a wider wake than the cusped and round cases. This results from the fixed separation point at the sharp corner of the fuselage in the baseline and empty configurations. The wake in Figure 5.3c shows that the boundary layer follows the initial part of the cusped geometry before separation. In this case, a weaker shear layer and a narrower wake are formed. The corner of the round geometry in Figure 5.3d has a small radius and does not prevent eearly separation of the shear layer.

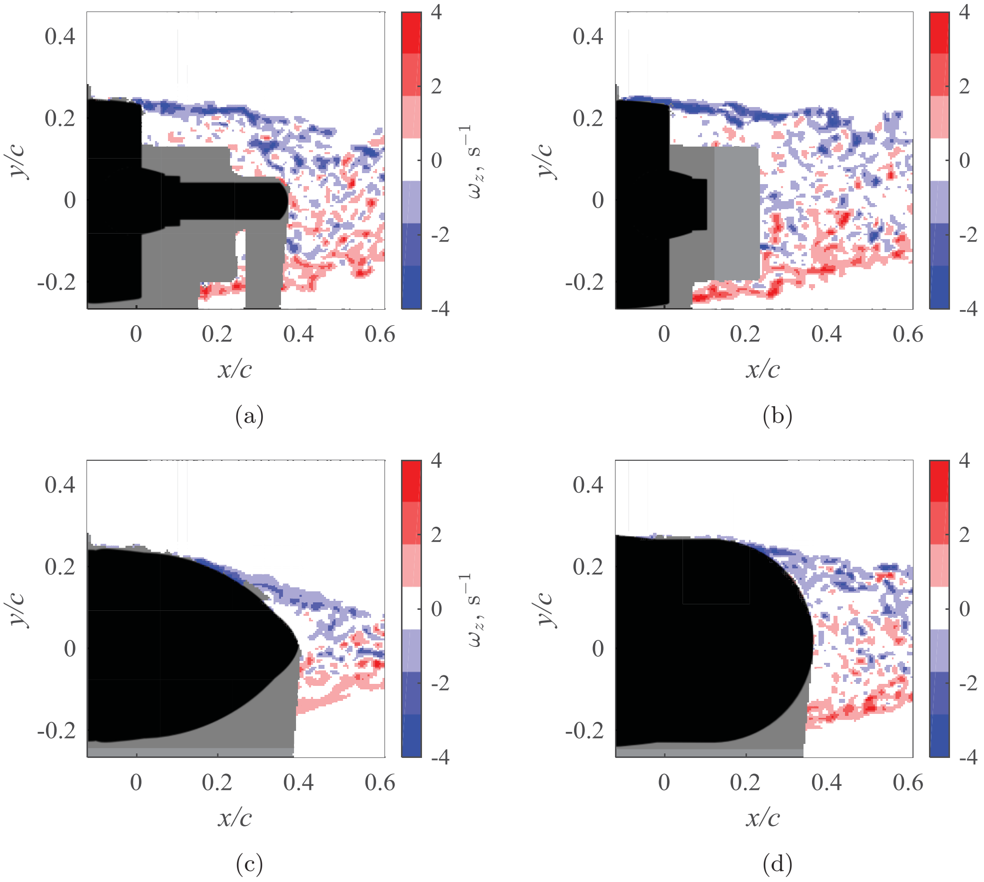

Figure 5.3: Instantaneous vorticity field at zero angle of incidence comparing the (a) baseline, (b) empty, (c) cusped, and (d) round case configurations.

5.2.2 Effect of Main Rotor Downwash

The effect and significance of the main rotor downwash on the wake flow is investigated at rotor downwash velocity to freestream velocity ratio of $U_d/U_\infty = 0.18$. The normalized magnitude of mean velocity ($|\boldsymbol{U}|/U_\infty$) in the wake of the fuselage are shown without the rotor (isolated fuselage) in Figures 5.4(a-d), and with the rotor equipped in Figures 5.5(e-h). The symmetry of the wake flow for the isolated fuselage in Figure 5.4(a-d) allowed for the resulting vector fields to be mirrored about the y-axis to reduce the regions of lost data due to laser sheet blockage. The separation bubble is visible in Figure 5.4 as the low velocity region (i.e., separation bubble) while the freestream has accelerated slightly beyond U_∞ ($1 < |\boldsymbol{U}|/U_\infty < 1.2$) outside this region. The bulk of the flow following the aft-face of the fuselage contains velocity magnitudes less than 20%. The flow separation from the fuselage is at the sharp corner of the body in the baseline and empty configurations, as specified in Figures 5.4a and 5.4b. The flow separation for the cusped case in Figure 5.4c occurs farther downstream as a combined result of an adverse pressure gradient induced by the surface curvature. This type of flow separation is not bounded to a fixed point and can move along the surface of the cusped TE. A large separation bubble is also observed in the PIV results presented by Breitsamter *et al.* (2014) in the wake of the helicopter model. For each of the isolated fuselage configurations, the wake begins to slightly expand around $x/c = 0.5$ as shown by the ($|\boldsymbol{U}|/U_\infty = 0.8$ to 1.0 contour.

The presence of the rotor downwash in Figures 5.4(e-h) slightly widens the wake, which can increase the pressure drag. The load measurements in Reß *et al.* (2015) displayed a consistent 50-100% increase in drag for $-10° \leq \beta \leq 10°$ resulting form the rotor downwash. The swirl of the rotor downwash also causes the wake to be slightly asymmetric, particularly with the cusped case in Figure 5.4g where the separation is not fixed at a geometric edge. The wake skews towards the side of the retreating blade in the positive y-direction. The asymmetries are indicative of an additional cross-flow component to the velocity, similar to the results of De Gregorio *et al.* (2012) that showed an increased cross-flow component and decreased axial velocity that was attributed to an increase of the fuselage drag. However, the magnitude of the mean cross-flow component on the centerline of the wake is about 0 to 2% of the freestream velocity.

The RMS of the magnitude of the velocity vector for the isolated fuselage and the rotor equipped model are shown at zero angle of incidence in Fig. 9. Figures 9a and 9b show that the shear layer region immediately following the back edge of the fuselage has large velocity fluctuations. The cusped case for the isolated fuselage in Fig. 9c has a small and focused region with larger RMS of velocity along the centerline of the wake. A consistent feature that can be noticed when comparing the isolated fuselage configurations in Figure 5.5(a-d) with the rotor equipped models in 5.5(e-h) is the asymmetry about the longitudinal axis of the fuselage (x'-axis) that resulted from the counter-clockwise swirl of the rotor downwash. Similar to the mean velocity in Figure 5.4, the fluctuation contours are skewed towards the retreating blade side of the fuselage in the positive y-direction. The asymmetry is small for all the configurations except for the cusped aft-body. The difference is associated with the transient behavior of the separation point on the relatively mild curvature of the cusped geometry. The other three configurations experienced a fixed separation points as a result of the sharp edges or strong curvature.

Ultimately the significance of the few features resulting from the main rotor downwash was deemed minute when comparing the aft-body configurations. The effect of downwash would likely remain small relative to the large effect of the side-slip angle on the wake flow. The remaining analysis was performed on the isolated fuselage to study the effect of the rear-fuselage geometry and side-slip angle.

5.2.3 Effect of Side-Slip Angle

The planar PIV was performed in the wake region of the four rear-fuselage configurations for side-slip angles ranging from $\beta = 10^\circ$ to 40°. The normalized mean velocity magnitude and RMS fluctuation field are presented for $\beta = 10^\circ$ in Figure 5.6, for $\beta = 20^\circ$ in Figure 5.7, for $\beta = 30^\circ$ in Figure 5.8, and for $\beta = 40^\circ$ in Figure 5.9. Figures 5.6-5.9 are organized such that the normalized velocity magnitudes are in subfigures (a-d) while the RMS fluctuations are in subfigures (e-f). The velocity magnitudes and the RMS velocities were calculated, and normalized by the freestream velocity, U_∞.

It is noticed in Figure 5.6 that the mean velocity field is skewed slightly in the positive y-direction with respect to the centerline of the fuselage (x'-axis). The length of the wake extending from the back of the fuselage in Figure 5.6(a-d) do not show any substantial change in size when compared with $\beta = 0^\circ$ wake in Figure 5.4(a-d). Figure 5.6(a-b) show that the baseline and empty configurations have similar mean velocity fields. The cusped case in Figure 5.6c has the narrowest wake which corresponds with the lowest drag at $\beta = 10^\circ$, as observed in the load measurements in Figure 5.1a. The wake region of the round configuration has similar dimensions relative to the baseline configuration. Figure 5.6(c-d) show that the cusped and round cases begin to exhibit small areas of accelerated flow (1.2-1.4 U_∞) along the side of the body.

The RMS of the velocity fields in Figures 5.6(e-h) show a more pronounced asymmetry in the flow with respect to the x'-axis, particularly in the empty and round configurations as seen in Figure 5.6f and 5.6h. The asymmetry is smaller in the baseline configuration due to protrusion of the motor section in the wake, which reduces early interaction of the two shear layers. Fluctuations stemming from each side of the fuselage merge downstream in a V-shaped pattern for the baseline configuration in Figure 5.6e. In the wake of the cusped configuration, the turbulence fluctuations are more intense while covering a smaller region.

As the side-slip angle is increased to $\beta = 20^\circ$ in Figure 5.7, more changes in the mean velocity and RMS fields are noticed. Though the bulk of the low velocity regions in Figures 5.7(a-d) remain on the positive y side of the body, the freestream begins to curve the tail of the separation bubble towards the negative y-direction. The length of the separation bubble noticeably decreases from $\beta = 10°$ to $20°$. When comparing the shape of the wake for the baseline configuration at $\beta = 10°$ and $\beta = 20°$ in Figures 5.6a and 5.7a, it can be observed that the $|\boldsymbol{U}|/U_\infty = 0$ to 0.2 contour sits much closer to the motor geometry at $\beta = 20°$. The mean velocity field in Figure 5.7b show the development of a localized region of larger velocity (0.4-0.6 U_∞) inside the separation bubble of the empty configuration, which can be attributed to recirculation in the flow. Figures 5.7(c-d) show a small high-speed flow region at the upper section of the cusped and round cases relative to $\beta = 20°$.

The RMS fluctuation fields in Figures 5.7(e-h) are concentrated in a narrower region compared to those in 5.6(e-h). The baseline and empty configurations in Figures 5.7(e-f) both show a similar RMS field with the bulk of the fluctuations rooting from the upturned side of the fuselage. The stronger fluctuations in the wake of the cusped case shown in Figure 5.7g root more from the downturned side of the fuselage, and a region of low velocity fluctuations on the same side widens near the separation point.

Figure 5.8 compares the flow field of the four configurations at a side-slip angle of $\beta = 30°$. The transition between side-slip angles of 20° and 30° provided the largest discrepancy between the configurations in the load measurements of Figures 5.1 and 5.2. The sign of $\mathrm{d}C_m/\mathrm{d}\beta$ also changed from negative to positive at $\beta = 20°$. The mean flow fields in Figures 5.8(a-d) show a notable reduction in the length of the wake with respect to the previous side-slip angles. The wake of the baseline configuration in Figure 5.8a maintains a similar curvature as at $\beta = 20°$ in Figure 5.7a, and the $|\boldsymbol{U}|/U_\infty = 0$ to 0.2 contour remains tight to the motor geometry.

Additional growth of the recirculation region is seen for the empty configuration in Figure 5.8b. The low velocity bubble for the cusped case in Figure 5.8c undergoes a large reduction in size and the separation bubble is more concentrated in a smaller region. Figures 5.8c-d show that both the cusped and round cases also experience a change in the curvature of the wake that was first noticed by the baseline and empty configurations at $\beta = 20°$ in Figures 5.7a-b. The high-speed region also becomes larger in the cusped and round cases at a side-slip angle of 30°.

The RMS fluctuation fields in Figures 5.8(e-h) notice a more significant change in comparison to the previous angles. The overall width and strength of the region with high velocity RMS for each configuration increases drastically. Figure 5.8e shows that there is a single region with high RMS of velocity at the immediate downstream of the motor. This region is formed where the two shear layers interact, and is in contrary to the V-shape pattern of the high RMS region formed by the two shear layers in Figure 5.6a. There is also the possibility of interaction of the separated shear layer from the upper edge of the fuselage with the motor protrusion in Figure 5.8e, which can result in structural vibration of the fuselage. The widening of the high RMS region of the baseline configuration was observed to occur at $x/c = 0.4$ in Figure 5.7e, while it has shifted farther upstream to a location of

$x/c = 0.2$ in Figure 5.8e. A similar pattern was noticed for the empty configuration as the location where the fluctuation region widened (at 0.1 U_∞) shifted from $x/c = 0.5$ in Figure 5.7f to $x/c = 0.25$ in Figure 5.8f. The cusped and round cases no longer experience the widening of the wake from a downstream location. Rather, the region of 0.1 U_∞ expands sharply from the downturned side of the body at $x/c = 0.25$, as shown in Figures 5.8(g-h). The round case produces a large region of high fluctuations, as seen in Figure 5.8h. The large region of unsteady flow indicates a low pressure wake region, which further supports the large drag discrepancy between the round case and the other configurations noticed in Figure 5.1a.

The mean velocity and RMS fields comparing the four configurations at $\beta = 40°$ are shown in Figure 5.9. The high side-slip angle causes the flow to accelerate around the sides of the fuselage prior to the flow separation. In all configurations a larger and stringer accelerated flow region (1.2-1.4 U_∞) is observed on both sides of the aft-body. The motor geometry of the baseline configuration clearly protrudes and interferes with the shear-layer separated from the blunt fuselage edge, as shown in Figure 5.9a. The local region with higher velocity inside the separation bubble of the empty configuration reduces in size and shifts towards the negative y side of the fuselage, as shown in Figure 5.9b. The separation from the upper side of the cusped configuration occurs at the downstream end of the geometry due to the high side-slip angle in Figure 5.9c. The separation bubble of the cusped case is primarily concentrated within a small region on the -y' side of the fuselage longitudinal axis (x') which would cause a larger component of the pressure distribution from the wake to be projected about the roll axis (x'). The mean wake of the round case in Figure 5.9d slightly widens and has a marginally higher velocity at $\beta = 40°$.

The RMS of velocity in Figures 5.9(e-h) continues to expand in width and becomes more intense relative to the previous angles. The interference of the motor geometry in the baseline configurations triggers the high fluctuation region noticed in Figure 5.9e which would lead to oscillations of the fuselage. The fluctuations in the empty configuration root primarily from the -y side of the fuselage. The separation from the sharp trailing edge of the cusped case triggers a high fluctuation region in the wake, as shown in Figure 5.9g. The width of the region with RMS of 0.1 U_∞ continues to expand from the negative y' side of the fuselage at high side-slip angles. The strength of the fluctuations for the round case persists at $\beta = 40°$, as shown in Figure 5.9h.

One of the main conclusions from the PIV results comparing side-slip angles is that the separation bubble grows in strength as RMS of velocity fluctuations increases with increasing β from 0° to 20°. Therefore, the low pressure region becomes stronger and the negative pitch moment increases. From $\beta = 20°$ to 40°, the separation bubble becomes stronger and concentrates in a smaller region. However, the separation bubble is not aligned with the longitudinal axis of the fuselage and is shifted to the downturned side of the fuselage due to the freestream flow coming around the upturned side of the fuselage. A result of this misalignment is that a component of the moment from the low pressure region is projected about the x'-axis (i.e., roll moment). Therefore, within $20° \leq \beta \leq 40°$ the pitching moment is reduced while the roll moment is increased, explaining the trends discussed in Figure 5.2.

5.3 Conclusions

A wind tunnel investigation was performed to investigate the effect of side-slip angle on the aerodynamics of a helicopter model with different aft-body geometries. Three components of force and moments were measured using a six-axis load cell on four rear fuselage configurations over side-slip angles ranging from $\beta = 0°$ to $40°$. PIV measurements were carried out and compared to the six-axis load cell measurements to provide an in depth analysis of the instantaneous vorticity fields as well as the mean velocity and RMS fluctuations. Planar PIV was also performed on a rotor equipped model to analyze the effect of rotor downwash on the wake flow.

The drag force coefficients displayed a parabolic increase with rising side-slip angle. The cusped case reduced the drag up to 20% for side-slip angles up to $\beta = 30°$, while the round case increased the drag for $0° \leq \beta \leq 40°$. The empty configuration displayed an increased $\mathrm{d}C_l/\mathrm{d}\beta$ slope of the roll moment coefficients up to $\beta = 20°$ while exhibiting similar patterns as the other configurations at higher side-slip. The cusped case had the largest zero angle pitch moment while the cusped case had the smallest magnitude, following an inversed order as the zero angle drag coefficients. The slope of the pitching moment ($\mathrm{d}C_m/\mathrm{d}\beta$) changes sign from negative to positive at $\beta = 20°$. The baseline configuration exhibited a large decrease in pitch moment magnitude between $\beta = 30°$ and $40°$. The cusped case reduced the variation of the pitch moment by 36% relative to the baseline configuration, while the round case reduced the variation by 67%.

The analysis of the vorticity fields at zero angle of incidence from planar PIV showed small-scale structures in shear layer regions of the turbulent wake. The main rotor downwash slightly widened the wake and resulted in a small asymmetry of the wake, most notably in the cusped case configuration. The wake of the cusped case was more sensitive to the rotor downwash since the separation pointed was not fixed at a geometric edge. The effect of the main rotor downwash was considered to be minute relative to the effect of the rear fuselage geometries and the side-slip angle.

The effect off side-slip angle on the wake flow was evaluated using planar PIV measurements on the fuselage wake for $10° \leq \beta \leq 40°$. Increasing β angle from $0°$ to $20°$ was found to increase the strength of the wake, causing the negative pitch moment to increase. As β was increased above $20°$ the wake became more concentrated in a smaller area that was skewed towards the downturned side of the fuselage. This resulted in a larger component of the pressure distribution to be projected about the roll axis.

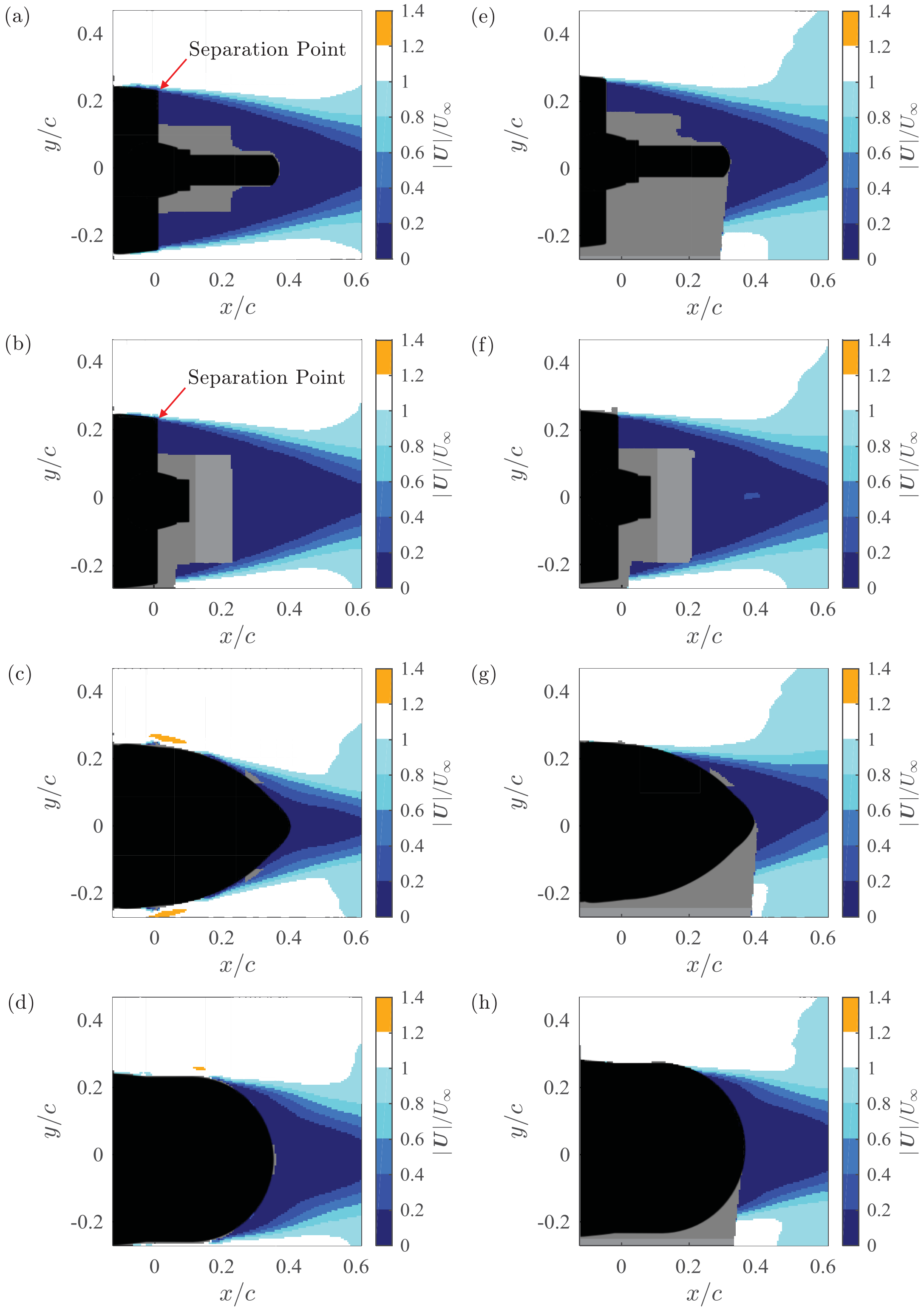

Figure 5.4: Normalized velocity magnitudes comparing the (a-d) isolated fuselage and (e-h) the rotor equipped model for the four rear-fuselage configurations at zero angle of incidence.

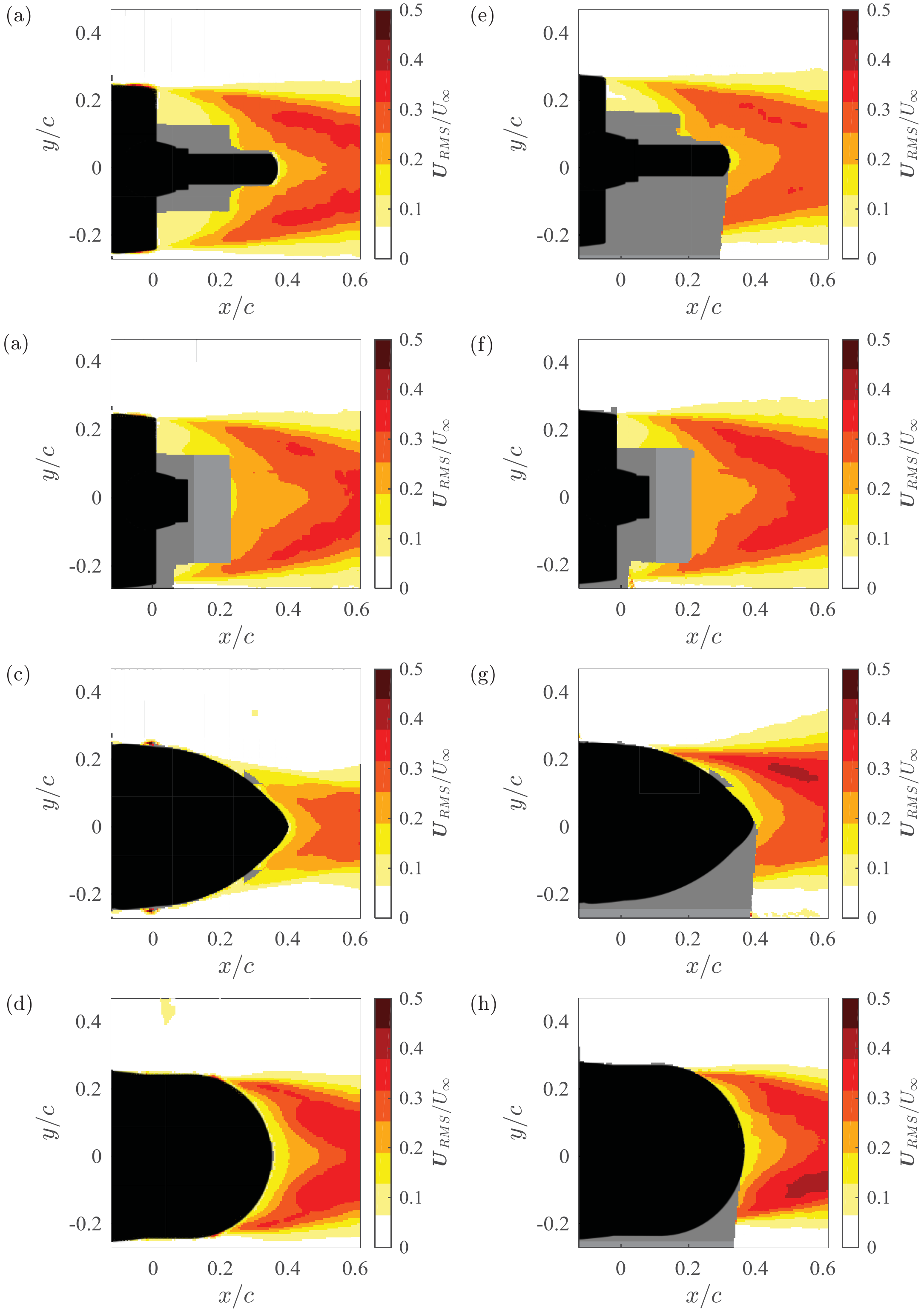

Figure 5.5: Normalized RMS velocity fields comparing the (a-d) isolated fuselage and (e-h) the rotor equipped model for the four rear-fuselage configurations at zero angle of incidence.

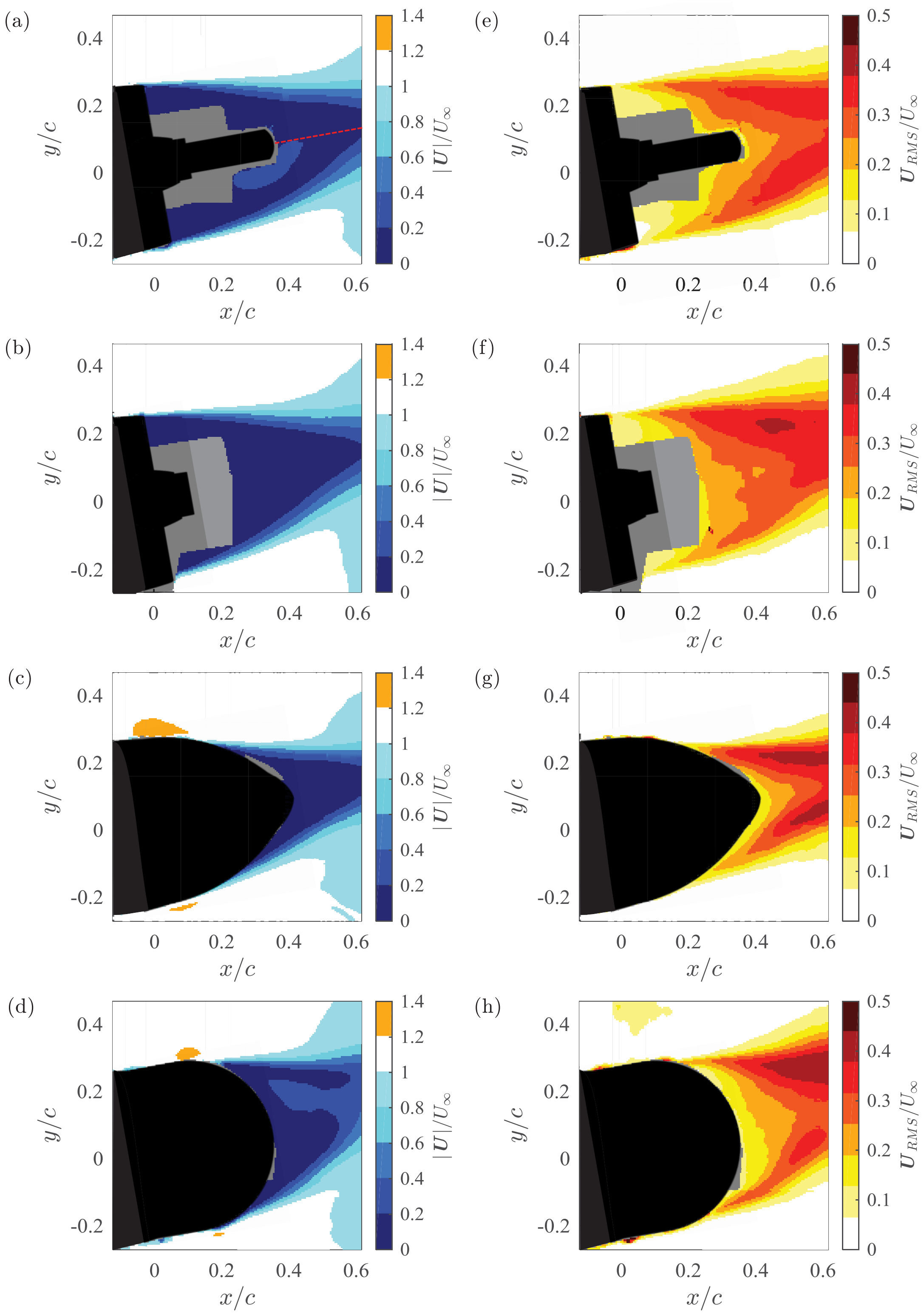

Figure 5.6: (a-d) Normalized velocity magnitudes and (e-h) RMS fluctuation fields comparing the four fuselage geometries at a side-slip angle of $\beta = 10°$.

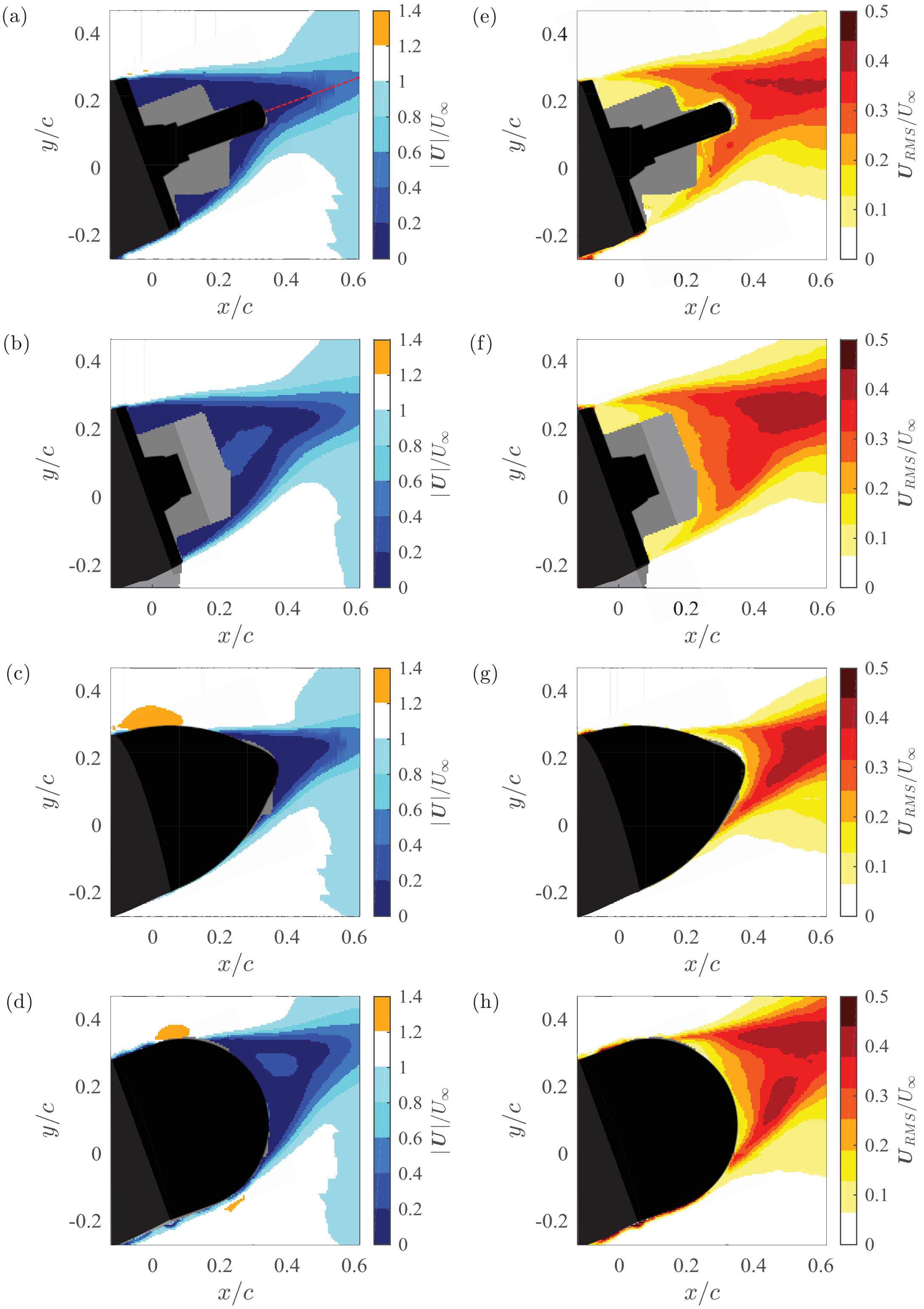

Figure 5.7: (a-d) Normalized velocity magnitudes and (e-h) RMS fluctuation fields comparing the four fuselage geometries at a side-slip angle of $\beta = 20°$.

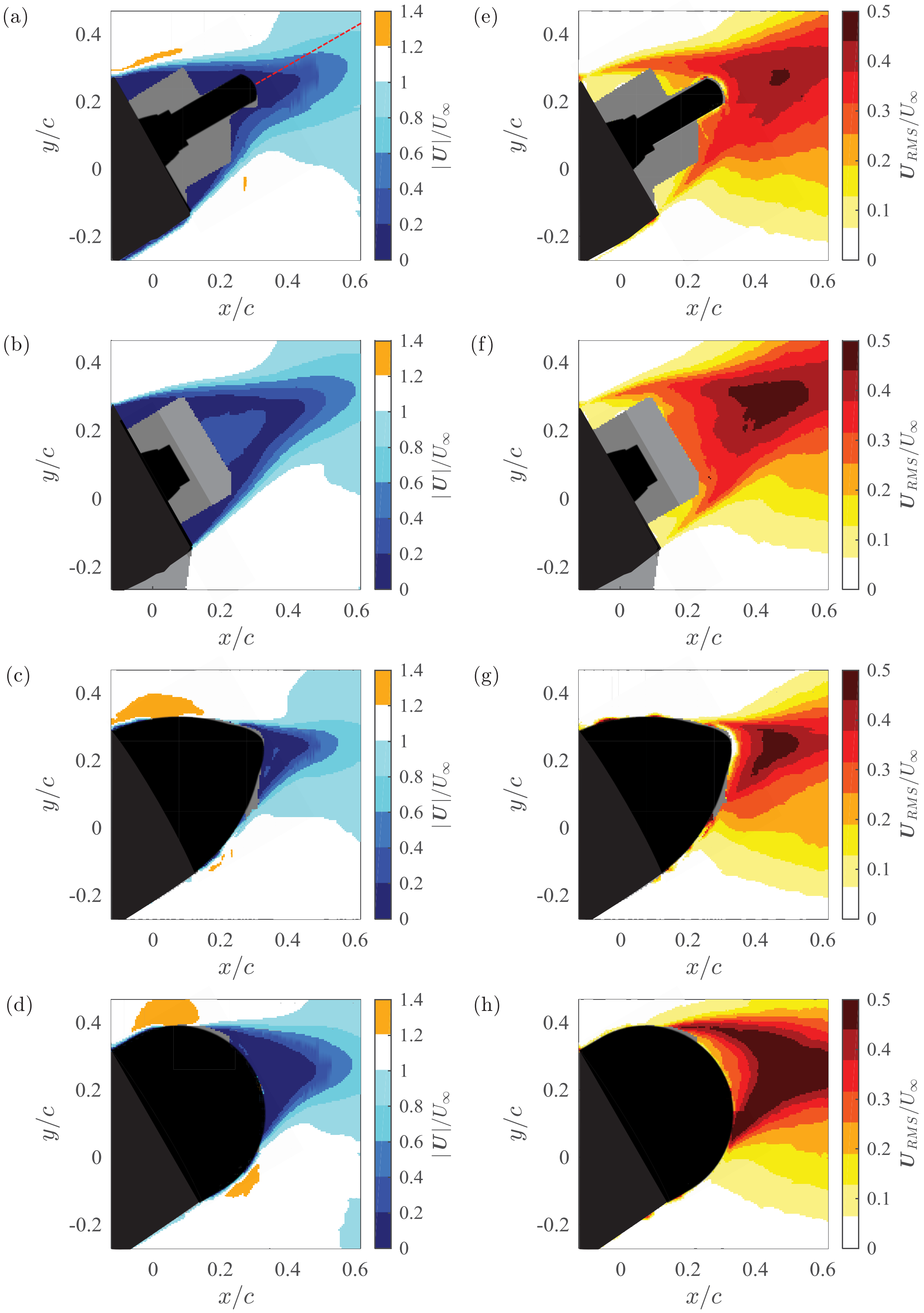

Figure 5.8: (a-d) Normalized velocity magnitudes and (e-h) RMS fluctuation fields comparing the four fuselage geometries at a side-slip angle of $\beta = 30°$.

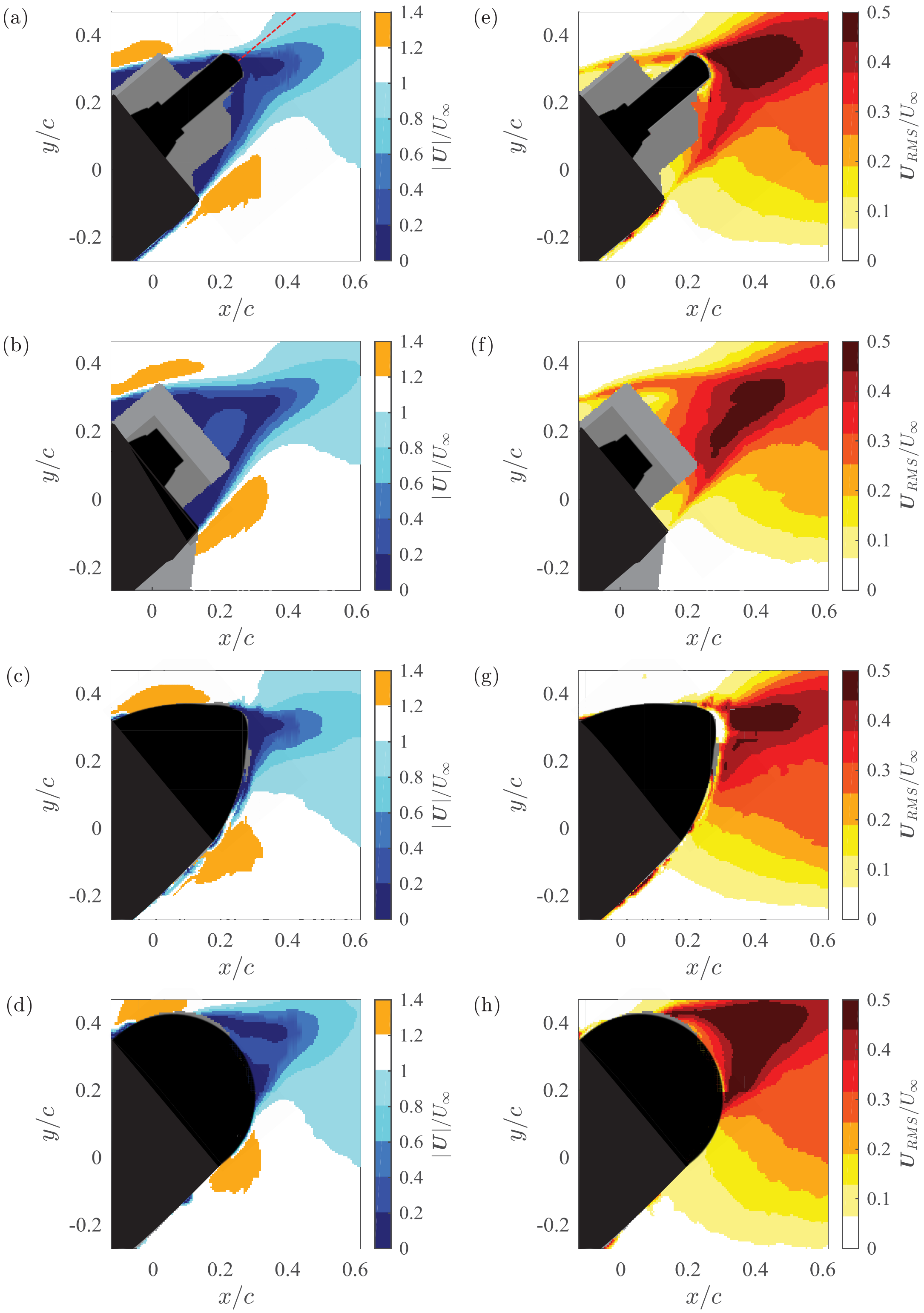

Figure 5.9: (a-d) Normalized velocity magnitudes and (e-h) RMS fluctuation fields comparing the four fuselage geometries at a side-slip angle of $\beta = 40°$.

Chapter 6

Conclusions

6.1 Summary of Results

An experimental setup was developed in the University of Alberta wind tunnel to resemble the flow acting on a helicopter fuselage under various flight conditions. Six-axis load cell measurements were performed for the forward flight condition of -15° $\leq \alpha \leq$ 15° at $\beta = 0°$, and for the level flight condition of 0° $\leq \alpha \leq$ 180° at $\alpha = 0°$. The development of the separation bubble in the rear-fuselage wake was analyzed using stereo and multiple-camera planar PIV techniques.

The characterization of the forward flight condition revealed the dependency of the drag and lift forces on the angle-of-attack. The drag was found to have the highest magnitude of the aerodynamic forces and decreased gradually as the angle-of-attack was increased, as noticed in similar investigations in literature. The lift was found to linearly increase with down-force present for -15° $\leq \alpha \leq$ 5° and positive lift for 5° $\leq \alpha \leq$ 15°. The side force was shown to have no true dependency on the angle-of-attack, as expected for a body that is symmetric about its plane of rotation. The pitching moment showed notable variations with changing angle-of-attack. A nose-down pitching moment was present for -15° $\leq \alpha \leq$ 7° and a nose-up moment was present for 7° $\leq \alpha \leq$ 15°. The pitching moments experienced a gradually increasing slope ($\mathrm{d}C_m/\mathrm{d}\alpha$) for -15° $\leq \alpha \leq$ 0° and a nearly linear trend for 0° $\leq \alpha \leq$ 15°. Both the roll and the yaw moments had no reliance on the angle-of-attack, as anticipated due to the symmetry of the fuselage.

The load measurements of the level flight condition indicated that the aerodynamic forces acting on the body have a stronger dependence on the side-slip angle than the angle-of-attack. The drag coefficients at large side-slip angles were nearly an order of magnitude larger than those measured in the forward flight condition. The maximum magnitude of the drag coefficients occurred at $\beta = 80°$. The side force coefficients were positive for 0° $\leq \beta \leq$ 100°, reaching a maximum magnitude at $\beta = 60°$. The lift force coefficients had much smaller variations with changing side-slip angle and fluctuated around zero lift for the full range of side-slip. The yaw moments were the dominant moments in the level flight condition. Large yaw moments were introduced as the projected frontal area increased, with large moment arms relative to the center of mass. The yaw moment coefficients approximately follow a sinusoidal pattern over the 180° period. The roll moment coefficients are positive in magnitude for the full range of tested side-slip angles. The roll moments increased up to a maximum magnitude at $\beta = 90°$. The pitch moment coefficients showed a similar range of magnitudes as the roll moment coefficients. The pitch moments had much more volatile response to changing side-slip angle. Large fluctuations in magnitude were noticed over the 10° side-slip intervals, drawing concerns for smooth flight operation.

The effect of the rotor downwash was characterized for three angle-of-attack values, including α = -5°, 0°, and 5°. The presence of the main rotor downwash was found to cause a more rapid expansion of the downstream wake in the lateral direction. The expansion of the wake would be indicative of an increase in the drag force acting on the fuselage, similar to trends found in literature. An additional feature that resulted from the main rotor downwash was the increased velocity magnitude in the longitudinal-vertical plane of the wake. The downwards component of the main rotor downwash adds to the velocity vector, thus increasing the magnitude of the velocity by approximately 10%. Ultimately the main rotor downwash was deemed to have minimal effect on the rear-fuselage wake development.

Four rear-fuselage designs were developed to analyze the aerodynamic performance of each configuration at side-slip angles ranging from $\beta = 0°$ to 40°. The six-axis load cell measurements revealed some distinct differences between the performance of the streamlined, round, and removed motor configurations from the baseline motor geometry. The removed motor configuration experienced similar drag characteristics as the baseline motor geometry. The streamlined casing was able to reduce the drag by up to 20% between $0° \leq \beta \leq 30°$, while the rounded casing increased the drag by up to 18% over $0° \leq \beta \leq 40°$. The streamlined and round casings were able to exhibit similar roll moment characteristics as the baseline configuration for $0° \leq \beta \leq 25°$ before diverging at higher side-slip angles. The sharp transitions that were notice in the pitch moment coefficients of the baseline motor configuration between $\beta = 20°$ and 30° were able to be mitigated using the designed cases. The streamline case was able to reduce the magnitude swing by 36%, while the round case was able provide a 67% reduction.

The four camera planar PIV investigation of the rear-fuselage wake revealed the effect of the aft-body design on the wake development. The streamline case was observed to consistently decrease the size of the low velocity separation bubble for all side-slip angles. The more gradual curvature of the streamline case delays the flow separation to a point farther downstream on the fuselage. The rounded case had blunter profile and increased the size of the wake and the fluctuation region. The advantage of the rounded case was a result of the constant curvature that allowed for separation to occur from a rounded edge, rather that a sharp and fixed location that was experienced by the baseline fuselage model. The rounded separation edge provided a smoother transition in pitch and roll moments as the side-slip angle was increased.

6.2 Future Considerations

Based on some of the recent studies and developments in the area of helicopter fuselage aerodynamics and flow measurement techniques, a few suggestions for future work are suggested:

- Implement passive and active flow control techniques (i.e. vortex generators, synthetic jets, or actuators) to suppress the flow separation to a higher degree.
- Apply large-scale PIV techniques using larger and more reflective particles, such as Helium Filled Soap Bubbles, to analyze a broader portion of the rear-fuselage wake
- Perform time resolved flow measurements over swept side-slip or angle-of-attack to visualize variation of the flow during changing flight conditions.

Bibliography

Ahmed, S. R., G. Ramm and G. Faltin (1984). Some salient features of the time-averaged ground vehicle wake. Technical report. SAE International. Ipswich, MA. Technical Paper 840300.

Anderson, J. (2016). *Fundamentals of Aerodynamics.* pp. 896–925. 5 ed.. McGraw-Hill. New York.

Bello-Millán, F.J., T. Mälelä, L. Parras, C. del Pino and C. Ferrera (2016). Experimental study on Ahmed's body drag coefficient for different yaw angles. *Journal of Wind Engineering and Industrial Aerodynamics* **157**, 140.

Boniface, J. (2016). A computational framework for helicopter fuselage drag reduction using vortex generators.. *Journal of the American Helicopter Society* **61**(3), 1–13.

Breitsamter, C., M. Grawunder and R. Reß (2014). Aerodynamic design optimisation for a helicopter configuration including a rotating rotor head. In: *29th Congress of the International Council of the Aeronautical Sciences.* St. Petersburg, Russia.

Brunello, D., G. Clarke and R. Reddy (2012). Numerical and experimental analysis of a representative ADF helicopter fuselage. In: *28th Congress of the International Council of the Aeronautical Sciences.* Brisbane, Australia.

Cook, M. V. (2013). *Flight Dynamics Principles.* pp. 33–71. 3 ed.. Butterworth-Heinemann. Oxford, UK.

De Gregorio, F., K. Pengel and K. Kindler (2012). A comprehensive PIV measurement campaign on a fully equipped helicopter model. *Experiments in Fluids* **53**(1), 37–49.

Drees, J. M. and K. W. Harvey (1970). Helicopter gust response at high forward speed. *Journal of Aircraft* **7**(3), 225–230.

Filippone, A. (2007). Prediction of aerodynamic forces on a helicopter fuselage. *The Aeronautical Journal* **111**(1117), 175–184.

Fradenburgh, E. A. (1972). Aerodynamic factors influencing overall hover performance. Technical report. Science and Technology Organization. AGARD C.P. 111.

Gholamhosein Pouryoussefi, S., M. Mirzaei and M. Hajipour (2015). Experimental study of separation bubble control behind a backward-facing step using plasma actuators. *Acta Mechanica* **226**(4), 1153–1165.

Grawunder, M., R. Reß, C. Breitsamter and N.A. Adams (2012). Flow characteristics of a helicopter fuselage configuration including a rotating rotor head. In: *28th Congress of the International Council of the Aeronautical Sciences.*

Hayden, J. S. (1976). The effect of the ground on helicopter hover power required. In: *32nd Annual National V/STOL Forum of the American Helicopter Society.* Washington, DC.

Hilbert, K. B. (1984). A mathematical model of the UH-60 helicopter. Technical report. NASA Ames Research Center. Moffett Field, CA. NASA TM-85890.

Hinds, W. C. (1982). *Aerosol Technology: Properties, Behavior, and Measurement of Airborne Particles*. John Wiley & Sons. New York.

Hoffmann, P. H., K. C. Muck and P. Bradshaw (1985). The effect of concave surface curvature on turbulent boundary layers. *Journal of Fluid Mechanics* **161**, 371–403.

Howlett, J. J. (1981). UH-60A Black Hawk engineering simulation program, Volumes I and II. Technical report. United Technologies Sikorsky Aircraft. Stratford, CT. NASA CR-166909 and CR-166310.

Jenkins Jr., J. L., M. M. Winston and G. E. Sweet (1962). A wind-tunnel investigation of the longitudinal aerodynamic characteristics of two full-scale helicopter fuselage models with appendages. Technical report. NASA Langley Research Center. Hampton, VA. NASA TN D-1364.

Kähler, C. J., B. Sammler and J. Kpmpenhans (2002). Generation and control of particle size distributions for optical velocity measurement techniques in fluid mechanics. *Experiments in Fluids* **33**(6), 736–742.

Keane, R. D. and R. J. Adrain (1992). Theory of cross-correlation analysis of PIV images. *Applied Scientific Research* **49**(3), 191–215.

Knight, M. and R. A. Hefner (1941). Analysis of ground effect on the lifting airscrew. Technical report. National Advisory Committe for Aeronautics. Washington, DC. NACA-TN-835.

Kostiuk, L., M. Johnson and Thomas G. (2004). University of Alberta flare research project. Technical report. University of Alberta. Edmonton, Alberta.

Lamballais, E., J. Silverstrini and S. Laizet (2010). Direct numerical simulation of flow separation behind a rounded leading edge: Study of curvature effects. *International Journal of Heat and Fluid Flow* **31**(3), 295–306.

Langer, HJ., R. L. Peterson and T. H. Maier (1996). An experimental evaluation of wind tunnel wall correction methods for helicopter performace. American Helicopter Society 52nd Annual Forum.

Le Pape, A., C. Lienard, C. Verbeke, M. Pruvost and J. L. De Coninck (2015). Helicopter fuselage drag reduction using active flow control: A comprehensive experimental investigation. *Journal of the American Helicopter Society* **60**(3), 1–12.

Leishman, J. G. (2006). *Principles of Helicopter Aerodynamics*. 2 ed.. Cambridge University Press. New York.

Lin, JC. (1999). Control of turbulent boundary-layer separation using micro-vortex generators. In: *30th AIAA Fluid Dynamics Conference*. AIAA Paper 99-3404.

Lin, JC., FG. Howard and GV. Selby (1990). Small submerged vortex generators for turbulent flow separation control. *Journal of Spacecraft and Rockets* **27**(5), 503–507.

Lin, JC., GV. Selby and FG. Howard (1991). Exploratory study of vortex-generating devices for turbulent flow separation control. In: *29th Aerospace Sciences Meeting*. AIAA Paper 91-0042.

Liu, RB., ZG. Nui, MM. Wand, M. Hao and Q. Lin (2015). Aerodynamic control of NACA 0012 airfoil model with spark discharge plasma synthetic jets. *Science China Technological Sciences* **58**(11), 1949–1955.

McRuer, D. T. (1995). Pilor-induced oscillations and human dynamic behavior. Technical report. NASA Dryden Flight Research Center. Hawthorne, CA. NASA CR-4683.

Melling, A. (1997). Tracer particles and seeding for particle image velocimetry. *Measurement Science and Technology* **8**(12), 1406–1416.

Muck, K. C., P. H. Hoffmann and P. Bradshaw (1985). The effect of convex surface curvature on turbulent boundary layers. *Journal of Fluid Mechanics* **161**, 347–369.

Murray, R. M., Z. Li and S. S. Sastry (1994). *A Mathematical Introduction to Robotic Manipulation*. CRC Press.

Nati, G., M. Kotsonis, S. Ghaemi and F. Scarano (2013). Control of vortex shedding from a blunt trailing edge using plasma actuators. *Experimental Thermal and Fluid Science* **43**, 199–210.

Pahlke, K. G. (2007). The GOAHEAD project. In: *33rd European Rotorcraft Forum*. Kazan, Russia.

Poling, D. R., L. Dadone and D. P. Teliones (1989). Blade-vortex interaction. *AIAA Journal* **27**(6), 694–699.

Post, M. and C. Corke (2004). Separation control on high angle of attack airfoil using plasma actuators. *AIAA Journal* **42**(11), 2177–2184.

Prandtl, L. (1904). Über flüssigkeitsbewegung bei sehr kleiner reibung. In: *Third International Congress of Mathematicians*. Vol. 45. Quarterly Applied Mathematics. Heidelberg, Germany. pp. 561–571.

Prasad, A. K. (2000). Stereoscopic particle image velocimetry. *Experiments in Fluids* **29**(2), 103–116.

Prouty, R. W. (1986). *Helicopter Performanc, Stability, and Control*. Krieger Publishing Company. Malabar, Florida.

Raffel, M., C. Willert, S. Wereley and J. Kompenhans (2007). *Particle Image Velocimetry: A practical guide*. p. 4. 2 ed.. Springer. Berlin, Germany.

Raffel, M., F. De Gregorio, K. De Groot, O. Schneider, W. Sheng, G. Gibertini and A. Seraudie (2011). On the generation of a helicopter aerodynamic database. *The Aeronautical Journal* **115**(1164), 103–112.

Renaud, T., M. Costes and S. Peron (2012). Computation of GOAHEAD configuration with Chimera assembly. *Aerospace Science and Technology* **19**(1), 50–57.

Reß, R., M. Grawunder and C. Breitsamter (2015). Aerodynamic analysis of a helicopter fuselage with rotating rotor head. *Progress in Flight Physics* **7**, 99–110.

Seddon, J. and S. Newman (2011). *Basic Helicopter Aerodynamics*. 3 ed.. John Wiley & Sons. Chichester, UK.

Steijl, R. and G. N. Barakos (2009). Computational study of helicopter rotor-fuselage aerodynamic interactions.. *AIAA Journal* **47**(9), 2143–2159.

Stepanov, R., V. Zherekov, V. Pakhov, S. Mikhailov, A. Garipov, W. Yakubov and G. N. Barakos (2016). Experimental study of helicopter fuselage drag. *Journal of Aircraft* **53**(5), 1343–1360.

Sweet, G. E. and J. L. Jenkins Jr. (1962). Wind-tunnel investigation of the drag and static stability characteristics of four helicopter fuselage models. Technical report. NASA Langley Research Center. Hampton, VA. NASA TN D-1363.

Tulapurkara, E. G, A.B. Khoshnevis and J. L. Narasimhan (2001). Wake-boundary layer interaction subject to convex and concave curvatures and adverse pressure gradients. *Experiments in Fluids* **31**(6), 697–707.

Van der Hulst, H. C. (1981). *Light scattering by small particles*. John Wiley & Sons. New York.

Vogel, F., C. Breitsamter and N. A. Adams (2010). Aerodynamic analysis of a helicopter fuselage. In: *New Results in Numerical and Experimental Fluid Mechanics VII* (A. Dillmann, G. Heller, M. Klaas, W. Nitsche, W. Schrder and H.-P. Kreplin, Eds.). pp. 603–610. Springer. Berlin, Germany.

Wagner, S.N. (1973). Problems of estimating the drag of a helicopter. In: *AGARD Conference Proceedings.*

Wang, JJ., LH. Feng and CJ. XU (2007). Experimental investigations on separation control and flow structure around a cylinder with synthetic jet. *Science in China Series E* **50**(5), 550–559.

Wang, L., Y. Dai and C. Yang (2017). Gust response analysis for helicopter rotors in hover and forward flights. *Shock and Vibration* **2017**, 1–20.

Wieneke, B. (2005). Stereo-piv using self-calibration on particle images. *Experiments in Fluids* **39**(2), 267–280.

Williamson, C. H. K. and R. Govardhan (2004). Vortex-induced vibrations. *Annual Review of Fluid Mechanics* **36**(1), 413–455.

Zanotti, A., G. Droandi, G. Gibertini, D. Grassi, G. Campanardi, F. Auteri, A. Aceti and A. Le Pape (2016). Wind-tunnel tests of a heavy-class helicopter optimised for drag reduction. *The Aeronautical Journal* **120**(1231), 1446–1469.

Appendix A

Load Measurement Uncertainty

Two measurements of the aerodynamic loads were performed for -15° $\leq \alpha \leq$ 15° at zero side-slip, as shown in Figure A.1.

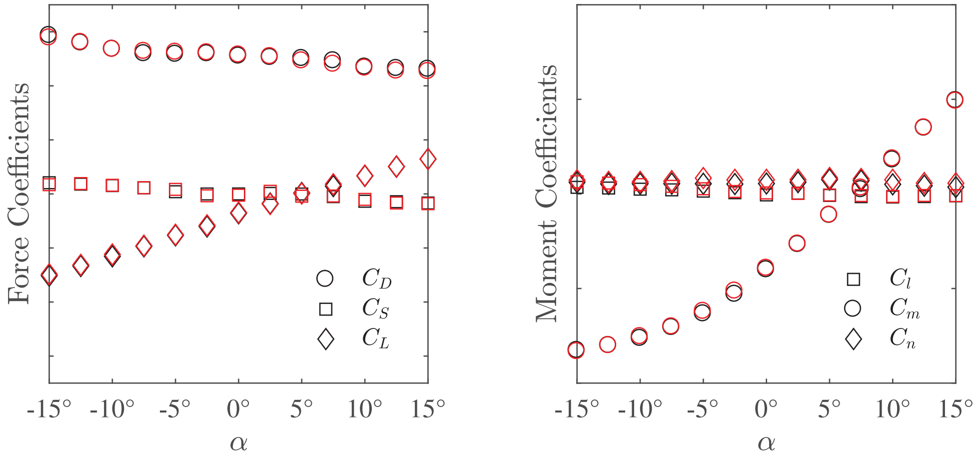

(a) (b)

Figure A.1: (a) Force coefficients and (b) moment coefficients for the baseline configuration with varying angle-of-attack at zero side-slip using black and red markers to distinguish the repeated measurements.

The aerodynamic force coefficients were calculated using the equation,

$$C_f = \frac{f}{\frac{1}{2}\rho_\infty U_\infty^2 A_{ref}} \tag{A.1}$$

The uncertainty for the aerodynamic force can be found using the propagation of uncertainties for a purely multiplicative equation as,

$$U_{C_f}^2 = U_f^2 + U_{\rho_\infty}^2 + 4U_{U_\infty}^2 + U_{A_{ref}}^2 \tag{A.2}$$

where U_{C_f} is the percent uncertainty of the dimensionless force coefficient C_f. The uncertainty of the force measurement can be broken down to precision (P_f) and bias (B_f)

uncertainty components, such that

$$U_f^2 = P_f^2 + B_f^2. \tag{A.3}$$

The bias uncertainty for the force measurements was given by the manufacturer to be a maximum of 1.5%, as shown previously in Table 3.1. The precision uncertainty is related to repeated measurements, and for small sample sizes, n, can be found following

$$P_f = t_{\alpha/2,\nu} \frac{S_f}{\sqrt{n}} \tag{A.4}$$

where $t_{\alpha/2,\nu}$ is the t-distribution for a given confidence interval $\alpha = 1 - c$ and degrees of freedom $\nu = n - 1$, while S_f is the standard deviation of the repeated values. For two repeated measurements and a confidence interval of 95%, the t-distribution value can be found to be $t_{0.025,1} = 12.706$. The maximum standard deviation that was calculated from the force coefficients occurred for the drag coefficients at $\alpha = 7.5°$, and was $S_{C_d} = 0.0045$. The largest precision error in the force measurements was computed to be $P_{C_f} = 0.0405$. The measurement uncertainty of the wind speed measurements for U_∞ was determined to be $\pm 3.3\%$ based on the resolution for the display, while the uncertainty in the air density and reference area were assumed to be $\pm 1\%$. The maximum total uncertainty for for the force coefficients was calculated at $\alpha = 7.5°$ for the drag coefficients to be $\pm 4.59\%$. Similarly, the maximum uncertainty in the moment coefficients was found to be $\pm 2.29\%$ for the roll moment at $\alpha = -15°$. The force and moment coefficients are shown with error bars in Figure A.2.

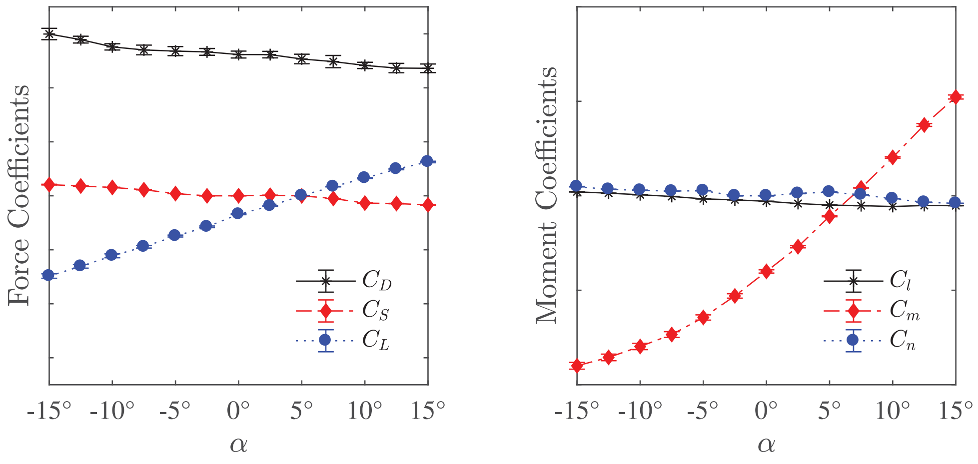

(a)

(b)

Figure A.2: (a) Force coefficients and (b) moment coefficients for the baseline configuration with varying angle-of-attack at zero side-slip with error bars.

Appendix B

Time Stability of Load Cell Data

This appendix shows the variation of the aerodynamic load coefficients over the 120 s testing period. Figures B.1-B.3 show the drag, side, and lift force coefficients while Figures B.4-B.6 show the roll, pitch, and yaw moment coefficients at $\alpha = 15^\circ$ and zero side-slip. It can be seen that the measured forces and moments do not show any significant variation with time, and thus averaging the values over the 120 s recording period is acceptable.

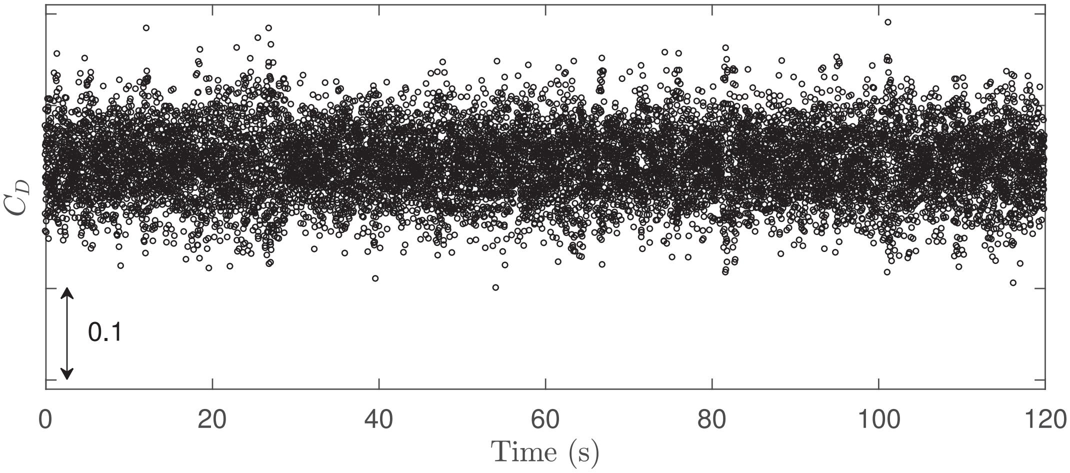

Figure B.1: Variation of the drag force coefficients with time at $\alpha = 15^\circ$ and zero side-slip.

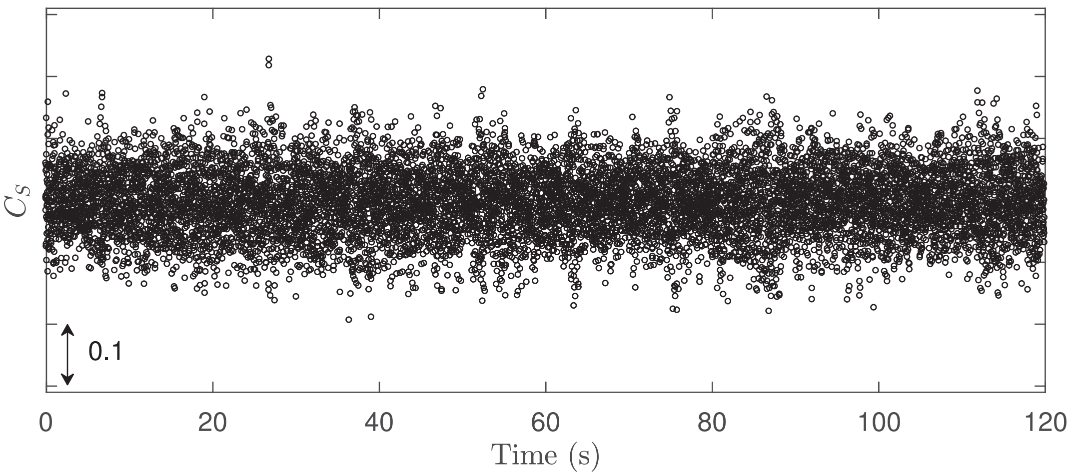

Figure B.2: Variation of the side force coefficients with time at $\alpha = 15°$ and zero side-slip.

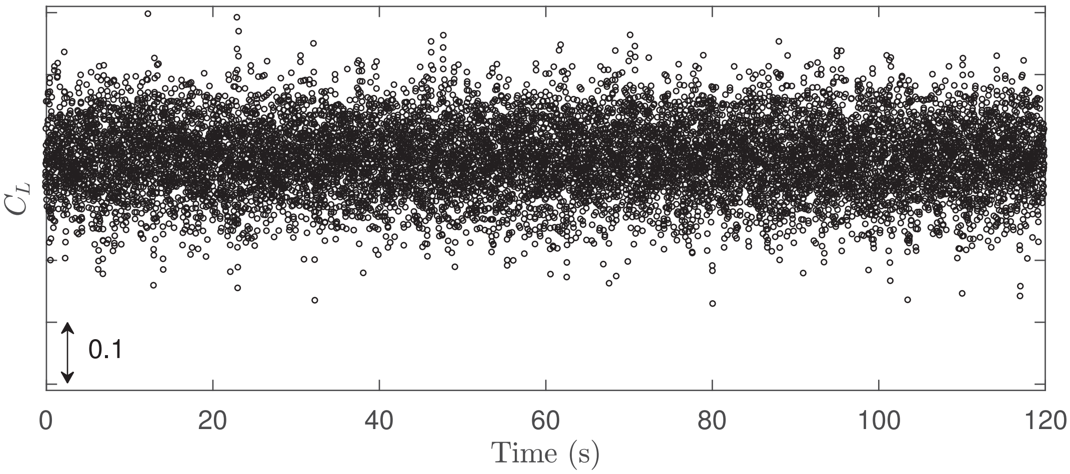

Figure B.3: Variation of the lift force coefficients with time at $\alpha = 15°$ and zero side-slip.

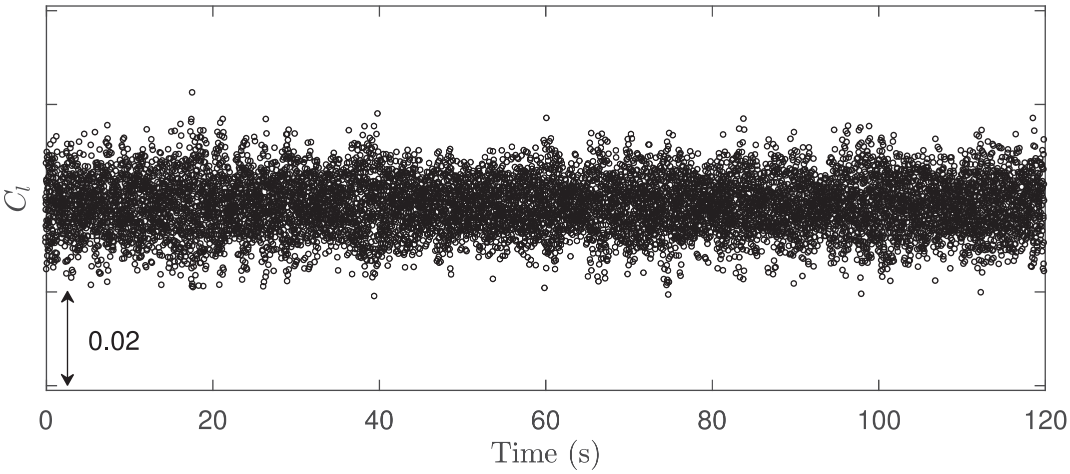

Figure B.4: Variation of the roll moment coefficients with time at $\alpha = 15°$ and zero side-slip.

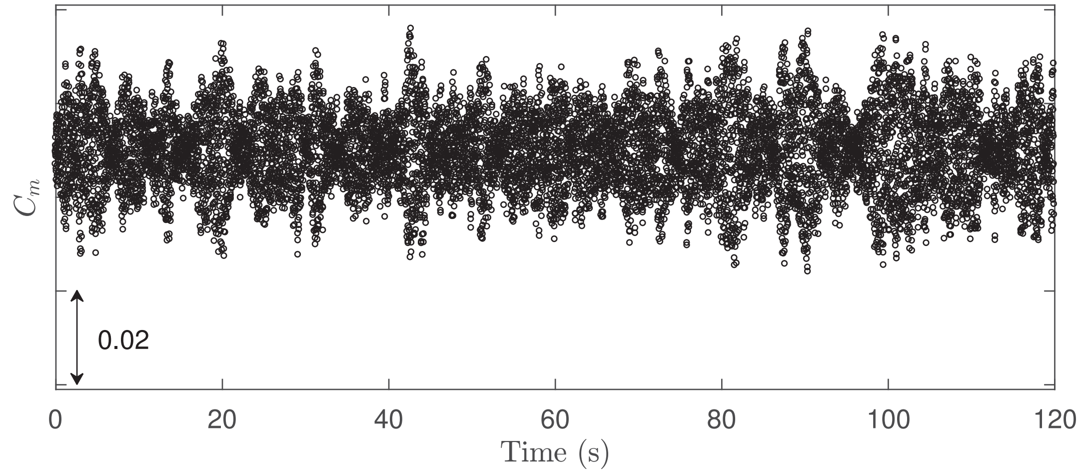

Figure B.5: Variation of the pitch moment coefficients with time at $\alpha = 15^\circ$ and zero side-slip.

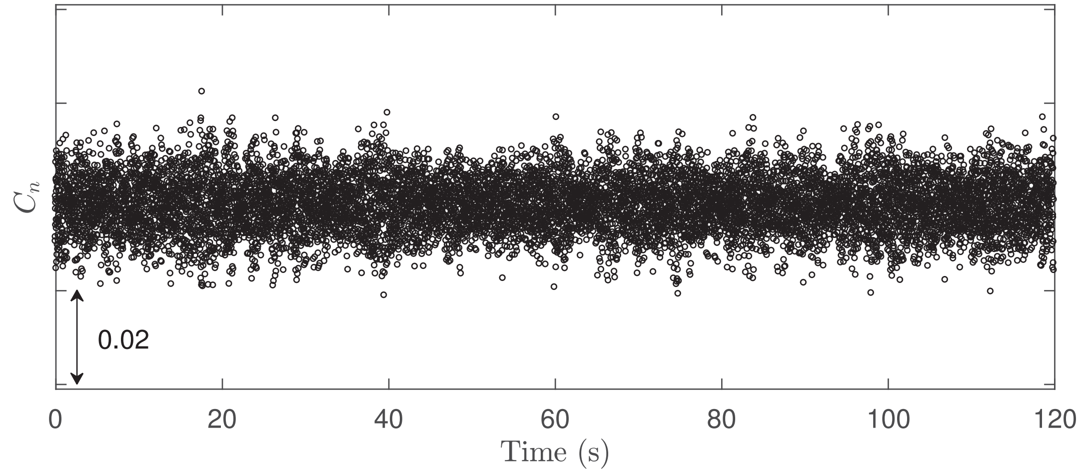

Figure B.6: Variation of the yaw moment coefficients with time at $\alpha = 15^\circ$ and zero side-slip.